11-7-2021

Interface-Induced Lattice Structure and Magnetism in Ultrathin Transition Metal Oxide Trilayers

David Howe
Louisiana State University and Agricultural and Mechanical College

INTERFACE-INDUCED LATTICE STRUCTURE AND MAGNETISM IN ULTRATHIN TRANSITION METAL OXIDE TRILAYERS

A Dissertation

Submitted to the Graduate Faculty of the
Louisiana State University and
Agricultural and Mechanical College
in partial fulfillment of the
requirements for the degree of
Doctor of Philosophy

in

The Department of Physics and Astronomy

by
David Howe
B.S., University of Notre Dame du Lac, 2014
December 2021

Acknowledgements

I have always tried to live my life by the words of the great Bob Dylan, “Don’t think twice, it’s alright”. To me, I take that to mean things may not always go the way you thought in life, but that fact doesn’t mean you can’t enjoy the journey or make life any less beautiful. I can say with certainty that my dissertation work did not always go as I had envisioned, but I have also found that the road to this defense has still been filled with its joys.

I must firstly thank Dr. Jiandi Zhang for his guidance and continually renewing vigor for physics, its research, and life in general. I often struggled during my graduate studies to maintain my desire to find new physics, but Dr. Zhang was always able to find the interesting threads in every project and revive my love of the endeavor for scientific discovery. His insight into the crucial physical questions and advice on how best to elucidate them was invaluable in my doctoral work. I sincerely enjoyed spending time with him both inside and outside of work, and I will always remember his inexhaustible travel stories and excellent tea making abilities.

My co-advisor for of my doctoral studies was the late Dr. E. Ward Plummer. He was a man who was capable of being strikingly brilliant, insightful, gruff, and approachable, oftentimes simultaneously. He was again someone who had an incredible ability to understand the important variables in a problem and get to the heart of an issue. His stature in the field was inspiring, though his personality and intellect were always his most inspiring attributes. He is acutely missed by the physics community in general and in particular by his colleagues at LSU.

I would not be graduating with a doctorate in physics without the incessant and unfailing guidance of Dr. Mohammad Saghayezhian. Over the many years together in the trenches of the lab, I have seen him at many stages of his education and career. Through all of them, he has been impossibly generous, kindly forthright, and truly brilliant. He guided me when

I didn't know which directions to go, gave me insights that changed the course of my education and life, and was always there with what I needed in the moment. I will forever be awed by his scientific mind, but it is his warm spirit that has blessed me most profoundly. I am honored to be his friend.

My other graduate colleagues throughout the years have also been absolutely instrumental in my progress both through my physics education and my life. Experimental labs require large amounts of time attempting to make machines work like they're supposed to, and it's through the crucible of wrapping chambers in aluminum foil that great professional and personal bonds can be formed. I have felt extremely grateful in my education at LSU to have encountered, virtually exclusively, so many friendly and intelligent people who have always been willing to lend a hand in the lab or on the white board. Between filling helium and going for afternoon idea sessions/coffee time, I always like part of a group that could enjoy themselves while moving physics forward. They have expanded my ideas of the world and shown me that for all our differences we all love the same things. My sincerest thanks to. Dr. Prahald Siwakoti, Zeeshan Ali, Dr. Hangwen Guo, Dr. Gaomin Wang, Dr. Zhen Wang, Dr. Roshan Nepal, Michael Wu, Dr. Joel Taylor, Dr. Ramakanta Chapai, Dr. Lina Chen, Smita Spear, and Frank Womack.

I have always been proud to be my parent's child. They have shown me from my earliest memories the extent they would go for one another and their family, and the gifts they made with their time, resources, and hearts for the good of their children are hard to fathom. I have benefitted beyond measure from the house they made for me and the opportunities they gave to me. My mother gave me my faith and love of knowledge, my father has given me language and use of my hands, and together they have given me love beyond measure. I will always be proud to be their child.

Finally and most wholly I thank Mary Catherine Holt. With her, even from across the world, every dark thought can turn to song and every sadness turns to mirth. Every time I felt like I could not continue on in the program, she told me I could do anything I put my mind to. I now know that to be true, so long as she is by my side. She is my favorite person I ever met, and her infectious enthusiasm, dazzling mind, intense empathy, and genuine love for every person she meets are the most beautiful things I've ever seen. I marry her exactly one month after this defense, and I know that my life after this doctoral work and that day will be filled by more joy than any man dare dream of. I am eternally grateful that we get to share our lives together.

Table of Contents

List of Tables

List of Figures

Abstract

The study of magnetism has been a rich playground in condensed matter physics due to the multiple mechanisms capable of producing the effect and its relationship to multiple characteristics of a material. Transition metal oxides (TMOs) have been of particular interest for ongoing research into magnetic phenomenon due to the abundance of interesting physical phenomena found in member systems such as colossal magnetoresistance, skyrmion formation, and interface-driven 2D electron gases. Thin films introduce an additional thickness-dependent element, where reduction below a critical thickness eliminates the magnetic coherence of a system and FM order is lost. The atomic structure of these materials can also affect the formation of coherent spin alignments due to hybridization change and charge doping. Finally, heteroepitaxy of multiple materials in strained systems can introduce new interactions that allow for novel FM states, such as the giant magnetoresistance found in 3d TMO superlattices.

This thesis work will aim probe the evolution of certain FM materials through each of these manipulations, namely the dependence of FM behavior on thickness, structural change, and heterointerfacing. The relationship between defect evolution and epitaxial strain will be examined in heterostructures between strong spin-orbit coupled $SrIrO_3$ and ferroelectric $BaTiO_3$, finding that strong strain is the primary driver of defect formation and not symmetry mismatch at interfaces. Thickness dependent studies of ferromagnetic phase $[La_{.67}Ca_{.33}]MnO_3$ (LCMO) heterostructures will show that a novel FM state can be induced in LCMO layers by introducing buffer $SrRuO_3$ (SRO) layers. This SRO induced onset occurs well below the dead layer thickness of monolithic LCMO and exists in completely insulating films, contrary to normal double-exchange manganite FM models. The SRO system is compared structurally and electronically with the lower enhancement effects seen from buffer layers $CaRuO_3$ and $SrTiO_3$. Multiple causes

of this FM are considered, and through resistivity modelling and structural analysis we find that an incipient FM phase in SRO coupled with structural change and an interfacially-mediated AFM pinning are the most likely driving factors. Through this research we find a new route for magnetism in transition metal oxides that pushes the dimensional control of magnetic functionalities in artificial heterostructures.

Chapter 1. Introduction to Magnetic Order and Transition Metal Oxides

When designing projects in experimental condensed matter physics, and particularly in thin films, we are often looking for new and interesting ways to combine the known degrees of freedom (DOF) in crystals that may yield new insights into their origins and behavior. By looking for the interplay between the electronic DOF, such as the orbital and charge state, and the lattice, we can probe our deepest lingering questions about how materials interact and how to control them to our advantage. It is therefore important in designing experiments to look for systems with a novel cooperation of these characteristics, but also to develop accompanying test cases in such a way as to isolate, as much as possible, the characteristics at work. This has led us to consider how these crystallographic DOF can play a role in low dimensional magnetism, colossal magnetoresistance (CMR), and magnetic anisotropy.

$Sr_{(n+1)}Ru_{(n)}O_{(3n+1)}$ is a layered perovskite of the Ruddleson-Popper series, which have the form $A_{(n+1)}B_{(n)}O_{(3n+1)}$. The different members of the SRO family have disparate characteristics, and as n goes to infinity, we reach $SrRuO_3$ (SRO), which in its bulk is an itinerant ferromagnet with the Curie temperature of 160 K [1]. The ferromagnetism in this system is thought to be of Stoner type, where the density of states at the Fermi energy energetically favors one spin alignment over another. If this material is grown as a thin film on STO (001), the orientation of the magnetization is majority out of plane (OOP) oriented, and if the dimensionality is further reduced to 4-5 unit cell thickness, the film will eventually lose its metallicity and magnetism altogether, i.e. “dead” layer behavior [1, 2]. The origin of such dead layer behavior is not clear, and it may be possible through fine control of the material’s electronic and structural nature to reverse such effects.

LCMO in its bulk crystal form has a ferromagnetic-metallic ground state, and a simultaneous ferromagnetic and metal-insulator transition at 260K, which is characteristic of a double-exchange (DE) interaction mediated ferromagnetism [3]. Double exchange is mediated through the hopping of electrons between nearest-neighbor Mn sites with different valence states in order to satisfy Hund's rule. This hopping simultaneously creates a metallic state, but if we move from a bulk crystal to a dimensionally confined thin film, the metallicity and ordered magnetism are lost, similar to what is seen in SRO films. The origin of such dead layer behavior in both cases is still under intensive debate. Presumably, the study of interface coupling could help to reveal the nature of these dimensionality effects, potentially reviving the magnetic properties in the ultrathin film limit.

The object of this study is to observe how structural, electronic, and magnetic properties at transition metal oxide interfaces can be manipulated in order to produce higher degrees of functionality. The bulk of this work focuses on magnetic and resistive manipulation in heterostructures between LCMO and buffer layers with different magnetic and structural characteristics, from insulating STO, to paramagnetic CRO, and then primarily to ferromagnetic SRO. We study how the interfacial lattice and magnetic coupling revive the magnetic and electronic properties of the films and even create new interface magnetic states. Our results have shown exciting interface magnetic phenomena, fundamentally different from those in corresponding bulk or individual thin films, suggesting the scientific importance of this designed heterostructure study. We will also study structural change induced by heterointerfaces, looking at defect formation in SIO-BTO heterostructures and how potentially functional defect cores can be placed strategically.

The research project outlined above and elucidated below will systematically study a suite of SRO-LCMO trilayer heterostructures grown on STO(001) with various techniques that will characterize their magnetic, resistive, and structural characteristics. We also will create an ancillary suite of films, namely LCMO-CRO and LCMO-STO heterostructures, to reveal the possible causes of the observed phenomena. In order to create this complete compendium, we have undertaken many measurements in house at LSU, in conjunction with STEM work completed at Brookhaven National Lab. The following sections will give an overview of the current state of research in the field and our understanding of the outstanding issues to be considered.

1.1 Magnetic Considerations in Transition Metal Oxides

First we must understand the physical origins of magnetism in transition metal oxide materials before we can make sense of its evolution in LCMO and SRO thin films and heterostructures. There are many types of magnetism that can exist in materials, and a brief overview of their behavior and physical origins are provided here. We will look at paramagnetism, diamagnetism, ferromagnetism (FM), and antiferromagnetism (AFM) here, each of which has been seen in various temperature and doping regimes of the materials used in this work.

Magnetism in materials is intimately linked to the orbital angular momentum $\boldsymbol{L}$ and spin quantum momentum $\boldsymbol{S}$ of electrons in the atomic lattice and are typically combined into the total angular momentum $\boldsymbol{J}$ by the simple formula $\boldsymbol{J} = \boldsymbol{L} + \boldsymbol{S}$. Considering the orbital motion of charged electrons, we know from basic physics that moving charged particles produce a magnetic field. We also know that Lenz's law states that charge will move in order to counteract any changing magnetic field. If we consider this effect with the moving electrons in their atomic

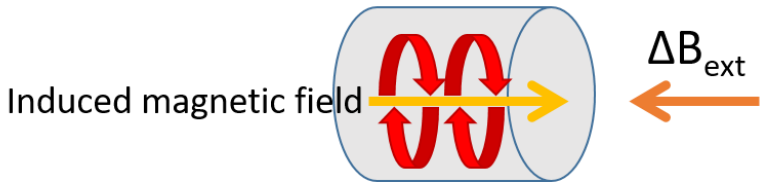

Figure 1.1. Representation of simple diamagnetic effect in materials based on Lenz's law. Materials will tend to move electrons such that an applied magnetic field is expelled. Perfect diamagnets are able to expel all field that penetrates it, generating an equal and opposite field internally. Type-1 superconductors are perfect diamagnets.

orbitals and an applied external field, this then leads us to diamagnetism, which is the tendency of electrons to change their orbital motion such that an antiparallel field is set up between the material induced field and any externally applied field. Every element is slightly diamagnetic due to this inherent physical nature, but if other types of magnetic ordering exist in the sample from other interactions, they tend to overwhelm this relatively small magnetic component. This effect is seen most acutely in superconductors, where current loops experience no resistance to current change and can perfectly repel any applied magnetic fields. We do note that this qualitative description neglects some quantum mechanical considerations of the electron cloud surrounding atoms, but including these effects merely determines the scale of the effect and not the overall behavior. In our study, STO substrates are diamagnetic, and their magnetic signal is subtracted out of many of our magnetic measurements.

Electron spin becomes pivotal in the paramagnetic, FM, and AFM type materials. Paramagnetic systems tend to align magnetic moments in parallel with an applied field but then do not maintain that internal moment if the external field is removed. This moment is proportional to the field applied. An unpaired electron in atomic orbitals is required for this state to exist, as paired electron spin moments are fully compensated in filled orbitals, limiting which materials can exhibit this character. Many transition metal oxides with low temperature FM

ordering, including LCMO and SRO, occupy a paramagnetic state above their Curie temperatures, as the unpaired electrons still exist above T_c and can therefore be aligned with any applied fields.

If the temperature is brought lower, a material might undergo a ferromagnetic transition, where previously unaligned spin moments and local magnetic domains become long-range ordered in alignment with an applied magnetic field. Ferromagnetism differs from paramagnetic

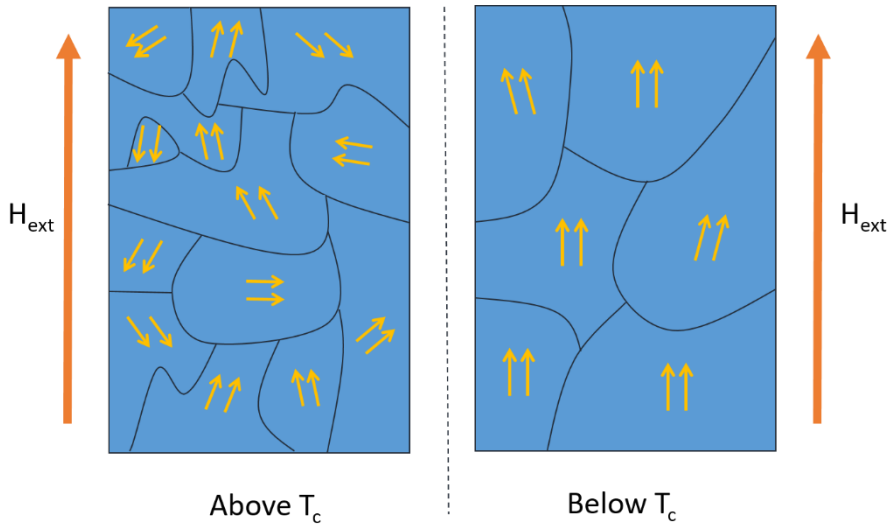

Figure 1.2. Schematic representation of FM domains above and below Tc. Above Tc, small magnetic domains may exist where internal spins are aligned, but large scale order is not stable. Below Tc, magnetic domains merge and each begins to align with the applied magnetic field, though they can still be slightly canted.

materials in that the system tends to stay in this arrangement even if the external field is withdrawn and will persist until either a sufficiently large opposing magnetic field is applied or the temperature is brought above the Curie temperature, both of which provide the necessary energy to break the long-range ordering of the material. The field necessary to align the spins of a ferromagnet is known as a material's magnetic permeability. It is possible to reduce the energy

needed to induce FM alignment of magnetic domains through structural and electronic manipulation [4, 5].

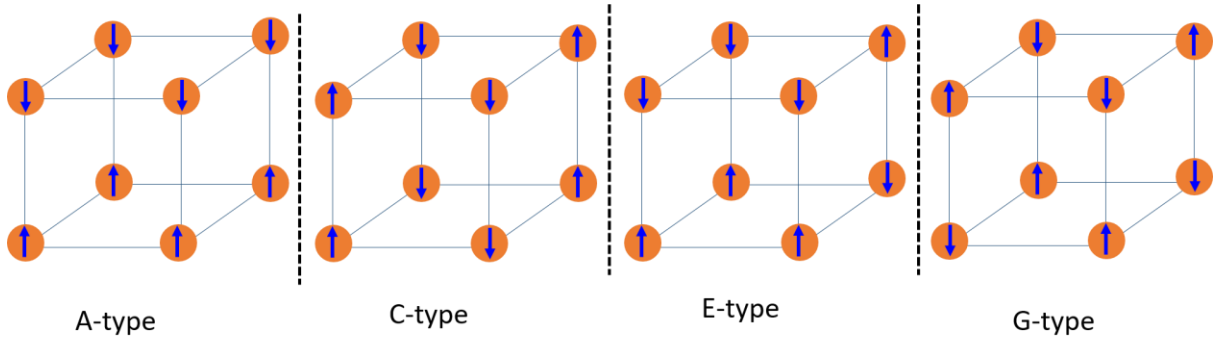

Figure 1.3. Types of AFM order in TMO's. Each set up has net zero total moment.

Antiferromagnetism is related to normal FM alignment, and in transition metal oxides it can be thought of as a juxtaposition of two FM sublattices with antiparallel alignment. AFM alignment can take many forms in transition metal oxides, each of which produces a net zero total magnetization for the sample. These are split into A, C, E, and G-type AFM's, the most common of which in TMOs is G-type, in which every neighboring atomic site has an antiparallel moment. This type of ordering is usually due to superexchange coupling mediated by the oxygen octahedral bond as described by Anderson[6]. Macroscopic magnetic measurements of these types of materials do not show any magnetic response by default, and as such must be observed through other types of measurements such as optical and resistivity measurements. Ferrimagnets are a subclass of AFM's, in which one of the magnetic sublattices has a larger magnetic response than the other, creating a net magnetic moment despite antiparallel alignment. We should remember this type of alignment in the work described below, recalling that AFM alignment can still produce FM responses.

Each of these types of magnetic response to an applied field is dependent on certain theoretical models for how the neighboring atomic moments interact with each other. As

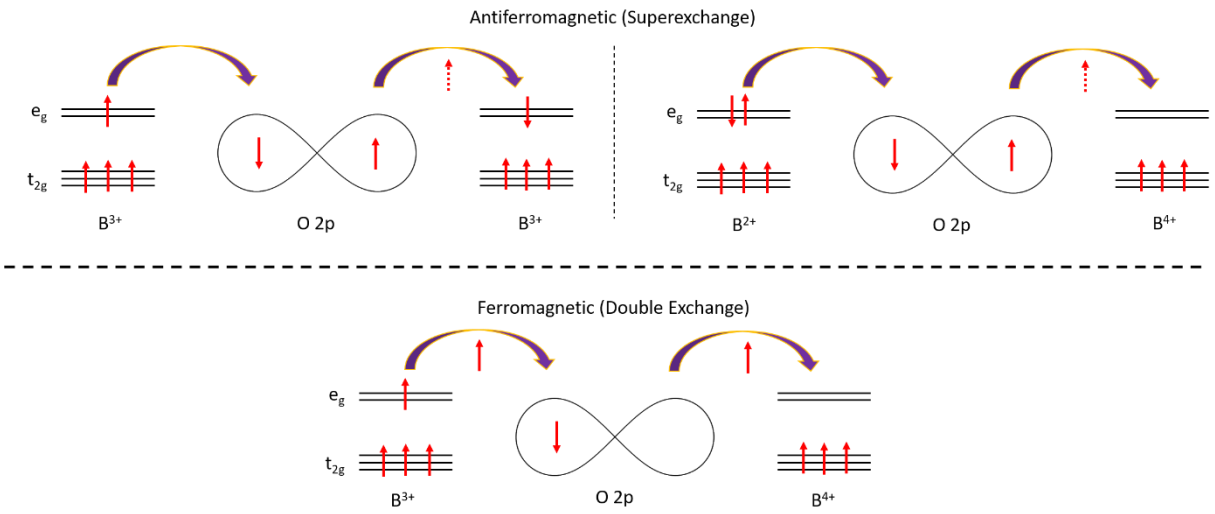

Figure 1.4. Different types of superexchange mediated magnetism. The top row pictures illustrate the AFM isovalent and two electron different B site atomic states, bottom row illustrates the FM aligned state with a single electron difference. AFM cases have virtual electron (dashed arrow) hopping that maintains the valence states of the system, whereas double exchange systems have real electron (solid arrow) hopping.

mentioned above, the superexchange model has been an excellent framework for describing AFM in transition metal oxides [6]. In this model, two d-orbitals of neighboring B-site atoms overlap with an intermediary O 2p orbital. Because of the necessary intermediary O site, this type of exchange is referred to as an indirect exchange coupling. This allows electron motion between the atomic sites. We know that random hopping of the outermost electron must not break Pauli exclusion rules when it arrives at the neighboring site, which means that for identically filled orbitals in a neighboring site, the spins will tend to align antiferromagnetically in order to reduce the hopping energy. AFM alignment is also preferred if one of the B-site atoms has a paired outermost d-orbital while the neighboring atoms have an unoccupied eg band. This AFM preferential alignment is also dependent on the covalent overlap of the B-site and oxygen orbitals, and can be affected by angular change in the orbital alignment, with a 90° bond alignment favoring this AFM alignment as described by the Goodenough-Kanamori rules [7, 8]. This orbital overlap angle is not to be confused with structural bond angles in oxygen octahedral

systems, though there is a correlation between change in structural bond angle and orbital overlap angle which can have important effects. If there is a single electron difference between neighboring atomic sites, then this superexchange interaction will tend to align moments FM, and this interaction is usually referred to as double exchange (DE). It is important to note that though these are both types of indirect exchange, double exchange produces a real interatomic electron hopping between sites that induces a metallic state, whereas AFM superexchange is produced by virtual electron hopping that influences the magnetic character but does not necessitate metallicity. The double-exchange interaction is crucial in our LCMO material and will be discussed in more detail surrounding this particular DE system.

The type of alignment produced through superexchange depends on Hund's rules for orbital filling in atomic shells to determine which orbital and spin arrangements are produced. They qualitatively determine why similarly filled or two-electron different systems likely produce AFM aligned spins and why singly different atomic site hopping electrons maintain a FM alignment across hopping sites. These rules prescribe how the energy is minimized in a system and are applied sequentially, meaning that the first rule is the most important for the minimizing the energy and should be considered first [9, 10]. 1) Orbitals are filled to maximize the spin quantum $\boldsymbol{S}$ of the system. This forces electrons to spread out in a crystal due to the Pauli exclusion principle because they cannot have the same spin and occupy the same atomic orbital, which in turn reduces the Columbic repulsion energy and minimizes the energy of the arrangement. 2) Once $\boldsymbol{S}$ is maximized, the $\boldsymbol{L}$ of the system will also be maximized. This again forces electrons to spread out either intra- or inter-site where they can occupy larger l orbitals and encounter other electrons less. Both of these rules are aiming to reduce the Columbic energy of the system, which is large compared to other effects in most crystals. 3) If S and L are

maximized, then J will either be maximized or minimized, depending on the atomic shell filling of the atomic site. If the shell is half filled or less, the J will be minimized by making it of the form $= |\boldsymbol{L} - \boldsymbol{S}|$, whereas a more than half filled shell tends to maximize total angular momentum $\boldsymbol{J} = |\boldsymbol{L} + \boldsymbol{S}|$. This term is associated with spin-orbit coupling and usually only becomes important in materials with a large spin-orbit splitting of d-orbitals. The first Hund's rule is important in DE ferromagnets, in that it dictates that hopping electrons will attempt to maximize their spin and tend to maintain a single alignment as they hop.

Other types of magnetic interactions are important for mediating the magnetic response in transition metal oxide materials. Three other important mechanisms to be considered in this work are magnetic polarons, antisymmetric exchange (also known as the Dzyaloshinskii–Moriya (DM) interaction), and Stoner-type magnets. While we will discuss Stoner FM's in the particular case of SRO crystals, we will give here a description of magnetic polarons and the DM interaction. Polarons are a quasiparticle excitation of an ionic crystal lattice by a charge carrier that distorts the surrounding crystal and can propagate. It is normally based on a dielectric response to a change in valence state caused by a mobile charge carrier where the atomic site shifts away from equilibrium in order to screen the altered charge state[11]. In Jahn-Teller (JT) active materials however, polarons are formed through a different process. These systems allow electron hopping between neighboring sites, and in certain valence states the electrons may be moving into a degenerate energy level. If this is the case, the crystal can deform itself to lift the degeneracy and form a so-called JT polaron [12]. Due to the enhanced localization of the hopping electron from the induced crystal deformation, conduction through JT polarons is an inherently insulating state. When the localized electron is given enough energy to overcome its localization and hop, it still must obey Hund's rules. In doped manganites, Hund's favors a FM

alignment of any hopping e_g electrons, and in such a system a JT polaron is also magnetic and can mediate FM[13]. This potential mechanism will be discussed in relation to our magnetic and resistivity data.

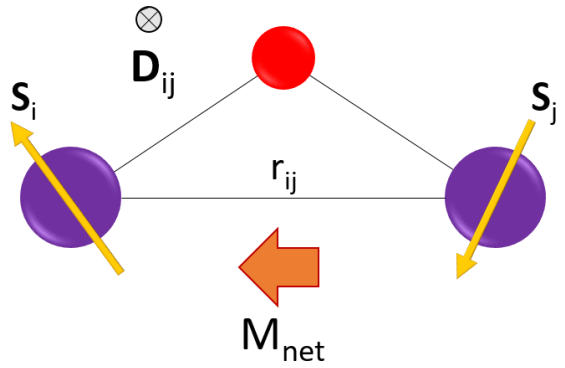

Figure 1.5. DM interaction model. AFM spin alignment can have weak net magnetization if spins are canted due to non-zero D_{ij} term.

Antisymmetric exchange is another source of FM signal in crystals and was first formulated by Dzyaloshinskii and Moriya in 1960 and 1958, respectively [14, 15]. The so-called DM interaction occurs between atomic sites where strong spin-orbit coupling (SOC) can induce a split energy level that creates an excited state at one site and a ground state in another. As this interaction can only take place between these two disparate states, the effect is only observed where there is broken inversion symmetry, which inherently occurs at interfaces and surfaces. The interaction is described the Hamiltonian $H_{DM} = \boldsymbol{D}_{ij} \cdot (\boldsymbol{S}_i \times \boldsymbol{S}_j)$, where $\mathbf{S}_{i,j}$ are the spins of the neighboring sites and $\mathbf{D}_{ij}$ is the DM interaction strength. $\mathbf{D}_{ij}$ can be either positive or negative, where the sign if the spins will tend to align in a parallel (positive) or antiparallel (negative) configuration. In order to minimize the H_{DM} term, the spins will attempt to align at a 90° angle with respect to one another such that the resulting cross product vector is parallel or antiparallel with the $\mathbf{D}_{ij}$ vector. The spins tend to cant relative to one another as a result of this preference. Canting can produce a net FM response in an otherwise AFM aligned system, though the effect

is weak compared to fully FM systems. Antisymmetric exchange has been linked to novel spin textures such as skyrmions, and can become important at interfaces between strong spin-orbit coupled materials[16, 17].

In considering the interface between two different materials, we also must understand the effect of valence change induced by such an interface and its potential role in magnetic alteration. This is commonly referred to as charge transfer, and can have potentially wide ranging implications. If we consider the case of superexchange-mediated magnetic systems, we know that the relative filling of neighboring atomic sites can determine whether a material has an AFM or FM character. We can imagine then if the valence state of these materials is changed we can drastically affect the magnetic properties of the film. Interfacial charge transfer in transition metal oxides typically occurs when the Fermi level differs between two heterostructured materials with different electronegativity [18]. As the interface is mediated through O 2p orbitals, the energy levels must be shifted such that the oxygen energy levels overlap[19]. The Fermi level must be matched then between the two materials, and if occupied states in one material overlap with unoccupied states of the other, electrons will flow in order to fill the unoccupied states creating charge transfer between the materials. This is typically understood to occur between metallic and insulting materials, but is relative to the band gap and the comparative Fermi levels of the two materials in question. For instance, charge transfer exists at the interface between insulating STO and $LaAlO_3$ and is known to cause an interfacial 2D electron gas [20]. We do however note that this picture of charge transfer neglects the complex quantum mechanical nature of electron orbitals in crystals, namely that charges are not so much discreetly transferred between atomic cations as much as the interfacial electron cloud mediated by the O 2p orbitals is shifted toward one side and changes the dielectric nature of the interface.

The relevance of this distinction is still debated, and its applicability in this work will be discussed[21, 22].

Understanding the relevant magnetic considerations for transition metal oxide materials and interfaces, we can now look toward the specific characteristics of the materials used in this study and how they change when brought into thin film and heterostructured forms. The

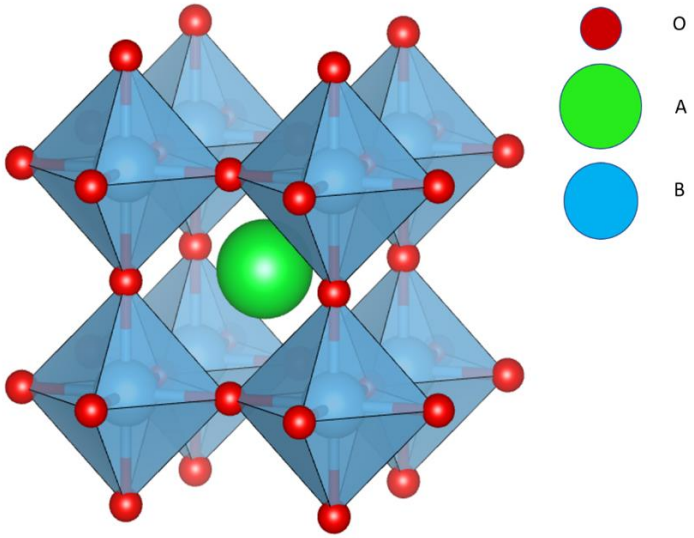

Figure 1.6. Crystal model for ABO_3-type perovskites, where A and B are alkaline earth metals and transition metals respectively. Oxygen octahedral cages are formed around the B site atoms.

materials in this study all fall under the perovskite crystal structure ABO_3, which entails an A-site cation at the center of eight B-site octahedrons formed by oxygen cages. While the shown structure in Figure 1.6 is a perfect square lattice with no tilt and rotation of the oxygen octahedron, this is not usually the case for perovskites, and most introduce some variation to this ideal, either from changes in relative lattice parameter, tilt and rotation of octahedral cages, or changes to unit cell bonding angles. Some materials such as $BaTiO_3$ can even introduce noncentrosymmetricity, where the A-site cation is shifted from the center of the unit cell [21]. Here we will discuss STO, SRO, LCMO, and CRO characteristics.

1.2. STO Characteristics and Preparation

Every sample in this study will use $SrTiO_3$ as the substrate material, as well as being used for heterostructuring in some cases. STO is used primarily due to its optimal structural parameters, with a purely cubic structure with no tilt or rotation and a useful 3.905 Å lattice parameter. This structure epitomizes the basic TMO structure seen in Figure 1.6, but when used as a substrate for tilted orthorhombic or tetragonal materials can induce a reduced interfacial tilting, as we will see in our measurements. The 3.905 Å lattice parameter puts it in the middle of most TMO pseudocubic lattice parameters, which means that we can use it to grow a host of TMO films with minimal film strain and uniform substrate contributions. A cubic to tetragonal structural change is seen in single crystalline samples around 104K, and this can affect the properties of films grown on STO substrates [23]. The magnetic and resistive properties of STO also make it particularly useful for use as a substrate material. STO is a highly insulating, weakly diamagnetic material with low coercivity[24]. Using an insulating material ensures that we primarily measure the characteristics of the grown films during resistivity measurements. The diamagnetic signal coming from STO substrates is weak and unique among our materials, making it easy to subtract from any magnetic signal obtained.

Single crystalline substrates are cut in the (001) direction, and this cleave direction affects the termination layer at the substrate-film interface and overall geometry of films grown on top of them. All STO substrates were prepared using a multistep etching process in order to ensure that the surface is clean and TiO_2 layer terminated. This termination is important, as it controls the termination structure of any grown films. The etching process follows these steps. sonication baths in ethyl alcohol, acetone, and deionized water for 5 minutes each in that order, then a 30 second etching in hydrofluoric acid, followed by 1atm oxygen annealing at 950°C for 3 hours. It

is known that different treatments can produce different surface symmetries, and as such it is important that we treat each substrate similarly[25]. Substrates that we use typically have a miscut angle below 0.1 degrees and a high degree of crystal uniformity, making them excellent substrate materials.

1.3. SRO Bulk and Thin Film Characteristics

The SRO crystal takes an orthorhombic form of the space group *Pbnm*, with a=5.567 A, b=5.5304 A, and c=7.8446 A [26]. In a pseudocubic notation, which is useful when trying to understand strain in thin film heterostructures, these translate to a_{pc}=3.930 A and c_{pc}=3.922 A. This crystal also has substantial tilt and rotation in the octahedral cages with an $a^-a^-c^+$ pattern in Glazer notation, with around 10 degrees of tilt in both directions [27, 28]. Glazer notation is a

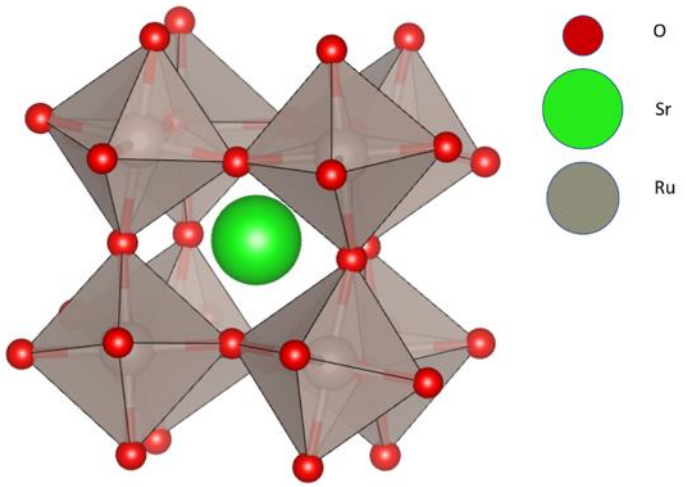

Figure 1.7. Model $SrRuO_3$ crystal structure. SRO occupies the *Pbnm* space group with Glazer notation $a^-a^-c^+$.

short hand for determining the rotation about each axis in a perovskite system. In this, the alphabetic notations describe which pseudocubic axis is being described, and axes are given the same letter if the axes lengths are the same. In this way, one can easily determine if the system described is cubic, tetragonal, or orthorhombic in pseudocubic notation. The positive and

negative signs describe if the tilt arrangements in that direction are in-phase (+) or out-of-phase (-). If no tilt exists in a given direction, then that axis is denoted with a 0 instead of the positive or negative sign.

In its bulk, SRO is an itinerant metallic ferromagnet. It is, however, referred to as a "half metal" in the single band Hubbard model[29] described by Equation 1.

$$H = -t * \sum_{i,j,\sigma}(d_{i,\sigma}^{\dagger} d_{j,\sigma} + d_{j,\sigma}^{\dagger} d_{i,\sigma}) + U * \sum_{i=1}^{N}(n_{i\uparrow} n_{i\downarrow}) + \mu * \sum_{i=1}^{N}(n_{i\uparrow} + n_{i\downarrow})$$

Equation 1.1

In this model, t represents the hopping energy between sites, U is the on-site Columbic repulsion between electrons of different spins also known as the Hubbard parameter, and μ is the chemical potential of the system. If t is much larger than U, it is more energetically favorable to hop between sites than stay in any 1 given orbital, which produces a good metal. In the opposite extreme, U is much larger than t and the wavefunctions of the electron orbitals do not overlap, making it energetically favorable to remain onsite. This is referred to as a Mott insulator. When t ~ U, as is the case in SRO, the system maintains a fermi-liquid behavior at E_f, but the onsite repulsion is not negligible. In SRO, Ru has a valence state of Ru^{4+}, with the Ru 4d orbital being split into t_2g and e_g bands by the crystal field with a band splitting of 3-4 ev. This means that 4 electrons are trying to fill t_2g, which only has 3 degenerate orbitals. This means that one orbital will be filled, which is energetically unfavorable due to the non-zero Hubbard parameter. This unfavourability shifts the effective DOS for the minority and majority spin bands from one another, making it more likely that conduction happens in the minority channel. This favored conduction of the minority spin channel is what drives the so-called Stoner ferromagnetism, as the itinerant electrons have a preferred spin direction. This model for the metallicity and

ferromagnetism in SRO is not completely settled, as deviations from this standard model have been recently found and point toward a local spin-splitting of t_2g present even above T_c [30].

Ruthenates, and SRO in particular, has also been studied for its large spin-orbit coupling (SOC) term, which has been linked to topological effects and magnetic skyrmions [31, 32]. SOC is a relativistic effect between the intrinsic spin magnetic moment of electrons and the observed magnetic field due to its orbital motion around a charged nucleus. The Hamiltonian term associated with SOC can be written as

$$\Delta H_{SOC} = -\frac{g}{m_e^2 c^2}\frac{\delta U(r)}{r\delta r} L \cdot S \qquad \text{Equation 1.2}$$

Where U(r) is the potential energy of the electron at a distance r from the atomic nucleus, g is the g-factor associated with the spin magnetic moment (≈2), and L and S are the orbital and spin angular momentums respectively [33]. This effect is always present in atomic physics, but the effect becomes more pronounced for larger atoms with large orbital angular momentums. Interfaces in strong SOC systems can produce Rashba splitting of spin bands in k-space, lifting their degeneracy and allowing for interesting effects such as spin currents and spin-hall effect [34–36].

As the dimensionality of SRO is reduced, these metallic and magnetic properties shift. When looking toward this thin film limit, the influence of the substrate materials structure on the film is of the utmost importance. It has been shown that ruthenate magnetism is very susceptible to change through lattice strain, and octahedral tilts can be altered by interfacing with other materials [37, 38]. In this study, we grow on cubic STO (001) which have a smaller in-plane lattice parameter than SRO, meaning that SRO will be under compressive strain and that an elongation of the c-axis is expected in these films [39]. Above 5 unit cell (uc) film thicknesses,

SRO remains metallic and ferromagnetic, but as thickness is reduced below 5 uc, both the ferromagnetic order and metallicity degrade [2]. The origin of the MIT is still under investigation, and may be due to dimensional confinement, increased density of site disorder, or surface reconstruction [2, 40, 41]. This loss in metallicity would also explain the disappearance of ferromagnetism, as half-metallicity is a prerequisite of Stoner FM.

1.4. LCMO Bulk and Thin Film Characteristics

The other material of principle interest in this work is $(La_{.67}Ca_{.33})MnO_3$. Structurally, this material is similar to SRO in that it is also orthorhombic with a=5.465 A, b= 5.479 A, and c= 7.723 A and part of the same *Pbnm* space group [42]. This translates to a pseudocubic in-plane lattice constant a_{pc} = 3.86 A, which is substantially less than seen in SRO. The tilt angle of the oxygen octahedron is about the same between SRO and LCMO, with about ~10 degrees of rotation [42].

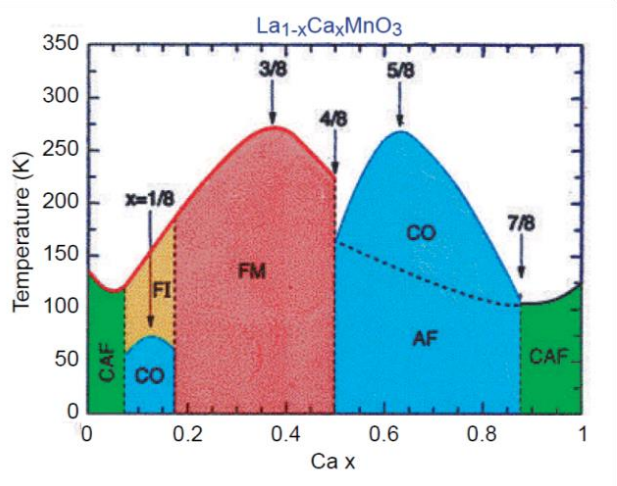

Figure 1.8. Doping phase diagram of 4 distinct doping regions are formed with different magnetic and resistive properties.

Manganites have been known to host a large variety of interesting physical phenomena, including metal insulator transitions, colossal magnetoresistance, and charge/orbital ordering [3].

In $[La_{1-x}Ca_x]MnO_3$, it is important to note that the phase diagram, shown in Figure 1.8 and reproduced from [43], shows a clear distinction between four major Ca doping regimes. These regions include an AFM insulating phase below 5% Ca doping, a FM insulating phase between 5-20%, a FM metallic phase between 20-50% Ca doping which we examine during this study, and an AFM insulating phase above 50%. $LaMnO_3$ is a Mott insulating A-type antiferromagnet which follows the Goodenough-Kanamori rules of manganite superexchange, in which we recall that virtual electron hopping between orbitally hybridized magnetic cations is antiferromagnetic when the hybridized orbitals are both half-filled [44, 45]. The addition of Ca doping between 5-20% leads to a FM insulating phase, which in the past has been attributed to spatially separated regions of the LMO insulating phase and more highly doped FM metal (FMM) phase [46]. Recently, however, studies have argued instead for a frustrated glassy phase with large scale magnetic polarons [47]. Our crystals occupy the FM metal phase between 20-50% Ca doping, where the metallicity and ferromagnetism are due to double exchange between the half-filled Mn^{3+} e_g orbitals and the empty Mn^{4+} e_g level. As previously discussed, the Hund's exchange prefers the system to occupy the maximal spin state and preferentially aligns the hopping e_g electron. This ties the magnetism in the system to its hopping-mediated metallicity. One of the main contributing factors to the hopping parameter, or its commiserate single electron bandwidth W, is the A-site ionic size [3]. If the ionic size is decreased, as is the case as the Ca doping moves above 50%, W is reduced and the double exchange domination of the electronic characteristics is diminished. In this region, other effects such as repulsive coulomb interactions, collective Jahn-Teller (JT) distortions, and charge/orbital ordering begin to take precedence [3]. This charge ordered state prefers both a localization of electrons and an ordering of Mn^{3+}/Mn^{4+} cations such that the superexchange occurs between similarly filled e_g orbitals, favoring an AFM

alignment [48]. The competition between the FMM and the CO states is evidenced by the dip in ordering temperature near the phase transition, signifying that both states exist above and below the transition doping level.

As the thickness of $L_{.67}C_{.33}MO$ is reduced, the material enters a "dead" zone, where it loses both its metallicity and its magnetic order. In this way, LCMO shows both a temperature and thickness dependent MIT. LCMO grown on STO (001) shows both a complete loss of metallicity and a substantial decrease in T_c as the films are brought below 10 uc [49]. The role of oxygen vacancies and disorder, structural distortion, and dimensional confinement must be considered in these ultrathin samples. The introduction of oxygen vacancies have been shown to drastically reduce the MIT transition temperature in LCMO films and has been associated with an increase in the Mn^{3+}/Mn^{4+} ratio, returning the system to the ferromagnetic insulator (FMI) phase [50]. Thin films are particularly susceptible to disorder effects, as interface induced strain can increase scattering sites and increase resistivity. While interfacial structural deformations have not drastically altered the properties of relatively thick (~170nm) LCMO films, it should be noted that in ultrathin films of similar manganates, the role of interfacial oxygen octahedral distortion is of paramount importance and can be used in order to enhance magnetic characteristics [51, 52].

1.5. CRO Characteristics

Though this work is focused on heterostructures of SRO and LCMO and the interesting interfacial physics they present, it is advantageous to use other similar materials in the same heterostructure arrangement in order to isolate the characteristics of interest in the proposed SRO-LCMO heterostructure system. Toward this end, we have utilized CRO and STO as buffer layers in between LCMO. Using these perovskites in tandem with SRO buffer layers will allow

us to probe the effects of interfacial octahedral rotation distortion, metallicity, and magnetism on the observed heterostructure properties. CRO is another orthorhombic *Pbmn* crystal with lattice constants a=5.36 A, b=5.54 A, and c=7.68 A, giving it an equivalent in-plane psuedocubic lattice parameter of 3.84 A [27]. This places the epitaxial strain between films of CRO on STO(001) at 1.5%, which is larger than the 1% for LCMO films and .7% for SRO. The oxygen octahedral cage tilt and rotation is also the largest of the group, with an in plane lattice rotation of ~16 degrees [53, 54]. This means that heterostructures with CRO buffer layer will likely increase the tilt and rotation of interfacial O octahedron as compared to SRO heterostructures. Increased interfacial tilt and rotation is often linked to a reduction in ferromagnetic response in perovskite manganates and is attributed to the double exchange's dependence on the B-O-B hybridization angle [55, 56]. Though initially thought to have some antiferromagnetic order, CRO has been shown to have no long range magnetic order down to at least 4.2K [57–59]. It is however metallic, and because of its similar band structure and Curie-Weiss constant to SRO, it is assumed to be near to an insulating transition[60, 61]. Light doping of CRO with other elements have been shown to drastically alter the metallic/insulator and magnetic/nonmagnetic characteristics, and is attributed to the d-band width being too small for magnetic stabilization but not so small that the film becomes insulating [62]. By substitution of CRO buffer layers for SRO, we will be able to maintain the metallicity and potentially crucial Ru-O-Mn interface of the SRO samples while eliminating any magnetic stabilization that may come from SRO.

1.6. Ruthenate-Manganite Heterostructures

This study will not be the first to look at heterostructures of perovskite manganites and ruthenates, and this work will expand upon that body of knowledge. In LSMO-SRO films, much attention has been given to the positive exchange bias seen in the system and the predicted antiferromagnetic coupling between the Ru and Mn moments that produces it [63–67]. In this system, the Ru layer acts as a "pinning" layer because of its strong magnetocrystyline anisotropy that can influence the more easily flipped Mn moments. If the coupling between these layers is antiferromagnetic ($J_{ex} < 0$), then as the field approaches zero, the J_{ex} becomes greater than the external applied field term H and flips the Mn layers. This flip then increases the reversed field felt by the pinned layer, shifting the hysteresis toward the positive [63]. Theory attributes the negative J_{ex} coupling to a polarized O 2p orbital that produces an asymmetric spin density that must be compensated, and predicts exchange bias to be highly dependent on interface intermixing of Mn and Ru [67]. This interfacial AFM coupling mechanism is yet to be confirmed however, and the role of site intermixture must also be investigated experimentally. This will be a main focus of this dissertation work. The two-step mechanism for understanding the exchange bias describes the layer coupling at low temperature, but at higher temperatures between 60K and 150K (thin film T_c of SRO) a more unconventional magnetic hysteresis emerges with 3 distinct zones [64]. This behavior is predicated by the assumption that the heterostructure is ferrimagnetic at low fields, which is consistent with differences in the bulk values for magnetic moment per B-site atom. A reduction in the magnetocrystalline anisotropy of SRO above 60K allows for magnetic domains to form in the SRO layer before LSMO. These SRO domains flip as the field is reduced, but because the Mn moments are larger and coupled

antiferromagnetically to Ru, a step is formed. The Mn moments eventually flip, leading to a three-step hysteresis.

LCMO-SRO heterostructures have also been studied in limited ways in the past. Most notably related to this work, a study by Gong *et. al.* looked at the role of magnetic anisotropy in LCMO-SRO heterostructures where the thickness of SRO was varied as the thickness of LCMO was held at 16 uc [68]. They found that the magnetic easy axis of the system changes from IP to OOP as the thickness of SRO is increased, consistent with a stronger magnetocrystalline splitting in SRO. They also note a 300% increase in the observed magnetoresistance between the MR of the 16 u.c. LCMO-1 u.c. SRO film and the pure 50 nm LCMO film at 20K. They do not observe any increase in MR at temperatures above the T_c of SRO, and they therefore attribute this MR increase to interfacial scattering caused by the nonuniformity of the strained magnetic anisotropy. It should be noted that very little has been revealed on the possible mechanisms for the enhancement of MR in manganate-ruthenate heterostructures. Other studies have looked at other doping levels of LCMO above the FM-AFM doping-phase boundary and found that strain has a drastic effect on the strength and even sign of the coupling constant between Mn-Ru layers [69].

After review of the existing state of research on SRO and LCMO, both separately in bulk and thin film form and together in heterostructures, we find scientific issues of merit that we are well suited to investigate. First, the nature of the interfacial coupling between manganites and ruthenates is of extreme importance given the amount of weight it is ascribed in determining the magnetic behavior in extremely thin films. We will investigate this coupling by looking to the interfacial structure and composition, with particular attention to the various thickness regimes of both LCMO and buffer layers above and below their dead-layer thicknesses. This will allow us

to isolate which effects are due to dimensional confinement, structural deformation, or interface elemental differences. This will be highly influenced by the artificial control we will implement in LCMO based on the buffer layer used, with FM metal SRO, paramagnetic metal CRO, and paramagnetic insulator STO used here. Secondly, we also find that studies of LCMO in the extremely thin limit below 10 u.c. are exceedingly rare, presumably because they are thought to be completely below its dead layer thickness. The nature of this dead layer is of particular interest throughout thin film research, and enhancement of properties in the ultrathin regime are paramount. We find from our work that LCMO heterostructures can still exhibit novel FMI behavior below its single film dead layer thickness. With this work, we will better understand the nature of this separation of ferromagnetism and metallicity by examining the structural, magnetic, and resistive behavior of the films.

Chapter 2. Instrumentation

2.1. Film Growth

The purposed project will entail the use of various experimental techniques in order to create the necessary materials and examine their properties. Of primal importance is the growth technique, namely pulsed laser deposition. This method is useful for growth of ultrathin films on top of prepared substrates and necessitates a high power UV excimer laser that is capable of spallating material from a target.

When the laser is activated, the combination of noble gases, in our case Krypton and Fluorine, are put into an excited state by the high voltage applied in the laser tube. In this excited state, Kr and F, which normally do not form chemical bonds, can form a molecule called an excimer. This KrF gas is then allowed to relax back down, at which point it dissociates once again and releases a UV photon in the process at the 248nm wavelength. Our laser set up can operate between a 1-10 Hz repetition rate and with various power outputs between 200-600mJ, which are two of the possible growth parameters we can manipulate in order to optimize any thin film growths we undertake. The laser is focused onto a target of the material of interest in its bulk form, usually purchased from a supplier of high-quality crystals. The focused beam has a high energy density, typically on the order of 1J per cm^2 per pulse. Due to the high power and short pulse length (~25ns), the material hit heats to very high temperature. At the same time, the UV laser light has enough energy to strip the electrons off the material it hits, creating a plasma on the surface.

This superheated plasma is ejected as a vapor from the surface in a visible plume. The desired substrate is placed in the path of the plasma, where the material will deposit in one of

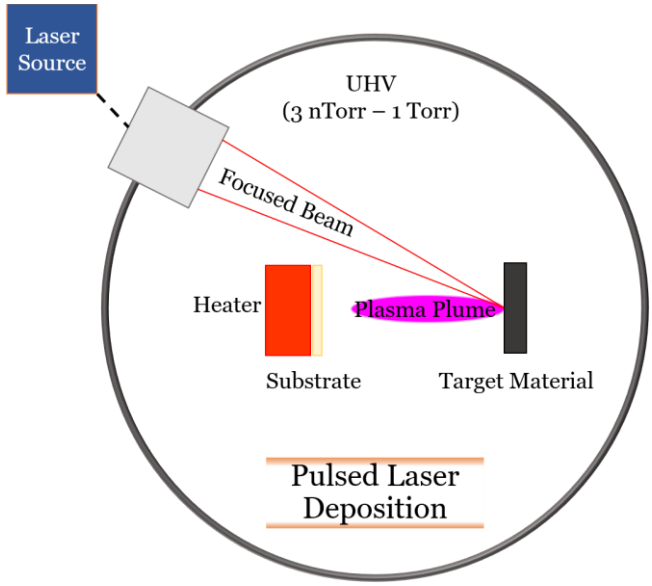

Figure 2.1. Schematic of PLD setup. Laser hits desired target in vacuum chamber on rotating carousel and emits plasma onto nearby substrate. Laser plume shape and size depends on material spallated, laser energy, and chamber pressure.

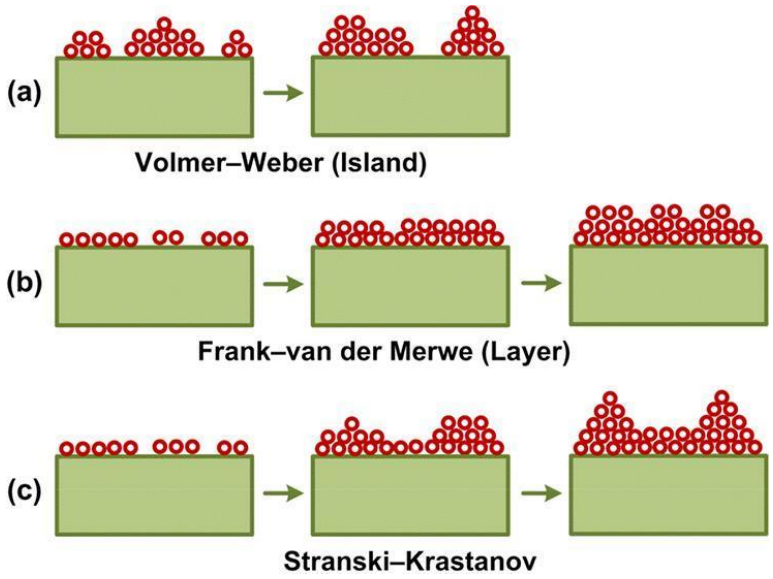

Figure 2.2. Possible growth modes during PLD. Layer-by-layer (or Frank-van der Merwe) is ideal for most thin film growth, though Stranski-Krastanov is usually acceptable. Not pictured here are collimated, or 3D, growth and step-flow mode. Reproduced from [67].

five possible growth modes.

Growth can occur either in a layer-by-layer, step-flow, island, mixed, or 3D manner. Layer-by-layer growth, also known as Frank van der Merwe growth, is usually ideal, and occurs when the deposited material begins to form single layer islands of the deposited material on the substrate. These islands form randomly and independently across the surface, and as more form as more material is ablated onto it, the islands will begin to encounter one another and form larger islands. As the growth continues, these islands grow in size until the entire surface is covered with the desired material. Then and only then does the next layer of the ablated material begin to form on top of this previous layer, and so on. This growth mode is ideal for high degrees of crystallinity and uniform characteristics in the samples grown. Layer-by-layer is similar to Volmer-Weber growth, though the latter does not achieve the same degree of film crystallinity as the former. In this mode, islands begin to for as they do in van der Merwe, but before the first layer is completely covered, the islands begin to form the next layer on top of the previous layer. This creates large multiunit cell islands on the surface of the film. An intermediate stage between these two modes is the Stranski-Krastanov mode, which may not finish every layer completely before the next unit cell starts to grow on the Volmer-Weber islands, but layers do eventually finish and can create an rough film. Each of these growth modes are shown in Figure 2.2 [70]. Collimated, or 3D growth, is an extreme version of Volmer-Weber, where there is next to no spread across the substrate surface, and spires are formed on the surface. This occurs when the incoming material has very low surface mobility, which can be affected by growth temperature and laser energy, or a preferred OOP growth direction. Step-flow growth is slightly different in that it only occurs when terraces exist in the substrate material used (which is usually the case). These terraces form natural points for ablated material to nucleate, meaning that instead of

islands, the layers form out from the step-edges, though still in single layers. Therefore step-flow and layer-by-layer growth are usually both acceptable in terms of the quality of grown materials.

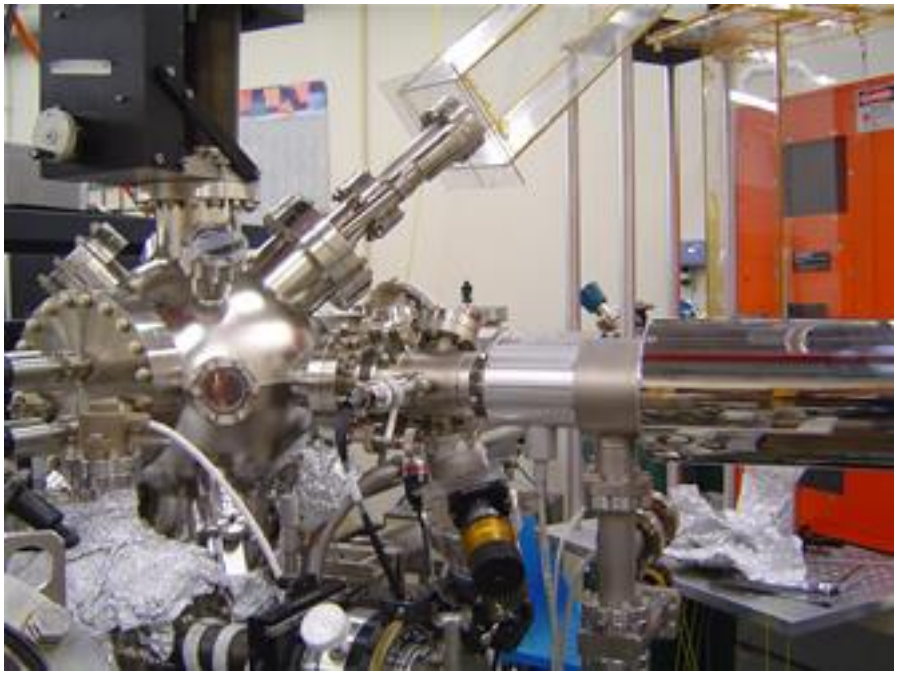

Figure 2.3. Experimental PLD setup. Laser (orange box in back) is a Lambda Physik COMPEX 201. Mirrors and lenses focus the laser beam onto a material target inside growth chamber (left). System allows for quick *in-situ* transferring of different substrates.

Achieving the correct growth mode depends highly on the growth parameters used, which can affect the mobility of adatoms, the surface energy of the substrate and film, and nucleation rate. Our lab can control for oxygen partial pressure (UHV-1torr), substrate temperature (RT-800º C), laser energy (200-650mJ per pulse), laser repetition rate (1-10Hz), and position relative to spallation target, all of which can drastically affect the growth of the desired films.

Quickly determining the type of growth mode occurring and the overall quality of the film can be important when it often takes many attempts with different growth conditions in order to get a sample to grow with the desired quality. This can be achieved with Reflection High

Energy Electron Diffraction. This technique uses an electron beam produced from a high-voltage tungsten filament that is then focused by a series of grids inside the apparatus. This controllable focused beam is directed at a phosphor screen that luminesces when the e-beam strikes it. Without any interfering materials, the beam makes a bright dot on the screen that can be recorded with a CCD camera. If, however, a substrate or film is placed in the beam path, the electrons can interact with the material and diffract through its lattice, obeying normal Bragg's law considerations. These diffracted electrons leave the material and form a diffraction pattern on the phosphor screen. The formed spots arrange in concentric circles around a central electron beam spot as a result of their different scattered wave vectors. This can be understood as an elastic scattering of electrons with wavelength λ and wavevector $k_0 = 2\pi/\lambda$. As this is an elastic scattering process, incoming electrons have the same incident and reflected wavevector, and this reflected wavevector forms the Ewald sphere of radius k_0 in reciprocal space [71].

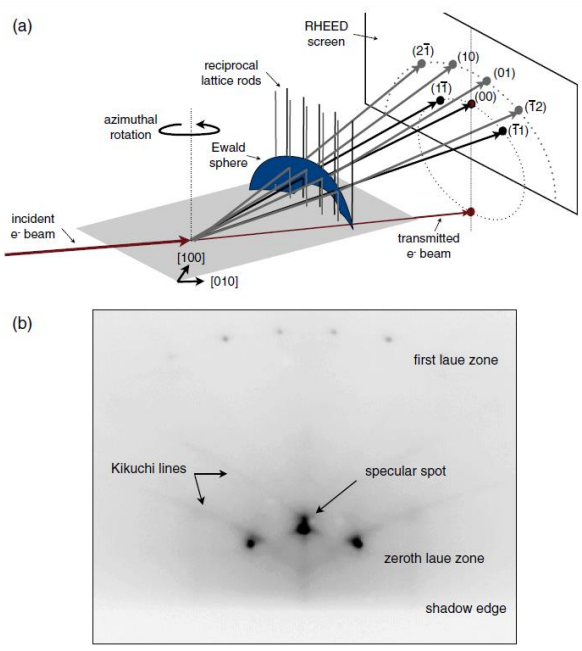

Figure 2.4. a) Illustration of Ewald sphere construction of observed RHEED pattern. Reflected electrons form diffraction patterns based on the intersection of the reciprocal space crystal lattice with the incident electron beam's Ewald sphere. Reproduced from [68].

Because RHEED only probes a thin amount of the crystal approaching the 2D limit, the reciprocal space construction of the crystal points instead forms infinite rods perpendicular to the surface of the material. These rods intersect the Ewald sphere, at it is at these points that constructive interference occurs and bright spots are observed. The rods intersecting the sphere form along planes that intersect the Ewald sphere, and when they are mapped onto the 2D phosphor screen they form Laue spheres, which appear as concentric circles around a central point. The entirety of the forward scattered Ewald sphere intersection points are theoretically observable in this construction, however in practice usually only the first few Laue zones are seen.

By monitoring the intensity of the spots observed using a CCD and related software, as well as observing any changes in the pattern formed on the screen, the growth mode and growth time per layer can be measured. The growth mode is determined by the appearance of the diffraction pattern observed. Layer-by-layer growth is observed when the spots formed are in a clear semi-circular pattern, as is usually the case before growth, and are maintained throughout the growth. Step-flow growth is seen when the small spots that had been seen originally morph into streaks on the screen. This is due to the material having different thicknesses across a single terrace but growing at the same rates. These lines should be largely uniform, without any spots forming within the lines signifying the formation of spires. If the growth is sub-optimal and 3D growth is occurring, multiple sets of spots will begin to form in the RHEED pattern not along the Kikuchi lines, which then denotes the presence of multiple columns on the surface that can scatter the incident electron beam. It is also possible to have growth conditions so far from the optimal growth parameters that the initial spots give way to pure background noise, which shows that no pattern is occurring on the surface and scattering events are varied and rampant. The time

necessary for the growth of a single layer is also useful information in film growth, and this can also be monitored with the RHEED setup. Software tracks given regions on the phosphor screen and measures their respective intensities. If a spot is observed through a full layer of a layer-by-layer growth, the intensity of the diffracted beam follows a characteristic intensity drop and resurgence. This oscillation in intensity is due to the nature of PLD film growth, where individual islands are formed as the layer builds. When many individual islands exist, the incident electron beam can be reflected by many of the islands and lose some of the beam intensity in the scattering process. This lowers the spot intensity seen on the screen, until it reaches a minimum at half coverage of the surface when the highest number of islands exist. As the coverage begins to rise, the intensity of the spots will resurge and become brighter until they are at their brightest when the layer has reached one hundred percent coverage. The process ideally repeats itself for every layer grown, creating an oscillation pattern that shows how long each layer takes to form and giving information on the growth dynamics of the particular growth. This information allows us to highly control the number of layers grown in a film, which is of paramount concern when thickness dependent studies are undertaken.

2.2. Crystal Characterization

Though RHEED is an important first step in understanding the quality of the ultrathin films grown, it is not sufficiently quantitative to understand the crystallinity of the film or make any statements on whether the material grown was in fact the desired material, as changes in growth conditions can alter stoichiometry and composition. To address these concerns, we use

two separate x-ray characterization techniques, namely Angle-resolved X-Ray photoelectron spectroscopy (AR-XPS) and X-Ray diffraction (XRD).

Modern high-resolution XPS was developed by Kai Siegbahn in the 1950's, and has been used widely ever since. The technique can be used to understand the atomic makeup and valence state of materials, and can also illustrate any changes in different layers of films with the addition of angle-resolved capabilities. An X-Ray source is attached to a vacuum chamber, here *in-situ* with the growth vacuum chamber, and collimated and monochromated by a series of mirrors and lenses. It is important that this set-up be conducted in UHV, as the emitted electrons need to be able to reach the analyzer and any gas pressure will scatter electrons, losing energy and lowering

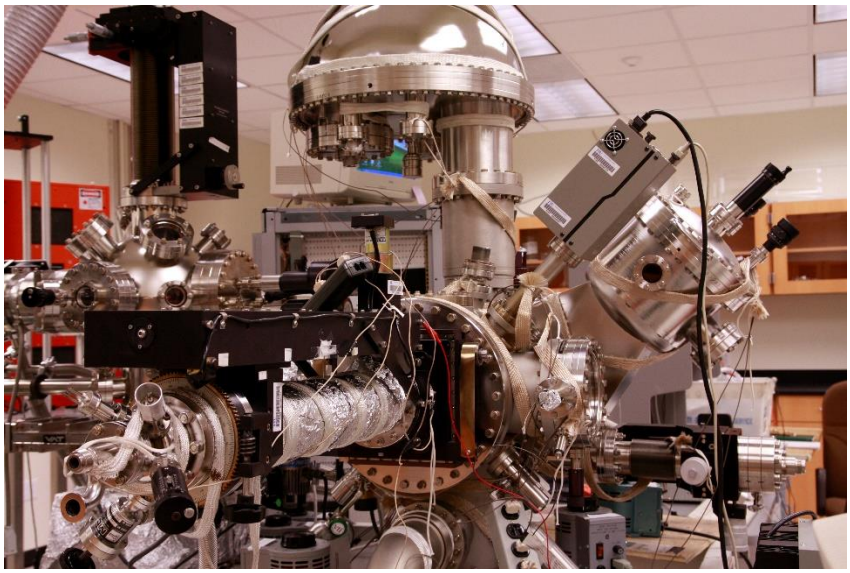

Figure 2.5. Experimental Setup of XPS. Monochromator (top right) takes light from x-ray source (bottom right) and reduces the line-width of the beam, as well as collimating it to hit the desired target. The ejected electrons are then focused through the chamber by electrostatic lenses into the energy analyzer (top).

counts detected. The X-ray source used produces Al K-alpha X-ray at 1487 eV. Though ideally the source would only produce this exact wavelength, there is an inherent FWHM (Full-Width Half-Maximum) to the line of .43 ev, and with any imperfections in the experimental setup, the

FWHM can increase. Therefore a monochromator is necessary in order to increase the resolution of the source. Our SPECS setup can reach a realworld FWHM limit of .44eV between the source and analyzer, though anything under .6eV is acceptable. The beam must also be focused with collimators in order to focus onto the desired sample. As the x-rays hit the material, electrons are emitted according to the photoelectric effect

$$E_{photon} = B.E._{electron} + K.E._{electron} + \phi \qquad \text{Equation 2.1}$$

The basis of the technique is in measuring the kinetic energy KE of the emitted electrons to quantify the binding energy BE of the core levels that those electrons were ejected from. Because the work function φ of the analyzer is known, the BE of the emitted electrons can be determined by only selectively measuring a certain KE electron with the energy analyzer. Our SPECS energy analyzer accomplishes this with a series of electrostatic lenses and a spherical energy analyzer. The lenses take the widely scattered electrons leaving the surface of the material and focus them to go through a slit in the base of the energy analyzer. The analyzer itself is comprised of two concentric hemispheres placed under specific voltages and separated from each other. The focused electrons are allowed through the entrance slit and are then subject to the applied electric field inside the analyzer. The E field acts as a centripetal force on the electrons, and will move the electrons towards a CCD on the opposite side of the hemisphere. By correctly setting the voltages of the hemispheres and creating what is known as a pass energy,

only electrons with this pass energy will make the correct path toward the camera and be detected.

To perform a measurement, the pass energy is held constant while the electrostatic mirrors are voltage tuned in such a way as to only focus electron energies with a certain energy into the sphere, where additional correction of electrons with incorrect energy will occur. The resolution of the measurement can be controlled by the slit width of the analyzer, radius of the analyzer itself, the pass energy, and the inherent line width of Al K-alpha as previously discussed [72]. The energy of the measured electrons and their relative intensities are directly related to the core level binding energies of the elements in the sample. The binding energy is element

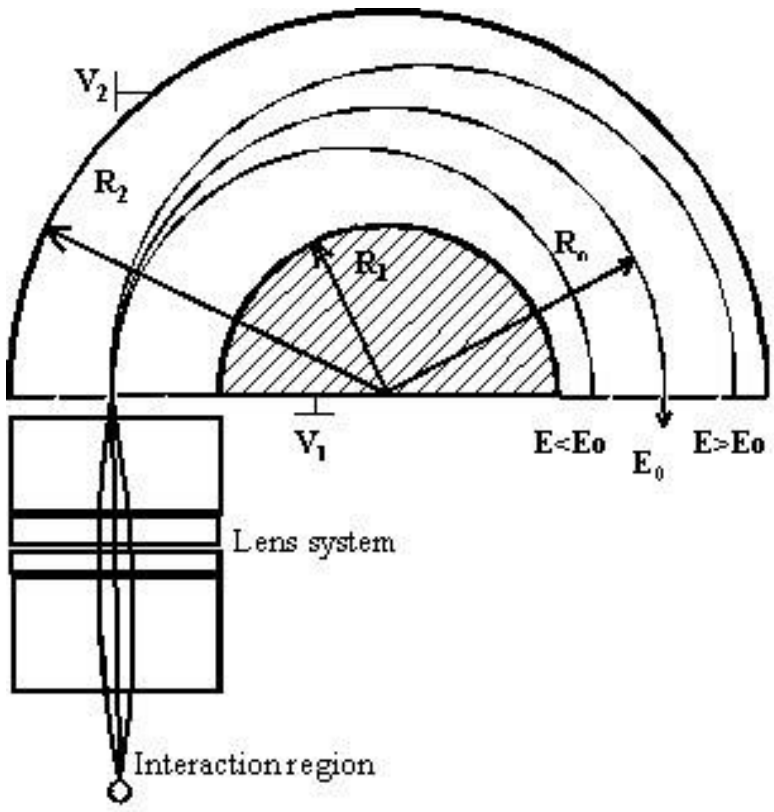

Figure 2.6. Schematic of XPS hemispherical analyzer and lens setup. The two separate hemispheres are kept at different voltages to allow only electrons with E_0 pass energy to escape the exit slit and be recorded. Reproduced from [69].

specific, and can therefore be used to understand the composition of the material. This energy is also dependent on the valence state of the material, as a higher valence state (ie more positive) produces less screening in the element and therefore produces a higher binding energy, and the inverse applies to a lower valence. Analysis of this data can then produce information on the states of the elements in the sample, which can lead to understanding the stoichiometry, and well as ensure that no contaminating substances are present that might later affect other measurements.

This technique can be furthered with the addition of angular resolution. In this case, the sample is rotated with respect to the energy analyzer direction, which allows fewer electrons to be emitted in the direction of the analyzer, as the path electrons must to take to be ejected from

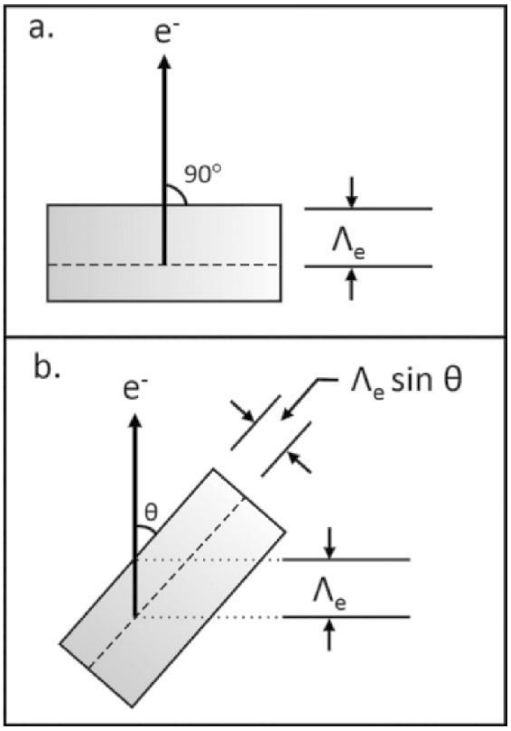

Figure 2.7. Model of angle resolved XPS. By rotating the sample w.r.t the direction of the XPS analyzer, the emitted electrons that have a long enough mean free path Λ_e to escape come from a thinner slice of the material, making the analysis more surface sensitive. Reproduced from [70].

the same layer increases. Therefore the electrons that do escape the sample are only from a thinner slice of the material, as only electrons from the top layers have a long enough mean free path Λ_e to escape along that direction [73]. Using this technique allows us to look for changes in the composition of samples as a function of penetration depth.

Many techniques can be used to understand the crystallography of the ultrathin films we grow, but one that is both powerful and efficient in XRD. This is an x-ray technique that utilizes simple Bragg diffraction principles and precise positioning in order to determine lattice spacing, thickness, and reciprocal space maps (RSM's). A Cu K-alpha source is mounted on a rotating arm inside a lead-shielded measurement house. Across from the source a scintillation detector is mounted on a rotating arm as well. These arms will rotate about a material in the center that can also be moved. For simple powder diffraction, the material is ground so that many different

Figure 2.8. Panalytical XRD setup. Source (left) and detector (right) are on rotating arms with a high degree of angular resolution (.001 degrees). Reflection-transmission stage for powder diffraction shown in center. Chi-phi stage not shown.

crystal orientations are represented throughout the sample, which can then be spun and averaged over the course of a measurement in order to understand the structure of the unit cells of the crystals. In thin films, we are interested in the overall crystallinity of the films grown, as well as the unit cell lattice parameters, and therefore special care must be taken in order to align the source and detector with the film's optimal direction. This is done through alignment with a Chi-Phi rotation stage that can move the sample along 5-axes, which maximizes the signal-to-noise ratio and ensures we are in line with the crystal direction.

Once the alignment has been completed, different measurements can be done to glean different information about the film. A rocking curve (RC) is used to understand how well the different unit cells in the film are locked into the sample out-of-plane (OOP) direction. Every film is comprised from individual unit cells of the grown material, and it is possible that during the growth, one unit cell rotates with respect to another. This creates a crystal with different facets, and the more rotated unit cells exist, the less well-defined the crystal and its resultant properties, as it may result in defects and commiserate anomalous properties. To probe these different orientations, the film must be "rocked" in-plane so that only unit cells with the desired measurement orientation satisfy the Bragg condition and are measured [74]. In practice, actually rocking the film is less practical than moving the x-ray source angle, which achieves the same goal of selecting for a specific OOP orientation. This is called an Omega scan, as it moves the source angle w.r.t the in-plane sample direction, which is called omega in most XRD experiments. By determining the FWHM of these RC's, the span of the different orientations is determined which tells us about the relative crystallinity of the grown film. Typically any film with FWHM under .03 degrees would be considered good, though considerations are made depending on the substrate quality.

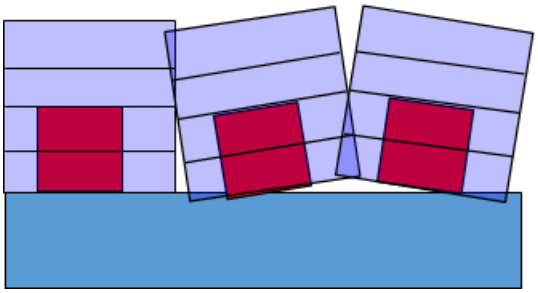

Figure 2.9. Model of mosaic spread in crystal structures. Seed crystals grow at slight misalignment angles, and when they meet form low-energy domain boundaries. This mosaicity is quantified by rocking curve scans. Reproduced from [71].

XRD can also tell us about the thickness and OOP lattice parameter of the unit cells in the grown film. This can be done both by theta-2theta scans, also known as coupled scans, and by RSM's. We will first talk about coupled scans. These work by examining the symmetric peaks of the films grown, meaning that we probe only crystal directions that satisfy the Bragg equation

$$2d * \sin(\theta) = n * \lambda \qquad \text{Equation 2.2}$$

and also emit reflected photons at the same angle as the incident omega angle. Moving both the source and detector in tandem achieves this outcome, hence why it is "coupled". The position of the peaks observed has a direct relationship to the OOP lattice constant of the unit cells, as these are the scattering planes that need to satisfy Braggs law. The exact determination of the lattice constant depends on the type of crystal structure being analyzed, as cubic structures produce different Bragg spacings relative to OOP lattice constant than, for example, a monoclinic structure with the same OOP lattice constant. Determining the thickness of the sample from these scans is done by looking to thickness fringes formed around the central film fringe. These extra fringes correspond to inference between the photons hitting the surface and those hitting the

interface, which leads to phase differences based on the thickness of the film. The thicker the film, the bigger the phase difference, which leads to a smaller distance between peaks in the theta-2theta scan. The thickness of the film is quantified by

$$t = \frac{(n_1 - n_2) * \lambda}{2 * (\sin(\omega_1) - \sin(\omega_2)}$$ Equation 2.3

where t is the thickness of the film, n is the order of the thickness fringe, and ω is the omega angle of the fringe. By a simple division of this thickness by the already determined OOP lattice parameter, the number of unit cells is determined and can be corroborated with the number of RHEED oscillations seen during growth [75].

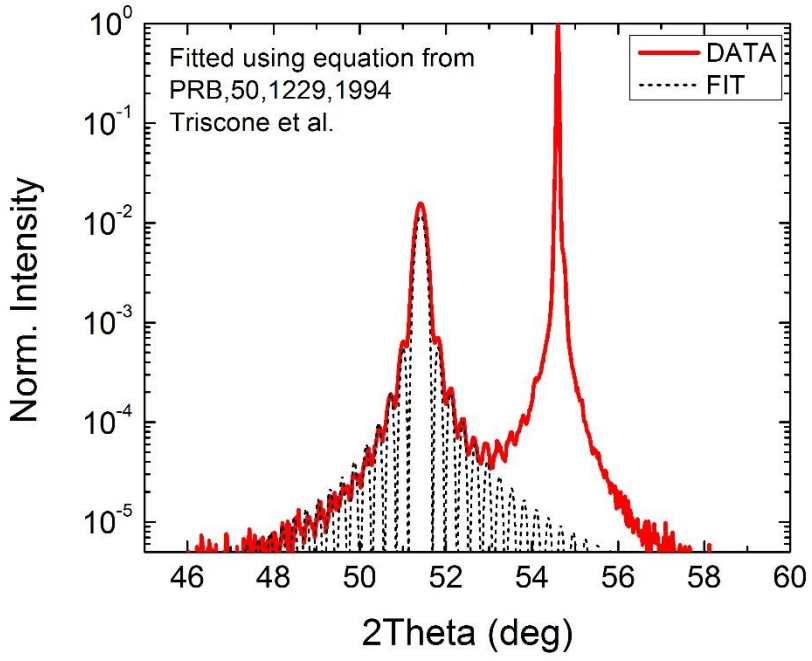

Figure 2.10. Example Coupled Scan. Substrate peak is the most pronounced as there is more of that material than the film, but the main film peak and subsequent thickness fringes are observed. The OOP lattice constant and thickness of the film can be determined from this. Reproduced from [72].

Reciprocal space mapping is another powerful use of this setup, and it can also be used to measure many of the same parameters as a coupled scan, though it has the added benefit of being able to quantify the in-plane lattice parameter of films grown. Ideally, films grown on top of substrates would have the same in-plane lattice parameter as the substrate itself, meaning that no defects exist at the interface and there is a smooth transition from the substrate to film. Not all films are perfectly strained however, and defects can form at the interface if the growth is sub-

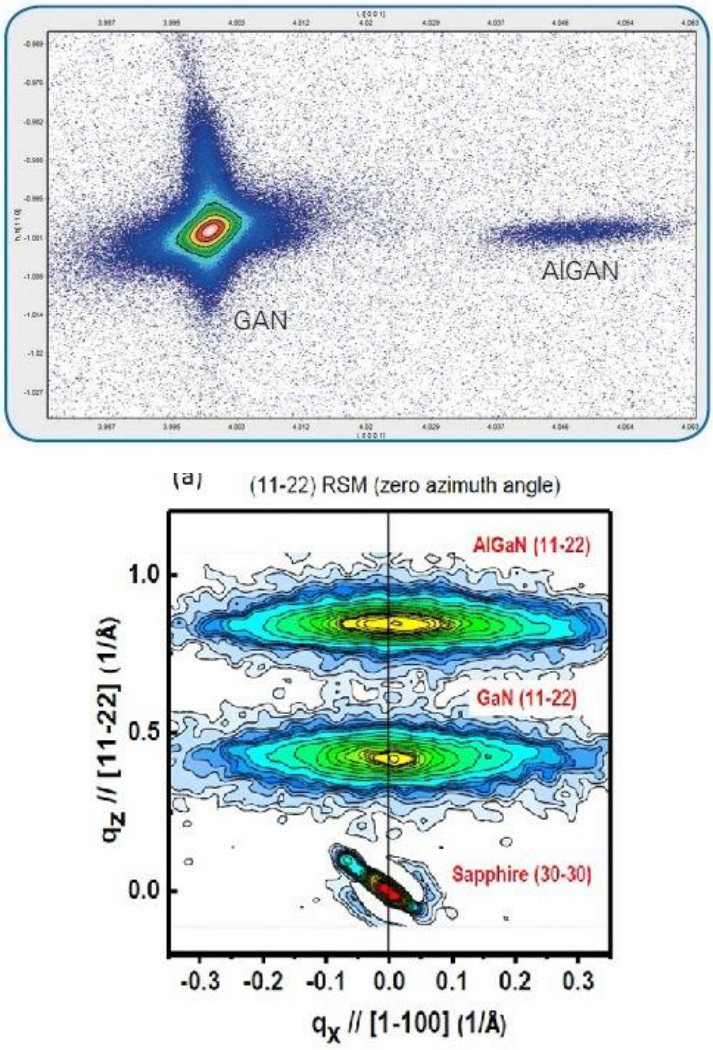

Figure 2.11. RSM's for two different materials. Illustrates the difference between a fully strained film (top) with a highly relaxed film (bottom). The left figure's film is only has minimal broadening in the qx direction, indicating a high degree of strain. The right figure shows a film that has the opposite behavior. Reproduced from [73] and [74].

optimal. RSM's probe this by moving omega and 2theta but not forcing them to be exactly in tandem, but allowing one to move while the other stays in place. This allows for otherwise restricted zones in the reciprocal space of the lattice to be probed. Perfectly strained films do not deviate from the substrate's in-plane lattice parameter, which is seen here as a thin line in the RSM pattern. If the film is relaxed from the substrate however, a broadening of the film peak occurs[76, 77]. The amount of broadening and the direction of it can be used to understand the type of relaxation occurring and the extent. This effect can only be observed at off symmetric hkl peak, such as -103, as symmetric peaks do not give any information in the reciprocal space q_x direction which is necessary to quantify the in-plane relaxation.

Electron microscopy techniques have become crucial in thin film research and can provide atomic scale (sub-Å) imaging of surfaces and sample cross-sections. This is due to the development of point-probe electron sources and sophisticated imaging techniques that allow us to make use of the small wavelength of electron beams (on the order of picometers) relative to traditional optical microscopy techniques that typically utilize ~nm scale sources. In particular, the cross-sectional electron microscopic techniques require precise control of the lensing and electron source as the technique is inherently diffraction dependent. This allows experimentalists to look at the structural evolution of films are their thickness increases, which is invaluable in the study of thin film interfaces and defect formation.

A schematic of a modern STEM apparatus is shown in Figure 2.12 along with the wide variety of potential techniques that such a system can provide. Of primary importance in this work are the high-angle annular dark field (HAADF), atomic resolution parallel electron energy loss spectroscopy (EELS), and annular bright field (ABF) techniques. HAADF images provide a $Z^{1.7}$ dependent image of atomic placement that allows for a degree of intensity analysis given

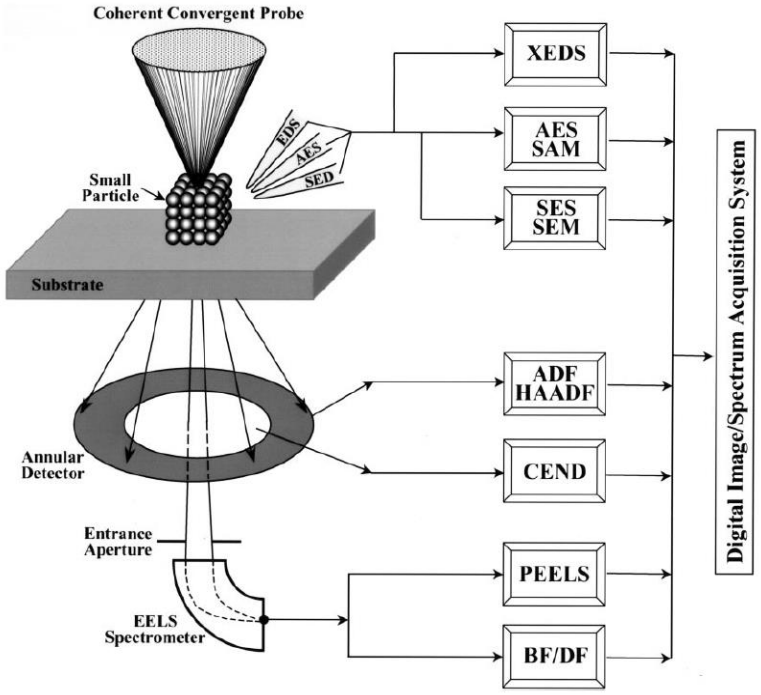

Figure 2.12. Schematic diagram of potential uses of STEM apparatus, showing annular and bright field imaging as well as backscattering techniques. Reproduced from [76].

output profiles. Because of this atomic size dependence, small atoms such as oxygen are not as easily visible in these images and make it less useful in oxide materials. ABF spatial images make up for this with a low-scattering dependence that allows for imaging of small elements, but this is at the cost of intensity scaling that makes images less contrasted. One of STEM's main benefits in modern setups is easy and sometimes simultaneous collection of certain imaging techniques in the same area, allowing for imaging of both HAADF and ABF images in tandem and getting the best of both techniques. EELS spectroscopy cannot be taken simultaneously with ABF imagining as they both use the same emitted electrons that have passed through a magnetic lens, but this technique allows for point-by-point spectroscopic data of a given sample. This allows us to determine not only the specific element at a given position based on its emission profile, but also analyze the spectra for valence change or electronic structure in a sample. Each

will be described in greater detail after an introduction to the theory of operation and experimental apparatus is provided.

Morton and Ramberg first proposed and demonstrated such a technique in 1939, where a non-corrected electron beam provided a projection microscopic shadow image of the material [78]. This and all transmission electron microscope techniques operate under simple scattering dynamics, where the amplitude of the transmitted scattered electrons can be described by the wave function **Ψ**(**K**,**X**). Vector **X** is the position of the incident beam and **K** is the typical 2D reciprocal space wavevector with magnitude

$$|\boldsymbol{K}| = \frac{2sin(\frac{\Theta}{2})}{\boldsymbol{\lambda}} \qquad \text{Equation 2.4}$$

Where λ is the wavelength of the electron beam and Θ is the scattering angle, similar to the wavevector seen for RHEED analysis. We know that direct observation of the wave function is impossible, but we can instead measure the intensity wavefunction of the transmitted electrons **I**(**K**,**X**) = $\left|\boldsymbol{\Psi}(\mathbf{K},\mathbf{X})\right|^2$. This intensity for a given beam position **X** can be described as [79]

$$\mathbf{I}\,(\mathbf{X}) = \int D(\mathbf{K})\,|\psi\,(\boldsymbol{K},\boldsymbol{X})|^2\ \mathrm{d}\mathbf{K} \qquad \text{Equation 2.5}$$

D(**K**) is the transmission function of the detector, and is usually described by a gamma function δ(**K**-**G**) where **G** is the reciprocal lattice vector. If this is the case, the intensity function reduces to I(**X**) = $|\psi\,(\boldsymbol{G},\boldsymbol{X})|^2$. This intensity can be observed at the diffraction discs formed by the convergent electron beam with divergence angle α. This same conical angle also extends to the formed diffraction disks, and if this angle is smaller than the Bragg diffraction angle, the disks overlap as shown in Figure 2.13. The electron detectors can then be placed at the

intersection of these discs to obtain intensity fringes as the electron probe is scanned across the sample.

The intensity distribution of the coherent electron probe can be described by

$$P(\mathbf{R}) = \int T(\mathbf{K}) \exp(-i2\pi\, \mathbf{K} \cdot \mathbf{R})\, d\mathbf{K} \qquad \text{Equation 2.6}$$

Where T(**K**) is the transmission function of the microscope (not same as detector transmission function D(**K**)) and **R** is the distance between the electron source and detector. The transmission function describes how much of the electron source reaches a detector, and can be given by

$$T(\mathbf{K}) = A(\mathbf{K}) \exp(-i\chi(\mathbf{K})) \qquad \text{Equation 2.7}$$

Where A(**K**) is the aperture delta function that is either open (1) or closed (0) if K is more or less than the cutoff wavevector $\mathbf{K}_0$ determined by the aperture size. The aberration function

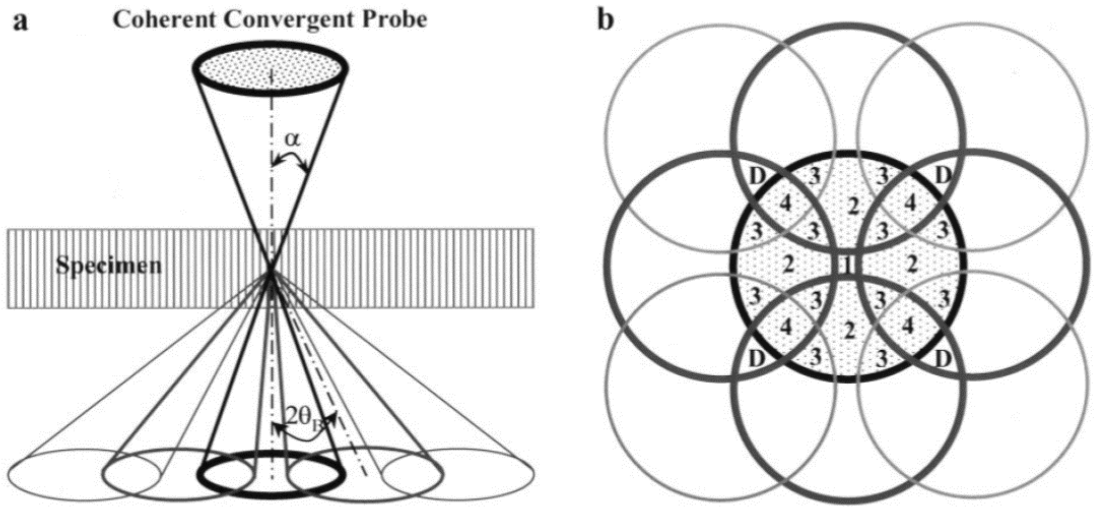

Figure 2.13. Bragg diffraction circles produced by atomic scale electron beam. Interference patterns from overlapping of secondary cones with primary produce diffraction patterns that can be analyzed. Primary cone makes up ABF imaged area, interference outside this area (D) makes basis for ADF and HAADF imaging. Reproduced from [76].

$\chi(\mathbf{K})$ is a function of the defocus value of the electron beam and the spherical aberration coefficient. If T(**K**) can be solved with known quantities from the microscope, then the first-order approximation the wavefunction **Ψ** of the transmitted electrons can be determined and in turn describe the intensity fringes observed for a lattice vector. T(**K**) is related to the first-order approximation of **Ψ** by

$$\boldsymbol{\Psi}(\mathbf{K},\mathbf{X}) = Q(\mathbf{K}) * T(\mathbf{K}) \exp[-i2\pi\mathbf{K}\cdot\mathbf{X}] \qquad \text{Equation 2.8}$$

Where Q(**K**) is the Fourier transform of the transmission function of the sample q(**X**). The real space transmission function depends on the interaction constant, accelerating beam voltage, and the projected sample potential. Each of these are knowable quantities. This shows that we can go from a coherent electron probe beam to an intensity profile of the transmitted electrons that describes the atomic lattice that diffracted it.

Accomplishing this theoretical framework with atomic resolution requires complex setup with several advanced electron optics, multiaxis detectors, and UHV equipment. Aberration correction (to at least the third order term) has allowed STEM systems to achieve the sub-Å resolution necessary to image atoms. This is accomplished with multiple series of optics and apertures before encountering the film. Optics introduced after the transmission through the sample serve to focus the beam at detectors and do not significantly impact the image obtained. Small electron point sources attempt to limit the initial spread of the electron beam, but usually come from tipped sources that will increase spread as the current is brought into the mA range. This then requires a system of magnetic condenser “lenses” that focus the electron beam, as shown in Figure 2.14 [80, 81]. This condensing happens multiple times to help correct for the chromatic and spherical aberrations inherent in the rotationally symmetric lenses. This is needed based on Scherzer theorem that states that charged particles passing through a rotationally

symmetric field will encounter a higher index of refraction and focusing near the lens edges than at the center of the beam, making for larger degrees of aberration [82]. The multiple lens system then ensures that each part of the electron beam has the same degree of aberration. These

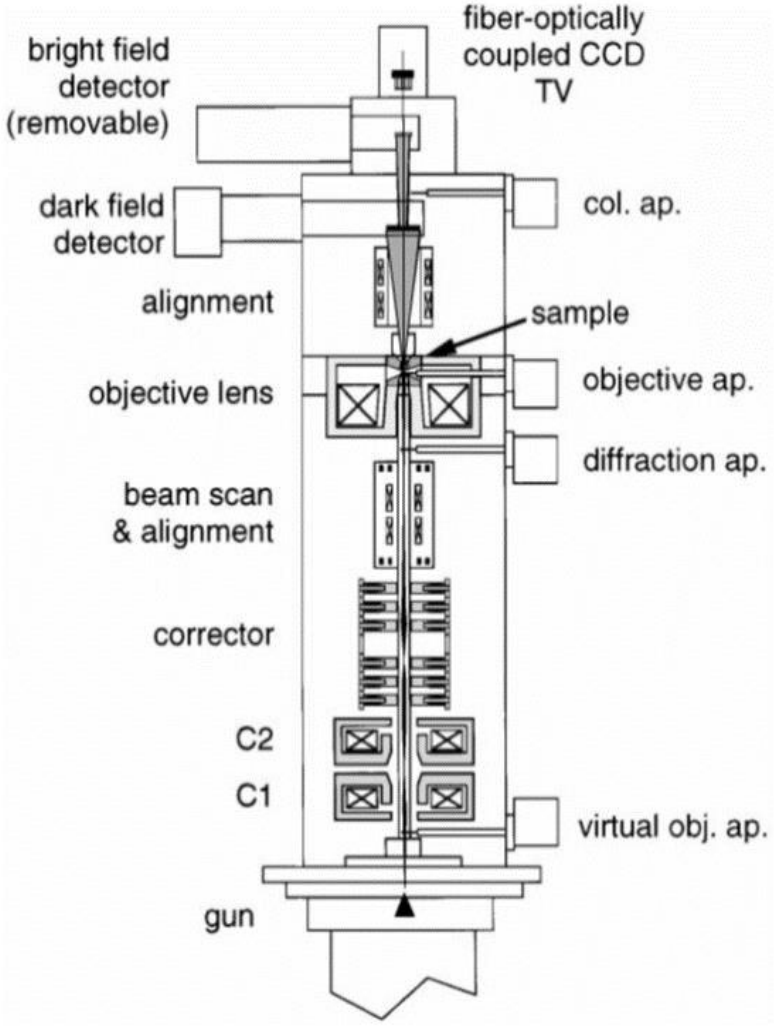

Figure 2.14. Schematic of STEM optics, scanning system, and detectors. Condenser and diffraction lenses create atomic-scale electron point beam, while corrector provides Cs aberration correction. Scanning coils magnetically position beam on sample through aperture. Detectors placed at bright field and dark field positions. Reproduced from [77]

aberrations, called Cs aberrations, can then be mitigated with the addition of quadrupole-octupole aberration correctors at this stage of the system [80]. It is has even been suggested that

with sufficient aberration correction that 3D resolved images can be constructed from a single 2D cut of a material [83]. These condenser lenses then focus the beam through a series of scan coils that are able to direct the angle of the beam through the rest of the system and provide the scanning functionality. An objective aperture after the scanning coils puts a hard limit on the amount of spreading possible before encountering the final focusing objective lens. This lens is responsible for focusing the beam down to an atomic scale which allows for the sub-Å resolution (the utilized JEOL ARM system has a spatial resolution of .071nm).

After the beam interacts with the material and the diffracted electron beam intensity carries with it the lattice information, it must be directed into the desired detector. The detectors used for these systems need a high resolution and high refresh rate in order to scan large areas of a material, and modern systems make use of direct electron detectors. These come in multiple forms, but for the JEOL ARM system utilized for this work, a scintillation detector is used. This is a converted CCD design that has excellent refresh rate and allows for fast capture of large areas, but is also a design with a lower contrast ratio due to a shallow well depth [84]. The pnCCD used is a Si-based charge converter detector with a high radiation hardness (good for large beam currents that increase signal-to-noise) [85]. Charged particles hit the semiconducting material and create electron-hole pairs that can be spacially- and temporally-resolved by accurate timing of their reception by the electrical circuit in order to create an image. This technique has the downside of potential lateral displacement (and subsequent resolution loss) of the electron-hole pair but can be mitigated by limiting the size of the scintillation area. This entire system from electron optics through signal detection is operated under UHV in order to limit electron scattering and not contaminate surfaces of cleaved samples. The detector can be utilized in a "4D" configuration, where 2D reciprocal space diffraction patterns are recorded for each 2D real

space cross-sectional area, leading to the term 4D STEM. Strain mapping can make use of this 4D STEM system by looking at the diffraction pattern observed at each point and determining how much the pattern is stretched or compressed relative to a baseline [86, 87]. By utilizing these techniques we are able to obtain atomic-resolution structural information from HAADF, ABF, and EELS, as well as strain mapping and Fast-Fourier transforms (FFT) of the imaged areas.

HAADF imaging looks at the incoherent elastic electrons scattered at high angles outside the innermost Bragg disk. The impact parameter of the beam is small (highly focused near atomic sites) and the scattering is therefore strongly nuclei dependent and unscreened by atomic electrons [88]. The low background of these high angle measurements make it ideal for FFT's of the diffraction pattern produced. After analysis, these FFT's take the form of arrays of diffraction spots, which through HAADF are dependent on the spacing between high-Z elements. The spacing between these spots, which are dependent on the induced lattice constants of a film, can be compared with expected patterns based on known bulk lattice parameters and a strain difference between the two can be calculated. This can be done to calculate in-plane (ε_{xx} component of the strain matrix), out-of-plane (ε_{yy}) and sheer distortions (ε_{xy} and ε_{yx}) with the same atomic resolution as HAADF and can be used to determine any local distortions of the lattice strain [89, 90]. It is also possible to use FFT's with ABF images in order to determine any rotational symmetry changes. These ABF images use the direct beam coherent elastic scattered electrons, which means they do not need the large scattering cross-section to be reflected at the high angles needed in HAADF. This lower dependence on Z allows for imaging of light elements, which is of particular importance in oxide research. The oxygen octahedra can be directly imaged, and any distortion of bond length or plane alignment (tilt) can be directly imaged. Applying an FFT to these patterns also allows us to determine the rotational symmetry

of a layer for a given imaging direction, often described in pseudo-cubic notation in thin films for clarity. Comparing the ABF FFT's with Glazer simulations allows us to determine if the rotational symmetry of a bulk material is maintained in the films. Precise measurement of the structural changes induced through thin film growth is pivotal in understanding many interesting property changes linked to thin film structural deformation[91–93].

Both HAADF and ABF imaging utilize elastically scattered electrons that only interact with atomic nuclei and maintain their energy as a result. If the electron beam does interact with the atomic electrons however, energy can be lost and inelastic scattering occurs. The lost energy is absorbed by atomic core electrons that can become excited above the Fermi level and is characteristic of the local orbital environment [94]. The electron beam comes through the material having lost this characteristic energy, giving chemical information such as the element encountered and its valence state, as well as giving lattice information such as plasmon formation or phonon excitations. Emitted electrons are passed through a magnetic prism (finely controlled magnetic field region) that separates them based on their energy, which can then be captured by a CCD or similar detector. Further refinement of the energy resolution of the spectra can be obtained by introducing a magnetic monochromator pre-sample to ensure only one electron energy enters a specimen. Monochromators can be used to achieve sub-200meV resolution of the final EELS profile [95]. Coupled with the Cs aberration corrected lensing systems used for STEM, this allows for atomic resolution of EELS profiles. For the rare earth elements and first line transtition metals, the characteristic EELS spectra have a two-pronged line shape typically referred to as $L_{2,3}$ peaks. These peaks, sometimes called "white lines", are due to the dipole nature of the p-orbital and correspond to $2p_{1/2}$ (L_2) and $2p_{3/2}$ (L_3) excitations into the d-shell[96]. Only the first row of transition metals show this overlapping fine-structure because

lower row metals have higher spin-orbit energy splitting that decouples the peaks. Change in the separation of $L_{2,3}$ can give vital information about the valence state of an element, which is of particular interest in thin film oxides whose valence state can be greatly affected by oxygen content or charge transfer [97, 98]. We will use this technique to look both for elemental intermixture at thin film heterointerfaces and for analysis of the line spectra formed for the elements to look for evidence of valence change.

2.3. Physical Property Measurements

While it is important to ensure the films grown are stoichiometric and crystallographic, much of the physics of interest for this study lies in the physical characteristics exhibited by those films. There are many techniques that can probe these features, but this study will rely primarily on magnetic measurements through a Superconducting Quantum Interference Device

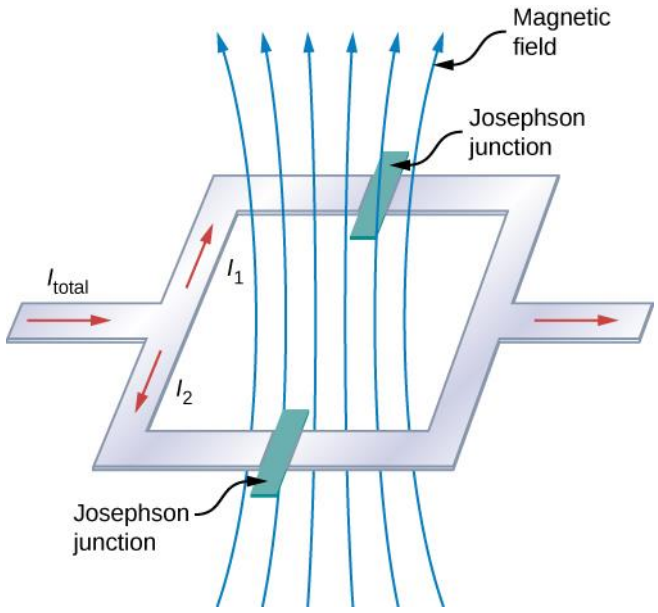

Figure 2.15. Schematic of SQUID measurement coil. Current is passed through the loop from one end and split evenly across the opposite branches. Changes in the magnetic flux through the loop affect the direction of current flow in the loop and therefore change the voltage across the Josephson junctions which can be measured and quantified. Reproduced from [86].

(SQUID) and resistivity and magnetoresistance measurements through a Physical Property Measurement System (PPMS)

As the name implies, SQUID devices are only made possible by the superconducting loops and Josephson junctions inside the machines. They work in two primary modes, either DC or RF (radio frequency), but the machine used in this study utilizes the DC mode and will therefore be the focus of this section. For these measurements, an input current I_i is sent through a type-1 superconducting coil split into two different branches, as shown in Figure 2.15 [99].

If no magnetic flux flows through the center, the current will be split evenly across the branches. If, however, magnetic flux does penetrate the coil, a current I_s will flow in order to keep the internal field zero. This has the effect of creating a larger current in one branch of the coil and a smaller in the other as I_s moves in the same direction as one and opposite the other. If the resultant current is larger than the critical current of the Josephson junction, then the supercurrent will be able to tunnel through the insulating barrier and create a measurable voltage difference in the barrier. It is not however the absolute value of this voltage that determines the flux penetrating the loop, but rather its oscillation. This is due to the nature of the superconducting loop only being able to allow integer values of the magnetic flux quantum through the coil

$$\Phi_{loop} = n * \Phi_0 = n * 2.068e(-15)\ (T * m^2) \qquad \text{Equation 2.9}$$

This reality, that only certain values of magnetic flux are allowed through a superconducting loop, reveals deep physics about the nature of superconductivity. A fundamental part of BCS theory is that the wavefunctions of the superconducting Cooper pairs of a system must have long range coherence and occupy the same quantum state. This means that for any electron making a

loop around the coil, its wavefunction must always change phase by 2π. If a magnetic flux is induced through the superconducting loop, this phase change must still be maintained, and arbitrary values of magnetic field will not always produce the required phase change. It is only integer values of the magnetic flux quantum that allow for this quantum mechanical necessity, and thus these are the only allowable values for the intervening flux. As a side note, this is also a way to describe the nature of zero resistivity in superconducting loops, as even if the magnetic flux through the loop decreases to zero, the current cannot slowly decay to zero but must jump from its non-zero value to zero to avoid any disallowed flux values. As this decay is statistically impossible for a quantum state of the number of electrons in the supercurrent, the current will not decay and will continue to run indefinitely with not external application of voltage.

As a result of only certain allowable flux quanta, the current through the superconducting loop will move in such a way as to create discreet values of Φ_0. Practically, this means that as the applied field creating the flux increases from zero to $\Phi_0/2$, current will flow in order to counter this change as would be expected in normal Faraday's law considerations and force a net flux of zero. However, as the field becomes higher than $\Phi_0/2$, the superconducting loop now has an energetic incentive to increase the flux through the loop to Φ_0 as opposed to bringing it down to zero, and as a result the current will flip directions and start creating more flux through the loop. The screening current maintains this direction until the applied field reaches Φ_0, from whence the cycle repeats as long as the applied field continues to increase. This switching creates a measureable change in the voltage reading in the Josephson junctions, and the number of oscillations that occur are locked into the exact number of flux quanta that have gone through the loop. It is ultimately these voltage oscillations that are measured by the SQUID device and converted into the measured signal from any samples placed in the machine. The

lowest measurable signal is only limited by the magnetic flux quanta and can be as low as 1E-14 T, which our machine achieves.

SQUID machines must be able to bring the materials for measurement down to very cold temperatures and apply high fields across them in order to probe the various magnetic characteristics that can emerge under different conditions. Our machine is capable of cooling samples down as low as 1.7K up to 400K and applying external fields up to ±5 T. How these temperatures and fields are created will be addressed in section 2.3.2. These machines can look for a wide array of magnetic phenomena by looking for both magnetic hysteresis in MH curves or by looking for changes in behavior of the MT data.

PPMS devices have simple measurement schemes, but require advanced equipment in order to control the environments in which the measurements take place. At its core, PPMS measures the voltage difference between contacts attached to the desired sample. These contacts are attached either with lithography techniques or with simple application of metal ohmic contacts. This simple idea in the correct and controlled environment can give information on not only the resistivity of a material, but also its hall characteristics, magnetoresistivity, magnetic susceptibility, and other physical parameters, and the temperature and external field dependence of each of these properties.

Without precise control of the temperature within the sample chamber, many small differences in temperature dependent phenomena would be washed out or mischaracterized. Moreover, the ability to reach extremely low temperatures, even below the boiling point of the liquid helium used to cool the sample chamber and electromagnet, is necessary for many materials that have resistive or magnetic behavior changes at these ultra-low temperatures. In order to achieve this, there are two primary methods, pot fill and continuous low-temperature

control (CLTC) [100]. These modes take over below the helium liquid temperature of 4.2K. Both of these methods use pressure control of the helium in order to push the sample chamber temperature down, though pot-fill makes use of the pressure of liquid helium and CLTC of its gaseous form. CLTC is used primarily in these studies as it is the faster of the two options and

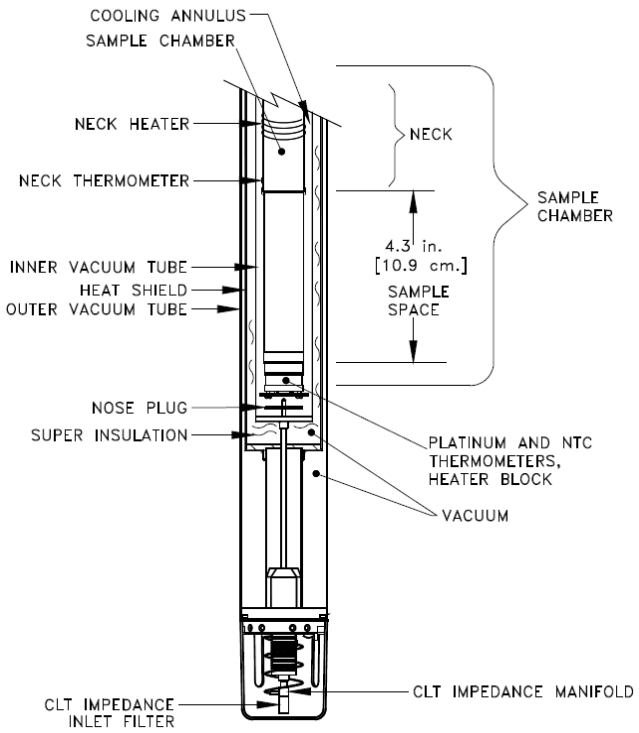

Figure 2.16. Schematic of PPMS sample chamber with thermal control elements highlighted. The entire sample space is thermally sealed from the exterior with multiple layers of vacuum tubes and "super" insulation. The nose plug allows for the CLTC control of the low temperature regime. Reproduced from [20].

can maintain the temperature of the sample at these low temperatures indefinitely, which is necessary for Hall measurements that may take hours, while pot-fill can only maintain the temperature for shorter periods up to 90 minutes. To maintain these ultralow temperatures, gas is fed through a special impedance tube as opposed to the normal impedance which is responsible for creating a slight helium pressure inside the sample chamber while above this temperature

regime. This CLTC impedance tube pressurizes with helium gas, and then allows some gas to escape, thus lowering the temperature of the gas inside the tube. This lower temperature gas is then allowed into the sample space where it directly cools the sample. Special care must be taken in this mode to not condense the helium gas back into its liquid phase while inside the sample chamber, and to mitigate these concerns the CLTC mode will go through a slow cooling process to reach the desired temperature.

Applying a high magnetic field across the materials inside PPMS and SQUID apparatuses is of utmost importance and must be highly controllable and capable of sustaining high fields during long measurements. To accomplish this, superconducting magnetic coils are used. In order to produce the large fields necessary, currents in the coils must also be incredibly large, with the actual current necessary being dependent on the material used for the coils. Ordinary metals could not withstand the currents used to create the high fields for these experiments, as the resistance in those coils would heat them to dangerous levels. That is why careful

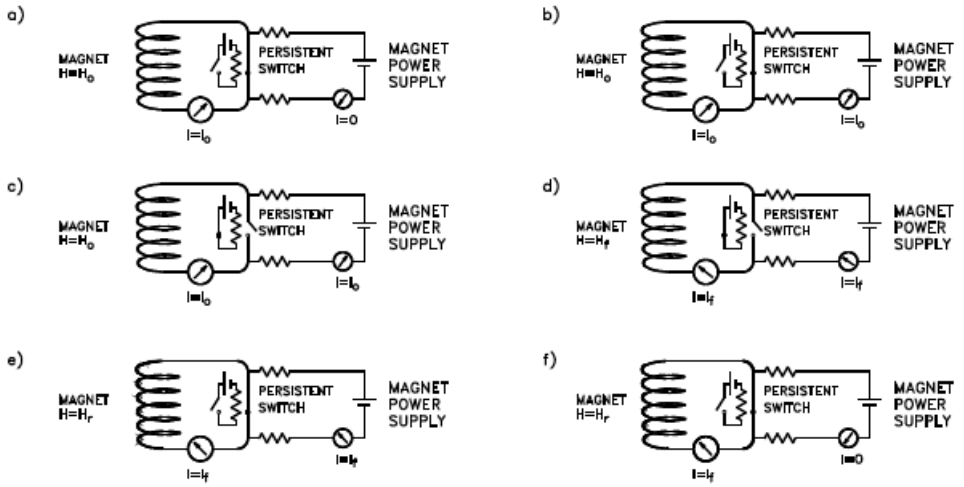

Figure 2.17. Step-by-step layout of persistent field mode in superconducting magnetic coil setups. The persistent switch has an external heating resistive circuit wrapped around it in order to increase its temperature locally and create the switching effect. Reproduced from [20].

consideration is placed on keeping the superconducting coils at low temperature at all times by the helium bath, as the currents in the electromagnets could quickly overheat the coils, causing damage to the wires themselves and possibly creating explosive expansion in the surrounding helium bath. Despite this fact, strategic use of superconducting to non-superconducting phases in the coil allow for easy switching of the magnetic field production from the coils. A schematic outline of the procedure is shown in Fig 2.13.

To change the field inside the coil while maintaining the superconducting current already within the wires, first an external superconducting wire attached to a current controller is brought to the current operating amperage of the magnetic coil. When this current is achieved, a heater in the circuit of the magnetic coil begins to heat a persistence switch. This switch is heated above the T_c of the material in use and becomes resistive. As a result, current from the coil prefers to travel through the still superconducting external wire. The current is then increased to achieve the desired field in the coil, at which time the persistence switch is usually allowed to cool back into its superconducting state, trapping the supercurrent in the coil to create a persistent and well-defined magnetic field. If speed is desired for a particular measurement cycle, the switch can be

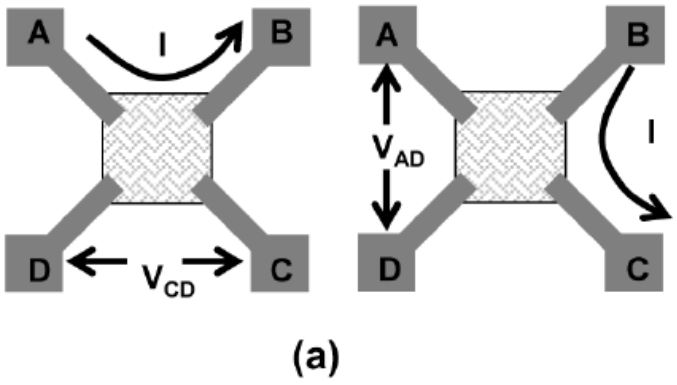

Figure 2.18. Schematic of possible Van der Pauw setup of contacts on sample. Two measurements must be taken at every applied field in order to get Hall data, both V_{cd} and V_{ad} with the correct current applications. Reproduced from [21].

kept open so that the current in the coil can be more quickly changed, called the “driven” mode, but this option does not produce as precise a field as the normal “persistent” mode and is not advisable for materials with fine details in the magnetic behavior.

PPMS techniques involve setting up, ideally ohmic, contacts on the surfaces of the materials of interest, and the particular positioning of the contacts allows different measurements to be taken. Contacts with the material should be metallic and contribute as little as possible resistance and noise to measurements, which is to say they are ohmic and obey simple V=IR considerations. To achieve these good contacts, highly conductive metals such as silver, indium, or gold should be used. These materials need to penetrate the top few unit cells of the material and bond to the crystal structure in order to create a low resistance Schottky barrier. This can be achieved either through direct depositions of the materials or through lithography techniques. Lithography is especially useful when attempting to create precise alignments of contacts which limits the amount of background subtraction necessary during data analysis and can make small features such as topological hall effects or small anomalous hall effects readily apparent during measurement. If Hall measurements are desired, the probes can be set up either on a lithography fabricated Hall bar or in a square 4-probe Van der Pauw arrangement. Hall bars are useful in that they can help inherently filter out longitudinal components of the resistivity measured in the sample, which makes for speedier data analysis and can help highlight small magnetic features. A square Van der Pauw approach allows for simultaneous measurement of sheet resistivity as well as Hall features, but does allow for a large component of longitudinal resistance in the Hall measurements if the leads are not precisely positioned on the sample, and can lead to false negatives in samples with small signals and less than ideal background conditions [101].

Chapter 3. Interface Induced Magnetic Revival in Ultrathin Manganite-Ruthenate Trilayers

In the following chapter, we will investigate ferromagnetic-phase LCMO trilayers with three different buffer layers, SRO, CRO, and STO. This will be done after first confirming the behavior of LCMO monolithic films in order to properly compare any behavior seen in the heterostructures. The three buffer materials will then allow us to investigate the role of not only structural change in LCMO but also the role of the Ru-Mn interfacial bond, incipient ferromagnetism, and charge doping on the properties of LCMO. This chapter in particular makes use of ultrathin heterostructures of the form $LCMO^{4uc}/Buffer^{3uc}/LCMO^{4uc}$, where each layer is sub-critical thickness and therefore isolates the effects originating from the heterointerfaces. We find that only trilayers between LCMO and SRO have an enhanced magnetic signal in the $LCMO^{4uc}/Buffer^{3uc}/LCMO^{4uc}$ ultrathin regime. Moreover, these magnetic heterostructures are also fully insulating at all temperatures, meaning that the magnetism observed is not long-range DE mediated but rather has moved to a separate magnetic characteristic from the bulk material. Based on previous knowledge of DE mechanisms in LCMO and Stoner ferromagnetism in SRO thin films, we discuss many potential sources of this magnetism, and posit that above-T_c disordered magnetic moments in SRO, interfacial exchange coupling, and a buffer layer mediated reduction in crystal symmetry may be the most likely causes of this enhanced effect.

3.1. Growth

We have utilized PLD growth in UHV using sintered stochiometric SRO, CRO, STO, and LCMO targets. Each material has its own growth conditions that optimize their growth mode (layer-by-layer or step-flow are both acceptable) and adherence to the substrate lattice parameter. Table 1 outlines the optimized growth conditions for each material on STO (001) single crystal substrates used in this study.

Table 3.1. Growth conditions used in PLD growth of thin films				
Material	Laser Energy/Pulse (mJ), Energy Density (J/cm^2)	Repetition Rate (HZ)	Temperature (°C)	Oxygen Pressure (mtorr)
LCMO	21, 1.40	10	700	100
SRO	52.5, 3.5	10	700	100
CRO	21, 1.40	10	700	150
STO	19, 1.26	5	700	10

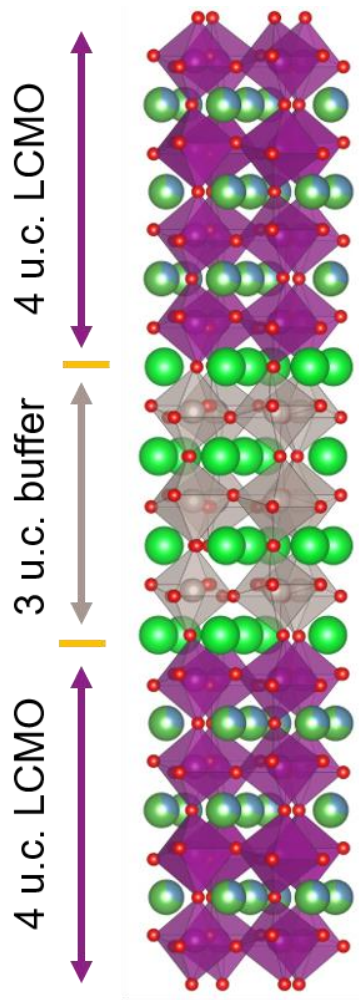

Figure 3.1. Schematic of trilayer films grown on STO(001) substrates. Yellow lines indicate interfaces between film layers.

All energies listed in Table 1 come from an external energy meter from ThorLabs specifically used to measure the power at λ = 248 nm. The energy density is calculated by

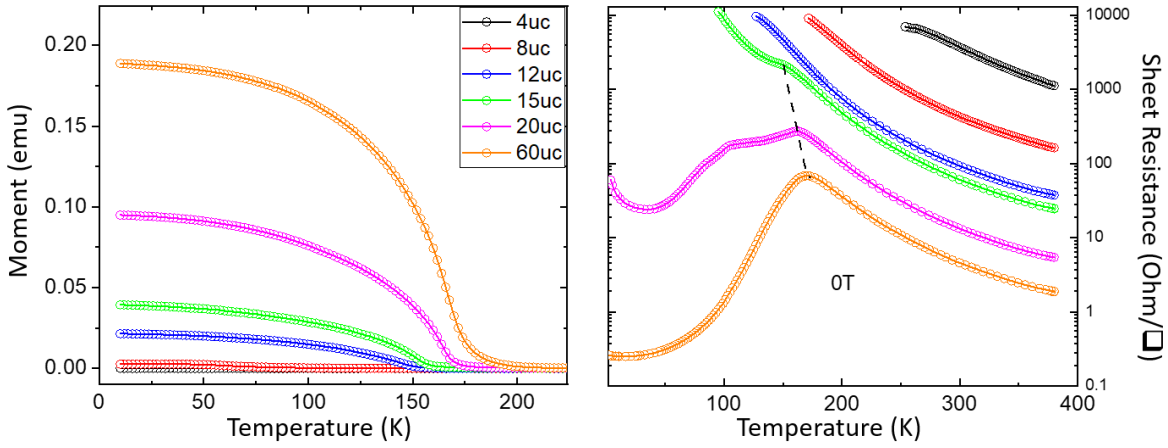

Figure 3.2. Magnetic and Resistive measurements for monolithic LCMO films on STO(001) substrates. Becomes metallic below 20 u.c., with black dotted line indicating Tc from M(T) data.

measuring the size of the laser spot at the target material, which in our system is 3.0 x 0.5 mm.

Using these conditions, we have grown a series of monolithic LCMO films as well as buffered

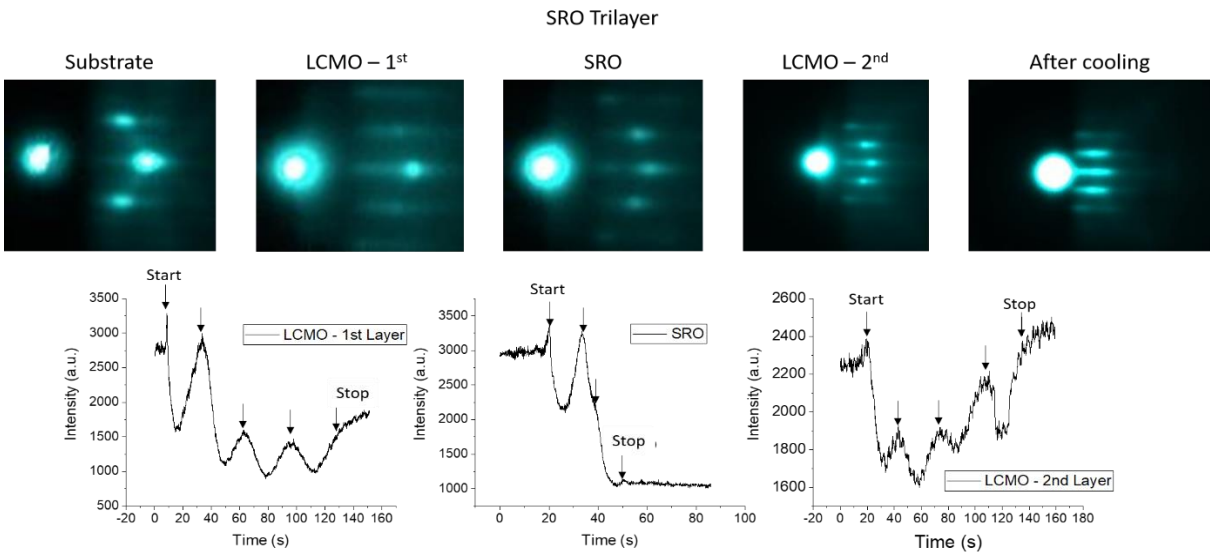

Figure 3.3. RHEED data from growth of $LCMO^{4uc}/Buffer^{3uc}/LCMO^{4uc}$ trilayer. Each layer shows osscialtions, though LCMO is clearer than SRO. RHEED spots show quality step flow growth. SRO appears to have surface termination conversion with longer first oscillation.

LCMO trilayers following the form $STO(001)_{substrate}/LCMO^{4uc}/Buffer^{3uc}/LCMO^{4uc}$. A schematic of this system is provided in Figure 3.1.

To understand the divergence of the trilayers from what is seen in typical LCMO thin films, we grew a series of monolithic LCMO films on STO substrates. This work has been done in the past, but was necessary to ensure that our LCMO was grown with optimal doping and crystallinity and in agreement with previous studied. We grew thicknesses both above and below the known critical LCMO dead-layer thickness of 12 unit cells and looked at their magnetic and resistive properties. This property audit is summarized in Figure 3.2, showing that our films show the characteristic thickness dependent transition around 15 unit cells from a material with a MIT to a fully insulating film. This is also reflected in the M(T) data, where thicker films exhibit a clear magnetic onset around the same temperature as their MIT, but thinner films have their onset temperature reduced until it is nonexistent for films less than 4 unit cells. This confirms that our films follow the same thickness driven transition previously observed which can then be compared with our trilayer heterostructures [49, 102].

Determining the thickness of these films and preliminary quality determination is done through monitoring the diffraction spots produced through RHEED. Figure 3.3 shows the RHEED growth of the $LCMO^{4uc}/SRO^{3uc}/LCMO^{4uc}$ buffered film. We can see that the films show excellent oscillations even after the deposition of layers of different materials, and also show minimal signs of formation of any islands or other artifacts. The growth does appear to enter a step-flow mode as opposed to a layer-by-layer, as evidenced by the emergence of streaky patterns around the primary diffraction spots. As noted in Chapter 2, this does not however denote a poor quality film crystallinity but rather a nucleation transition to step edges. We note that growth of multiple disparate layers tends to roughen any surfaces compared to a clean substrate single crystal surface,

but the fact that oscillations are still present in the upper layer of LCMO growth shows that the films are of good quality. We also note that the first oscillation in the SRO layer growth shows a longer oscillation time than for the next two unit cells. This is a known feature of SRO film growth and is attributed to termination conversion in the first SRO unit cell[103]. Because the RuO_2 surface is volatile, a smooth surface is not formed until the more stable SrO layer is grown on top, meaning that the first oscillation corresponds to a 1.5 unit cell growth, which is reflected in a longer first unit cell growth time by the same factor. This may however change during subsequent layer growth and termination conversion will be analyzed through EELS mapping.

3.2. Structural Analysis

While RHEED is a useful technique for real-time monitoring of crystal quality and layer formation, it is unable to determine if the film has epitaxially adhered to a substrate or give a holistic picture of a film's quality. Thin film XRD can provide further evidence of film quality to ensure that our films are well controlled both in terms of layer thickness and overall crystallinity. We therefore grew a superlattice of $[LCMO^{4uc}/SRO^{3uc}]_{12}$, where each bilayer was repeated 12 times. This was

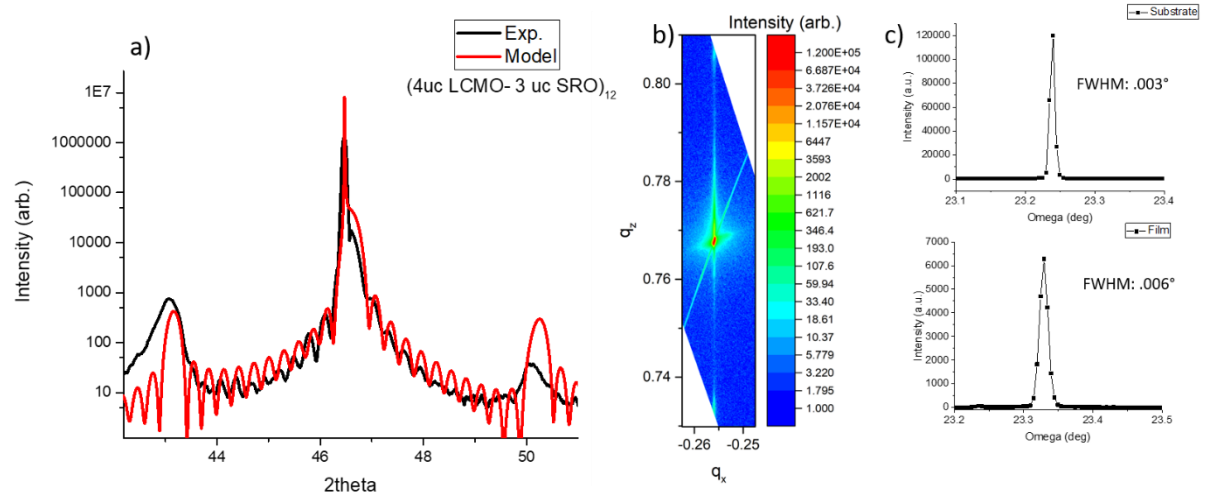

Figure 3.4. XRD Data for $[LCMO^{4uc}/SRO^{3uc}]_{12}$ heterostructure. a) Experimental (black) and simulated (red) coupled scan around (002) with arbitrary units of intensity. b) RSM of (-103) asymmetric spot c) Rocking curves for substrate (top) and film (bottom).

done in order produce a larger signal from the acquisition and show that we had well controlled growth no matter how many interfaces were formed. The XRD data is shown in Figure 3.4. The coupled scan shows a large number of fringes which indicates a regular repetition of layer thicknesses that do not destructively interfere with one another. This data is juxatopsed with a simulation of an ideal 4-3 bilayer heterostructure, shown in red. The simulation was carried out using a MATLAB program developed for use with perovskite oxides that uses a modified kinematic approach with an attenuation factor [104]. This attenuation takes into account a degree of the scattering and absorption that occurs in XRD experiments, but falls short of a full dynamical theory calculation due to computational limits. Good agreement between the data and simulation show that we have consistent control over the number of unit cells grown in each layer which is pivotal in extremely thin film studies. The main film peak occurs near the STO substrate peak, which is indicative of the fact the average OOP lattice constant of the film is slightly higher than that of STO due to the tensile strain in the majority LCMO layers. The rocking curves also show that our films match the mosaic spread of the substrates and do not form multiple growth directions. Epitaxial strain is confirmed by RSM around the (-103) asymmetric spot, where the film peak shows minimal spread in the Q_x direction, meaning that the IP lattice constants of the STO substrate and heterostructured film are fully matched. The Q_z direction confirms the coupled scan behavior of a slightly higher average OOP lattice constant of the film compared to the substrate.

CRO and STO buffered trilayers were also grown using the parameters described in Table 4.1. The RHEED data is shown in Figure 3.5 for each. We note that the CRO layer data in 3.5a) displays a similar oscillation pattern to that observed in the SRO trilayer (Figure 3.3). Though

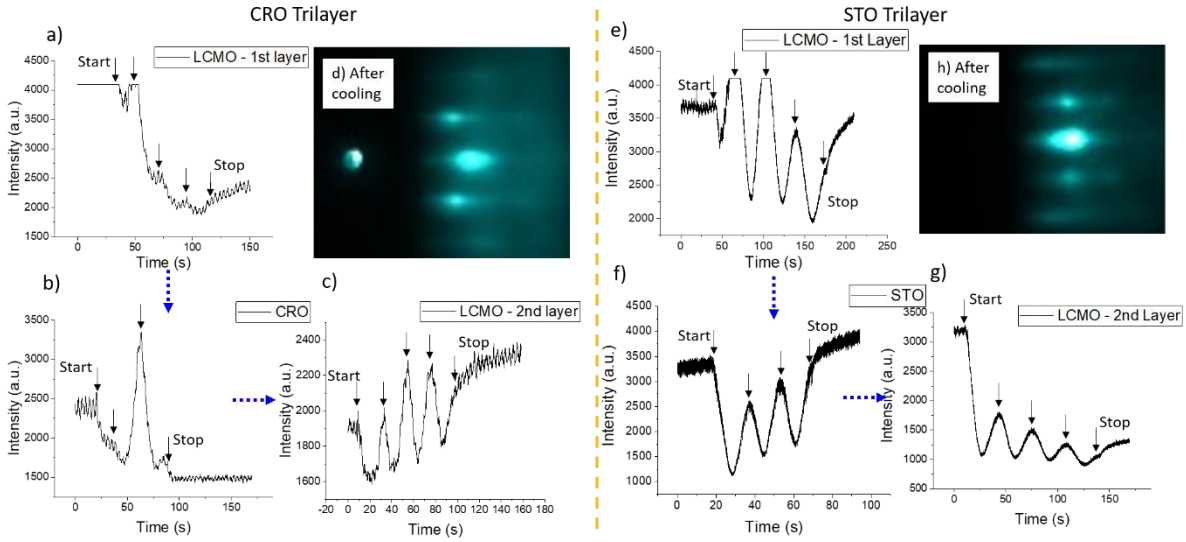

Figure 3.5. RHEED data for CRO and STO buffered ultrathin heterostructures. a) First LCMO layer followed by b) buffered CRO layer and c) 2nd (top) LCMO layer. Blue arrows indicate ordering of layers. e) First LCMO layer followed by f) STO buffer layer and g)top LCMO layer. d), h) After cooling RHEED images are taken after CRO, STO buffered samples are cooled in oxygen (growth pressure).

neither sample displays completely symmetric oscillations, this type of growth is characteristic of ruthenates grown in our lab and others, and still produces the desired layer thicknesses in other thin film studies undertaken in our group. STEM analysis on these samples confirms their good layer thickness adherence and overall sample quality and will be discussed later. STO heterostructures grew well with oscillations across all layers and a layer-by-layer RHEED pattern after the growth, which is typical for STO films that do not introduce any further lattice strain to the system.

By utilizing STEM atomic resolution (sub-Å) images, we are able to determine the structural changes across an interface through HAADF images, symmetry changes using electron

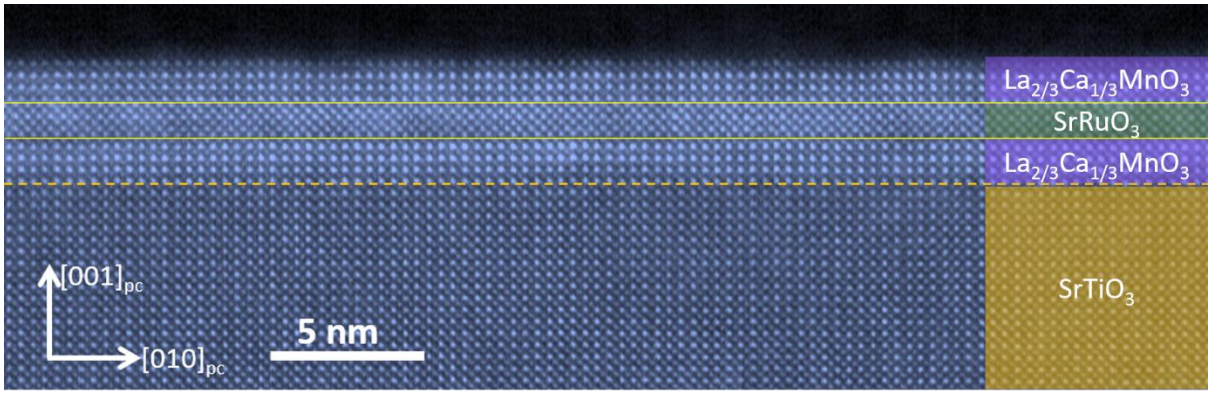

Figure 3.6. HAADF STEM image of ~60nm lateral area of $LCMO^{4uc}/SRO^{3uc}/LCMO^{4uc}$ trilayer. No dislocations are observed over this large area, and layer thicknesses are consistent throughout.

diffraction patterns, and any tilt and rotation modifications through ABF imaging. This full suite of structural data will allow us to contextualize any property modifications observed in the films. A HAADF image along the $[100]_{pseudo\text{-}cubic}$ direction of the $LCMO^{4uc}/SRO^{3uc}/LCMO^{4uc}$ trilayer is shown in Figure 3.6, and we can see that the film is well strained to the substrate with no dislocation centers over a 60nm imaged lateral area. The orange dashed line indicates the STO/LCMO substrate/film interface, while the yellow lines indicate the interfaces formed between the different materials of the trilayer. Each film layer is the desired thickness, showing that our determination of good sample control from RHEED and XRD holds. We also note that, in addition to being free from screw or edge dislocations, there is also only a single structural domain formed. SRO thin films have been known to form equivalent but rotated structural domains on STO substrates, and forthcoming work from our group indicated that these domains begin forming as soon as the first unit cell of SRO is deposited [105]. Likely this single domain structure is enforced by the

octahedral rotations of the base layer LCMO that preferentially align the SRO layers unlike on the purely cubic STO substrate.

By combining the HAADF and ABF images of the film, we can make detailed observations about the overall structural parameters of the buffered films. We do this in Figure 3.7, where we show HAADF and ABF images for two different beam directions, [100] and [110], as well as the derived IP (*a*/*b* pseudocubic lattice constant), OOP (*c* constant), and tilt angle for the oxygen octahedra. HAADF images are primarily used for the determination of the IP and OOP lattice constants while ABF imagining is necessary for tilt angle determination as it must be able to image oxygen atoms. Multiple directions are imaged to determine the tilt angle and look at the overall rotational symmetry for a given direction (discussed in Figure 3.8). The IP lattice constants in

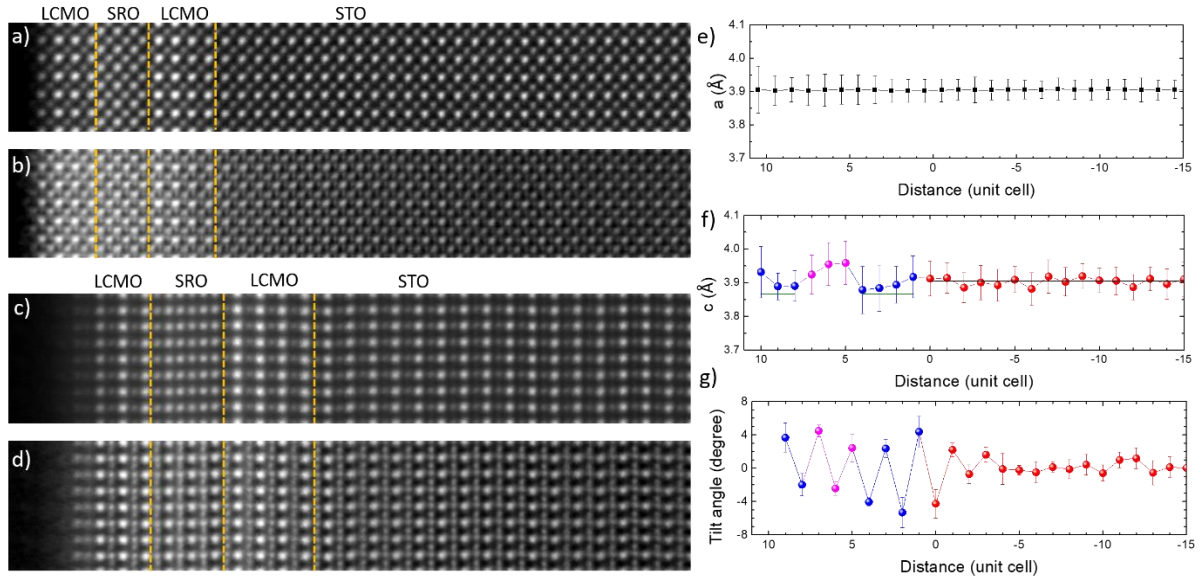

Figure 3.7. a-b) HAADF, ABF images in [100] direction for $LCMO^{4uc}/SRO^{3uc}/LCMO^{4uc}$ trilayer. Yellow lines denote interfaces. c-d) HAADF, ABF images in [110] direction for $LCMO^{4uc}/SRO^{3uc}/LCMO^{4uc}$ trilayer. e) IP lattice parameter for every layer in film, averaged across lateral area. Distance given in unit cells away from substrate interface, where 0 distance is the top STO layer, and positive distance goes into the film. f) OOP lattice parameter by film layer. Green line denotes LCMO bulk OOP pseudocubic lattice constant. g) Tilt angle as measured from ABF images.

Figure 3.7e) show that every layer of the trilayer film is epitaxially strained to the STO lattice constant, confirming our XRD results. In Figure 3.7 f) we see that the SRO layers expand their OOP lattice constant slightly beyond bulk values, as expected for compressively strained films, but LCMO layers also tend to show a slight c-axis increase despite being tensile strained. This effect is only moderate however, and weakens the further the film is from the STO substrate. The tilt angle from Figure 3.7g) shows that the film does still have a significant tilt in the ultrathin regime, with large tilt angles near the substrate interface that may be serving to dissipate some of the strain energy and help explain why less OOP lattice expansion occurs than would be expected. The net positive-to-negative tilt angle stabilizes around 7°, slightly less than the bulk 10° angle found in both bulk materials. This is expected for films in this ultrathin limit. It should be noted that for the calculated parameters, the top one or two unit cells of LCMO are not calculated, which is due to TEM sample preparation stripping some of the top layers and lowering the signal that can be obtained from these layers.

Diffraction patterns can also be obtained from the ABF diffracted beam through fast Fourier transform (FFT) signal processing. This technique is useful for qualitatively determining a sample's crystal symmetry, where the obtained FFT pattern can be compared with simulated

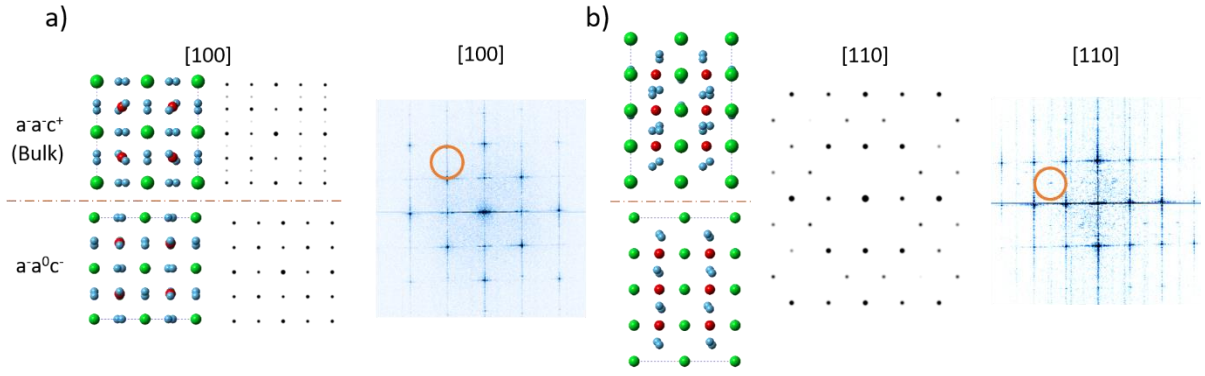

Figure 3.8. Simulated diffraction patterns for different tilt systems vs FFT data obtained from ABF imaging for a) [100] and b) [110] beam directions.

diffraction patterns for a given symmetry and scanning direction. For the FFT's obtained for the $[001]_{pc}$ and $[110]_{pc}$ cuts of the $LCMO^{4uc}/SRO^{3uc}/LCMO^{4uc}$ trilayer, shown in Figure 3.8, we can compare them to possible rotational models in those directions. Both SRO and LCMO follow an orthorhombic $a^-a^-c^+$ *Pbnm* symmetric pattern in bulk, but in thin films LCMO has been known to reduce its symmetry to a orthorhombic *Imma* pattern which has rotations in the IP direction but not the OOP direction following a $a^0b^-b^-$ Glazer tilt pattern[106]. Recent work from our group has shown that monolithic SRO will immediately regain a bulk-like *Pnma* structure within a single unit cell of growth on STO(001) . For the $[001]_{pc}$ direction, we can see from the simulation data that a system with $a^-a^-c^+$ rotation (*Pnma*) should have interstitial sites between main diffraction spots, whereas for a sample without rotation in that IP direction, no such intermediate spot would be observed. Our experimental FFT data shows no such intermediate spot for $[001]_{pc}$ direction, with no spot seen in the orange circle (added for emphasis), meaning that we have lost an IP axis of rotation. The crystal was also cut along a $[110]_{pc}$ direction, and we show the simulated pattern for the $a^-a^-c^+$ and $a^-a^0c^-$ (single IP tilt elimination, still orthorhombic) tilt patterns. Each of these patterns produce the same expected FFT's, and we see from the data that the expected intermediate spot exists (orange circle used to emphasize). This shows us that the other two rotations axes are preserved here, and the overall symmetry of the film is dominated by the thin film LCMO reduced tilt pattern and moves to an $a^-a^0c^-$ pattern, which is a rotation of the normal *Imma* $a^0b^-b^-$ LCMO structure. Moving to this rotated *Imma* structure with a single IP tilt axis may induce localization of mobile electrons and the overall resistive properties of the films [107, 108]. We make note here that these FFT's correspond to a single domain structure across the imaged areas, whereas some

studies of SRO thin films have shown that they can move into a two-domain structure in certain cases [109, 110].

We also obtained STEM data for the STO buffered sample in order to understand how a reduction in buffer layer tilt pattern might affect the LCMO layers, giving us a good structural comparison for forthcoming magnetic data. Figure 3.9 shows the HAADF, ABF, lattice constants, and tilt angle for the $LCMO^{4uc}/STO^{3uc}/LCMO^{4uc}$ heterostructure. HAADF images in a) and c) show that our films are the desired thickness with good crystal uniformity. This is born out in panels e-f), where the IP lattice constants are strained to the substrate while the OOP lattice constants for the LCMO layers does decrease below its bulk (green line) value as expected for a tensile strained film. This is different from the SRO buffered trilayer where the LCMO layers had a larger than bulk c-axis. This is perhaps related to the reduction in tilt angle for this sample

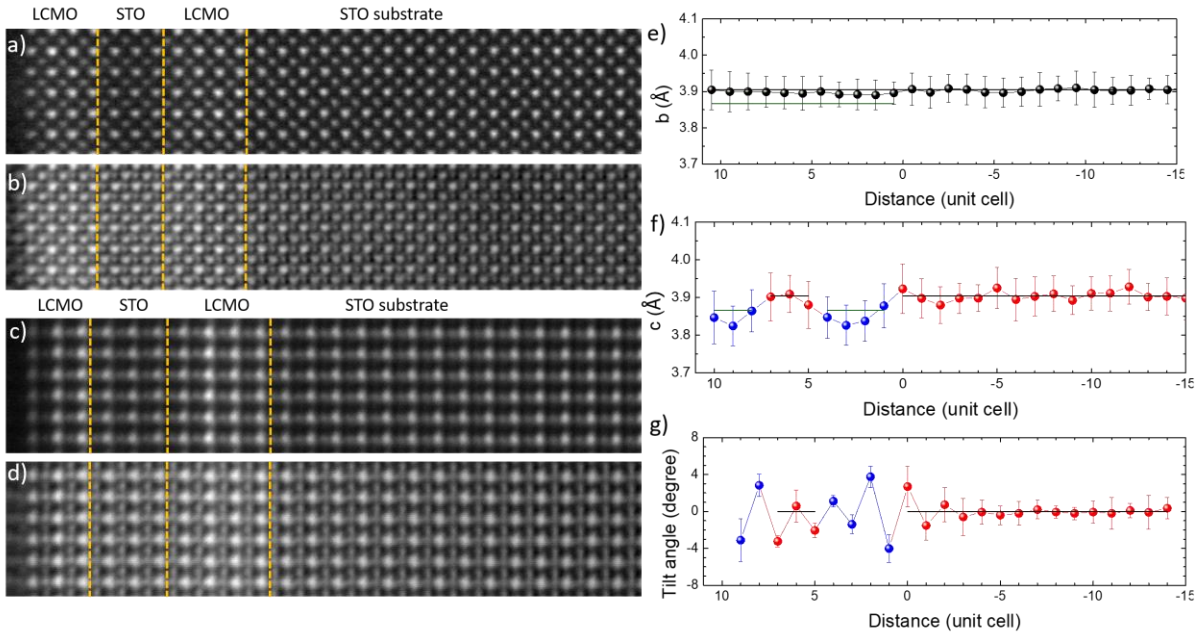

Figure 3.9. a-b) HAADF, ABF images in [100] direction for $LCMO^{4uc}/STO^{3uc}/LCMO^{4uc}$ trilayer. Yellow lines denote interfaces. c-d) HAADF, ABF images in [110] direction for $LCMO^{4uc}/SRO^{3uc}/LCMO^{4uc}$ trilayer. e) IP lattice parameter for every layer in film, averaged across lateral area. f) OOP lattice parameter by film layer. Green line denotes LCMO bulk OOP pseudocubic lattice constant. g) Tilt angle as measured from ABF images.

compared with the SRO sample, where we have a low tilt around 4° near the STO buffer interface as opposed to the 7° in SRO. The reduced tilt means that the LCMO layers must expand OOP in order to release tension and this leads to the expanded c-axis in this sample as opposed to the larger tilt angle in SRO buffered films. The STO buffer layer then reduces the allowable tilt in LCMO layers but does not altogether eliminate it.

If we compare the FFT diffraction obtained from ABF for the SRO and STO films, we find that the overall rotational symmetry of the films are identical. Figure 3.10 shows the FFT's from the two imaged samples imaged for beam directions [100] and [110]. As previously discussed, this allows us to probe all 3 rotational axis for an orthorhombic crystal. Comparing the images, we can see that both samples have the same diffraction patterns for both directions, with intermediate spot formation in the [110] direction but not the [100] direction. This means that both samples occupy

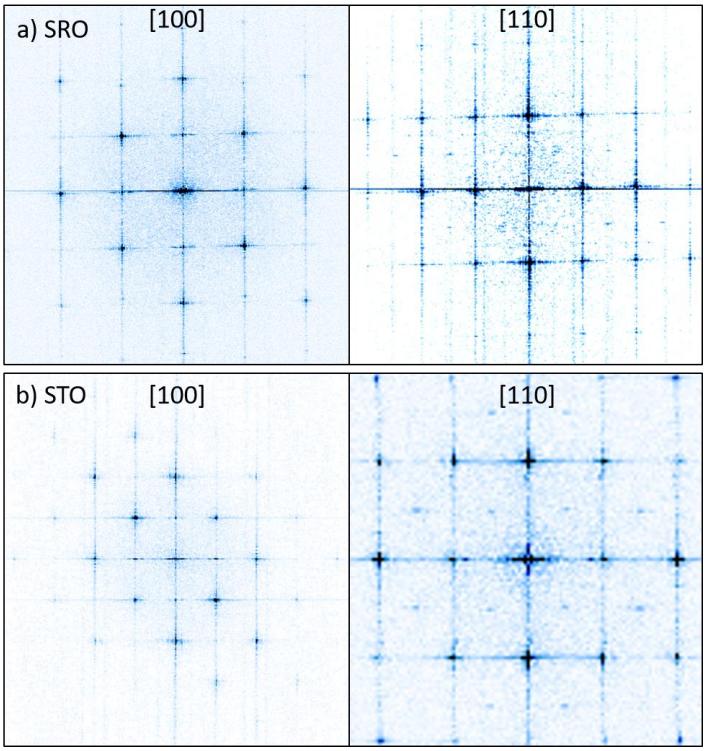

Figure 3.10. ABF-obtained FFT's for a)SRO and b)STO buffered trilayers. First panels show [100] beam directed images, second show [110] directions.

the same $a^-a^0c^-$ *Imma* space group, though we showed that the STO sample does a reduced tilt angle when compared to the SRO buffered trilayer. Magnetism in super exchange systems can be highly dependent on the structural parameters of a film, so in confirming that these films occupy the same structural group we are able to eliminate symmetric change as a potential cause of magnetic differences between these films and instead focus the other structural parameters like lattice constant and tilt angle. We note here that while not shown, preliminary results from CRO buffered samples show the same structural pattern from FFT images as the SRO and STO buffered films, and we therefore conclude that each sample in the discussed set occupies the same rotational symmetry.

While HAADF is excellent for getting a clear structural understanding of a material, it does not have the ability to determine the chemical composition of a film, as its contrast is governed merely by the relative intensity ratio, and especially struggles with imaging lighter elements. ABF imaging is even worse for this purpose, with very little intensity difference between elements despite large atomic number differences. Modern STEM setups can make use of atomic-resolution EELS maps however, which allow us to determine the atomic makeup of our films both inside the layers at near the interface. We have done this for both the SRO buffered trilayer and have plotted the data in Figure 3.11. The STO substrate is pictured on the right while the film layers grow leftward. In the SRO trilayer, we see that the first interface between the STO substrate and first LCMO layer has a noticeable amount of intermixture of the substrate Ti into the first unit cell of LCMO. While this could potentially shift the valence state in this first LCMO unit cell as Ti^{4+}

could dope the layer toward the lower doped FMI end of the LCMO phase diagram, this behavior would be present in all LCMO films grown on STO and yet no novel behavior is observed in monolithic films due to this interface. This Ti mobility is fairly common in thin films grown on STO substrates and not cause for concern about the overall stoichiometry of the trilayer[111, 112]. Only line profile analysis, discussed in the next paragraph, will elucidate if the substrate/film interface is affected by the Ti intermixture. Otherwise, the remaining interfaces between LCMO and SRO layers do not show significant intermixture. The first LCMO layer has very sharp Mn-layer termination followed by an Sr layer, as expected for this interface. As SRO is grown however, we see that the second interface going from SRO to LCMO has a RuO_2 – (La,Ca)O termination

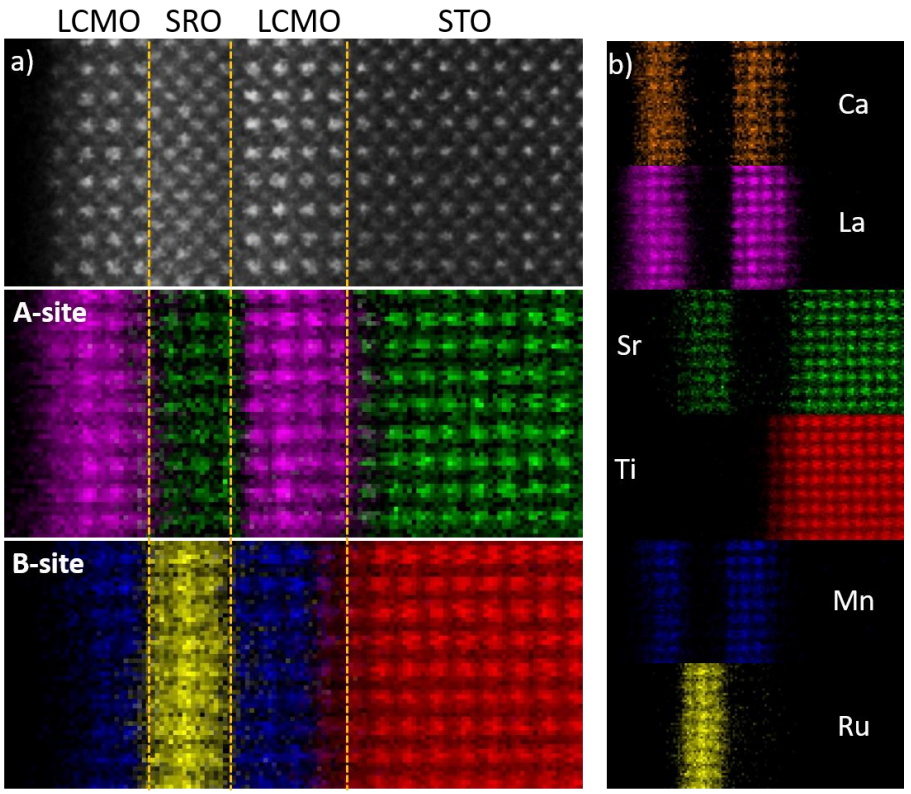

Figure 3.11. EELS atomic resolution data for SRO buffered film. a) HAADF imaged area along with simultaneously acquired EELS maps in middle and bottom panel. Middle panel shows A-site atoms (La and Sr) and bottom shows B-site (Ti, Mn, and Ru). b) Element separated EELS map.

structure. This is interesting in that SRO is well-established as having a termination conversion that occurs during the first unit cell of its growth, and our RHEED measurements seemed to agree with this picture. A similar behavior has been seen in other manganite – SRO heterostructures, and it has been suggested that the absence of the normal SRO termination conversion is due to a chemical driving force that forces the normal SrO termination layer to intermix with the interfacial manganite A-site layer [113]. Our EELS data does seem to bear this out, with a small amount of Sr interdiffusing into the first (La,Ca) near the top interface. This interdiffusion is also enhanced by the high temperature growth and quick succession of heteroepitaxial growth of the top LCMO layer on SRO as the termination-converted surface is more volatile in this case and has little time to condense before the LCMO layer is grown. The Ru-terminated surface has been suggested to

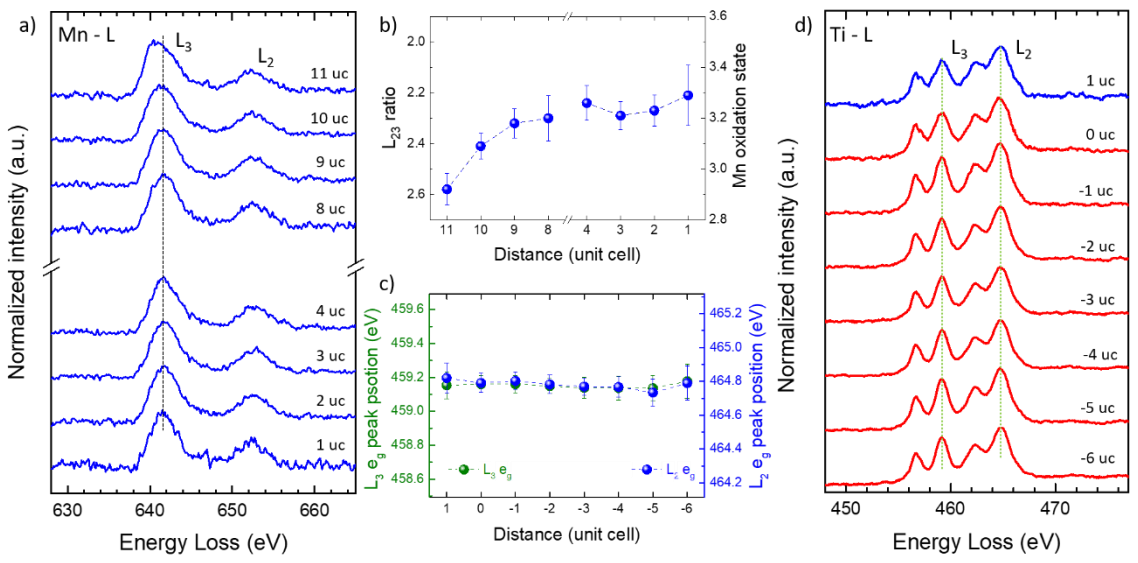

Figure 3.12. EELS line profile analysis for for $LCMO^{4uc}/SRO^{3uc}/LCMO^{4uc}$ trilayer. a) Mn $L_{2,3}$ edges for each LCMO layer. Indicated unit cell refers to distance away from STO substrate. Black line is a guide for the eye for the L_3 edge peak position. b) L_{23} (white—line) ratio and commiserate calculated Mn oxidation state as a function of distance from substrate. c) Ti peak position mapped away from interface with LCMO. d) Line profile for Ti L-edges, again with green guides for the eye.

have weaker interfacial coupling with manganites than the SrO terminated equivalent structure [114, 115].

The EELS elemental maps are formed by taking the known L and K core level edges and mapping how the line profile changes as the beam is scanned. The profiles themselves can also be analyzed to look for changes in the chemical valence of a given element, as disparate valence states can alter which levels can be filled with excited electrons. As charge transfer has been suggested as a potential source of revived magnetism in manganite-ruthenate heterostructures, it is imperative that atomic resolution EELS be done so that the interface where the potential doping occurs can be compared to Mn-layers away from the interface[63, 116–118]. This is a primary reason that we grew exterior layers of LCMO as opposed to placing the LCMO in between SRO layers, so that the difference between the interface with SRO did not dominated the entire manganite film. Line profile analysis is shown in Figure 3.12. Panel a) shows the 5nm-averaged layer-by-layer spectra in the known Mn L-edge range, with the dashed line indicating the peak position of the L_3 edge and the "0 unit cell" indicating the top substrate layer. Unit cell 1 is then the first grown layer of LCMO. We can see that the L_3 position, with the exception of the two topmost layers of Mn, occupy the same energy loss position. The topmost layers do show a difference from the rest of the film, but this is attributed to the harsh sample preparation needed for EELS measurement that can damage the surface and extrinsically change the valence state [119, 120]. Damage would not have been present during physical property measurements either, as they were acquired before STEM acquisition, and we therefore neglect the role of this surface shift in any observed physical phenomena. The remaining film layers do not show any Mn valence shift near the interface (unit cells 4 and 8) relative to the rest of the film. The L_{23} (white-line) relative intensity ratio shown in Figure 3.12b) also confirms that the filling of the Mn 3d-orbital is not changed between the

different layers, as the L_2,L_3 ratio is directly related to the allowed transitions to the energetically nondegenerate 3d orbitals. We therefore do not observe appreciable charge transfer between the SRO buffer and LCMO layers. The role of the Ru-termination is discounted here, because if this were the driving factor limiting charge transfer we would expect a difference between the 4th and 8th LCMO unit cells where the interfacial layers differ. A reduced metallicity due to the ultrathin SRO thickness may affect its ability to effectively dope the manganite layers. We also note that the ~3.3 Mn oxidation state (left-hand side of Fig 3.12b) is near that of the stoichiometric $[La_{.67}Ca_{.33}]MnO_3$ target, another indication of quality growth without the introduction of oxygen vacancy or other element deficiencies. We also look at the substrate Ti valence state in comparison with the Ti that interdiffuses into the first LCMO layer, as shown in Figure 3.12c-d). The peak positions remain the same for each of the 7 layers beneath the substrate interface and for the interdiffused Ti layer. Similar to the Mn valence, no observed position change denotes an absence

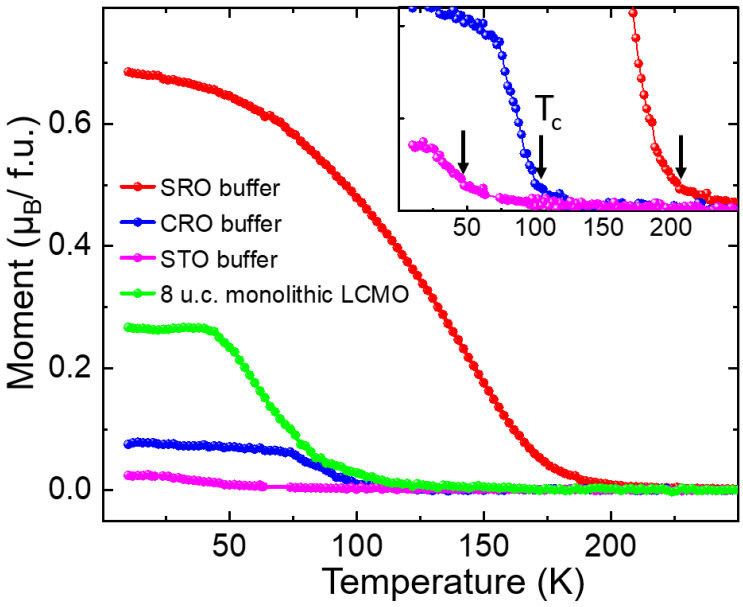

Figure 3.13. M(T) data for LCMO^{4uc}/Buffer^{3uc}/LCMO^{4uc} trilayer set, compared with the same thickness of monolithic LCMO grown on STO (001). Inset shows closeup for buffered heterostructure magnetic transitions.

of Ti valance change and therefore no charge transfer between the LCMO layer and insulting STO. As no change is observed in any of the white line spectra for this SRO sample, which would have

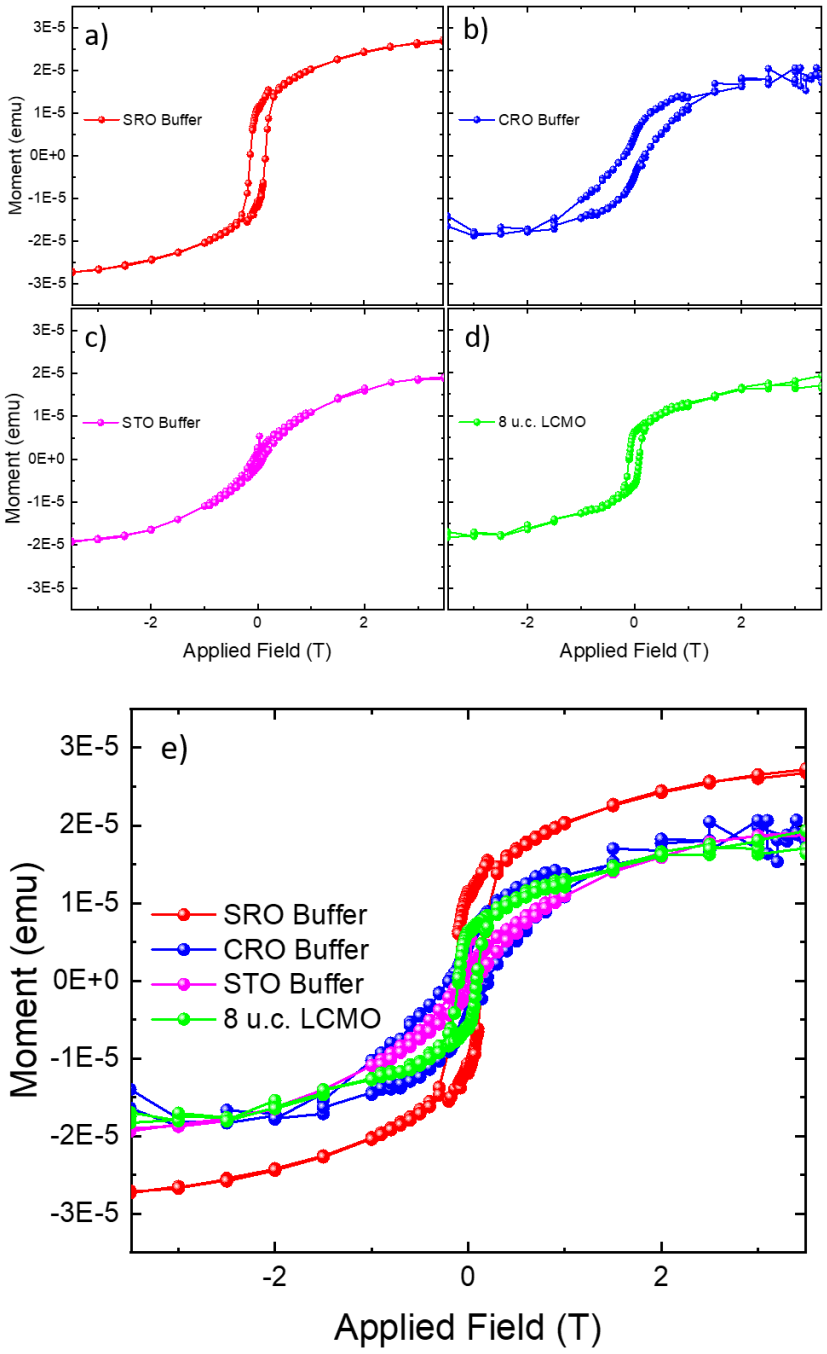

Figure 3.14. Magnetization vs external applied field for a) SRO, b) CRO, and c) STO buffered trilayers, as well as d) monolithic 8uc LCMO. e) Composite of a-d) for direct comparison.

the highest probability of valence change between each of the buffered trilayer films due to SRO's more metallic nature, we do not consider this mechanism as a viable option for any observed effects found in these films.

3.3. Magnetic Enhancement

Magnetic measurements utilizing a SQUID were carried out to determine how the addition of a buffer layer could affect the previously established magnetic characteristics in LCMO thin films. Each of the $LCMO^{4uc}/Buffer^{3uc}/LCMO^{4uc}$ trilayers is compared with an 8 unit cell monolithic LCMO film in Figure 3.13 using a 100 Oe field-cooled measurement technique. The compared monolithic film has the same total thickness of LCMO as the trilayers with an unbroken chain of Mn octahedron that should make it more functional than discontinuous buffered films. The green monolithic film curve does seem to outstrip the STO and CRO buffered films in this way, with a higher observed T_c of 123K in 8 u.c. LCMO versus the CRO T_c of 99K and STO 42K. However, as can clearly be seen for the red SRO buffered film, the magnetic onset temperature (198K) is substantially above that of the 8 unit cell monolithic LCMO film. A comparison of this onset temperature with the monolithic films in Figure 3.2 show that this SRO buffered film has a higher T_c than the 60 unit cell monolithic film (190K). This is our first indication that the magnetic stabilization in these films may be different from that seen in other LCMO films, as even in this 60uc thick monolithic fully metallic film which should optimize the DE-FM mechanism, we see that the SRO buffered trilayer outstrips its onset temperature. We note here that calculation of the Bohr Magneton per formula unit (μ_B/f.u.) used in our MT and forthcoming MH data assume that the SRO buffer layer contribute considerably to the magnetic signal observed while the CRO and STO layers are not. Neither CRO nor STO buffer layers show FM behavior under normal conditions and do not show any indications of FM here and are therefore assumed not to contribute.

The SRO layers do seem to be magnetically active and are therefore the Ru atoms are included with the Mn atoms as magnetic formula units. Magnetic hysteresis data can give us information about the net saturation moment the films achieve at high applied fields, as well as its coercive and remnant fields and any exchange bias behavior. The 5K MH curves for each buffer layer are shown in Figure 3.14a-d), with a composite shown in 3.14e) for clarity of net magnetization overlap. It is clear that for the three films with reduced magnetization, 8 u.c. LCMO and the STO and CRO buffered samples, that they all have similar net magnetization while the SRO sample again has a higher magnetic response. This behavior may have multiple causes. We know from the DE model that a larger overlap of oxygen 2p orbitals increases the DE interaction strength and that a 180° angle between the Mn-O-Mn orbitals maximizes this overlap. Simple geometric arguments can also explain why more parallel crystal octahedra allow for a higher saturation moment. STO and CRO buffered samples have distinctly different tilt and rotation patterns in this system as shown previously, but the bulk-like CRO buffered sample and the suppressed STO buffered trilayer have similar net moments. The monolithic LCMO has a higher T_c than both, and a reduced tilt angle as well, yet its saturation moment is the same. As the magnetic onset and tilt pattern for each of these films are so different, it is interesting that at low temperature and high field the moments end up aligning to a similar degree. This may be due to the reduced tilt STO and monolithic films allowing for similar saturations while the CRO trilayer has some enhancement due to the Ru-Mn interfacial bond that then is mitigated by the enhanced rotation. SRO has the best of both worlds however, with a more optimal tilt angle compared to bulk and enhanced magnetic onset.

The shapes of the hysteresis curves also belies some crucial information. The SRO and monolithic films have the more boxlike FM curves, the prototypical FM hysteresis loops, while the CRO sample has a small “wasp waist” hysteresis seen in ruthenates and their heterostructures

with manganites[122–124]. This wasp waist is understood by the presence of two different hysteretic behavioral domains within a single sample, one of which is a relatively harder magnet than the other[125]. The easy magnetic domain flips and brings down the overall magnetization, and then only after enough field is applied does the hard magnet flip and both domains reach saturation. In this sample, we know that the monolithic LCMO and SRO buffered samples have a reduced in-plane tilt throughout the films and no wasp waist is observed. However, the CRO sample has an increased tilt near the interface with LCMO but a reduced tilt near the substrate. These structural domains are likely to create two separate magnetic domains within the film, one of which has a harder magnetic easy axis than the other, producing the observed slight wasp waist. For the STO trilayer, almost no coercive field is observed and the remnant field is only slightly above a paramagnetic background. Full magnetic hysteresis properties are listed in Table 3.2.

Table 3.2. Magnetic hysteresis characterization data for buffered trilayer set and monolithic LCMO

Sample	Saturation Moment (μ_B/Mn)	Remnant Field (%)	Coercive Field (Oe)	Exchange Bias (Oe)
SRO Buffer	2.52 ± .029	41 ± .5	1600 ± 200	0 ± 200
CRO Buffer	1.94 ± .175	25 ± 2.2	1900 ± 200	0 ± 200
STO Buffer	1.89 ± .086	10 ± .5	900 ± 100	0 ± 100
8uc Monolithic	1.83 ± .157	34 ± 2.9	1000 ± 100	0 ± 100

Exchange bias is typically seen in materials with antiferromagnetic exchange coupling between two different magnetic domains or materials as discussed in Chapter 1. Its existence in the LSMO-SRO system is explained by an altered electronic nature near the interface, potentially due to charge transfer mediated by the Mn-O-Ru bond, that induces a negative $J_{exchange}$ between the layers and an overall AFM coupling of the Mn and Ru layers. We do not observe any exchange bias fields in our ruthenate-manganite trilayers, which under this charge transfer picture is the

expected result. However, the absence of exchange bias here may be linked to other factors arising from the ultrathin nature of these films, such as a reduction in magnetocrystralline anisotropy, and not observing it here is not sufficient to rule our AFM interfacial alignment in this system.

3.4 Novel Insulating Magnetic Regime

Understanding the resistive properties of the films may elucidate the underlying mechanisms that are driving the enhanced magnetic characteristics of the $LCMO^{4uc}/SRO^{3uc}/LCMO^{4uc}$ trilayer. We undertook simple four probe measurements and measured the trilayered films' temperature and field dependent resistivities as shown in Figure 3.15. Recall from Figure 3.2 that the 8 uc LCMO film is completely insulating, as well as the 12 uc monolithic film. Each of these films follow suit, with a fully insulating state and no MIT

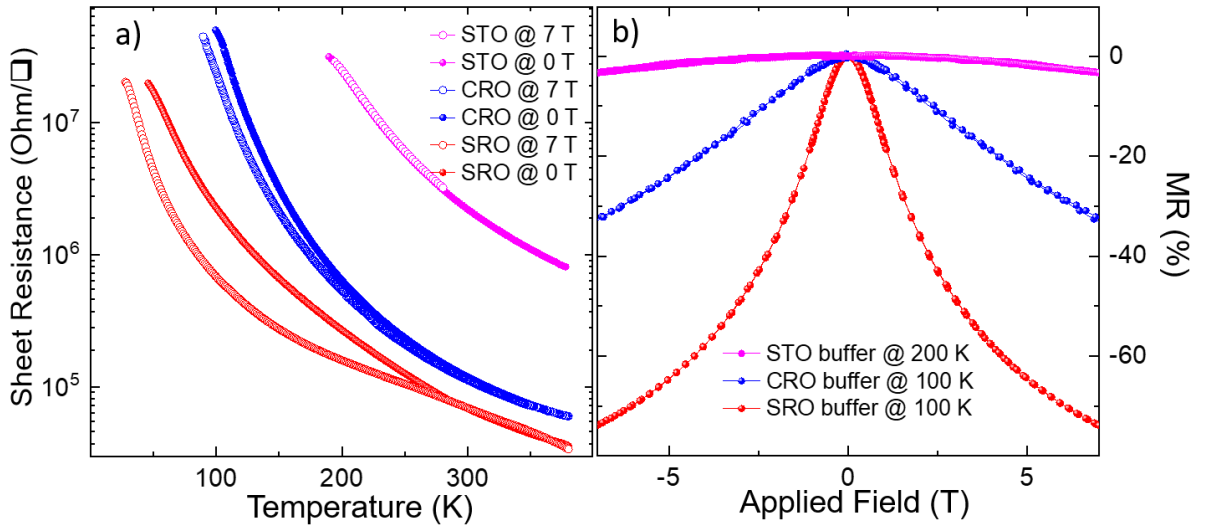

Figure 3.15. a) R(T) data for $LCMO^{4uc}/Buffer^{3uc}/LCMO^{4uc}$ buffered ultrathin films at 0, 7T applied OOP during acquisition. Red curves indicate SRO buffered samples, blue indicate CRO films, and magenta indicates STO films. All films maintain insulating behavior b) R(H) taken at different temperatures for the trilayers in a). 200 K was chosen as the lowest measureable temperature for STO film given PPMS constraints, while 100 K was chosen as the lowest measureable for CRO buffered sample. SRO was taken at 100K for better comparison.

occurring as it does in the thicker LCMO films. This behavior shows that we are in a drastically

different magnetic regime from the classically understood DE model for FM in manganites which necessitates a metallic e_g electron hopping state. We also note the absence of any SRO shorting behavior where the resistive behavior of the film is dominated by a metallic layer. SRO is metallic at this thickness on STO(001) substrates, and other studies of SRO underneath STO capping layers show that SRO's metallic behavior can be seen through the insulating STO layers and is not destroyed by the rotational and epitaxial strain applied by SRO's confinement. Three unit cells is generally considered to be below the MIT critical thickness for SRO, but a recent study by Boschker *et al.* has shown that SRO films down to a single SRO layer can have some metallic behavior above 120K and suggested that the insulating behavior previously seen was only due to disorder effects[126–128]. Because our films are heteroepitaxial, they cannot achieve the same degree of crystal uniformity as the nearly homoepitaxial growth of a single RuO_2 layer amidst a larger SrO-TiO_2 structural matrix, and we therefore assert that our SRO growth is still of high quality and in alignment with other heteroepitaxial films that are insulting at this thickness.

The fact that the $LCMO^{4uc}/SRO^{3uc}/LCMO^{4uc}$ trilayer is fully insulting and still has a T_c of 198K means that we have moved from a fully DE magnetic regime to another. While multiple potential causes will be discussed, we discuss here the possibility of magnetic JT polarons as a potential source of the overserved phenomena. As discussed in Chapter 1, JT polarons can mediate magnetism in a system if the hopping electron obey's Hund's rules. Optical studies have suggested a magnetic polaron state in the low-doped LCMO FMI phase[47]. This type of insulating state should manifest as polaronic motion in the resistivity behavior[129]. Models have been developed for different types of insulating behaviors in films, and here we will consider the two major mechanisms found in manganites, activated hopping and polaronic motion[130]. We looked at activated hopping models of the form $\rho = \rho_\infty * \exp(\frac{T_0}{T})^n$, where ρ_∞ is the high temperature

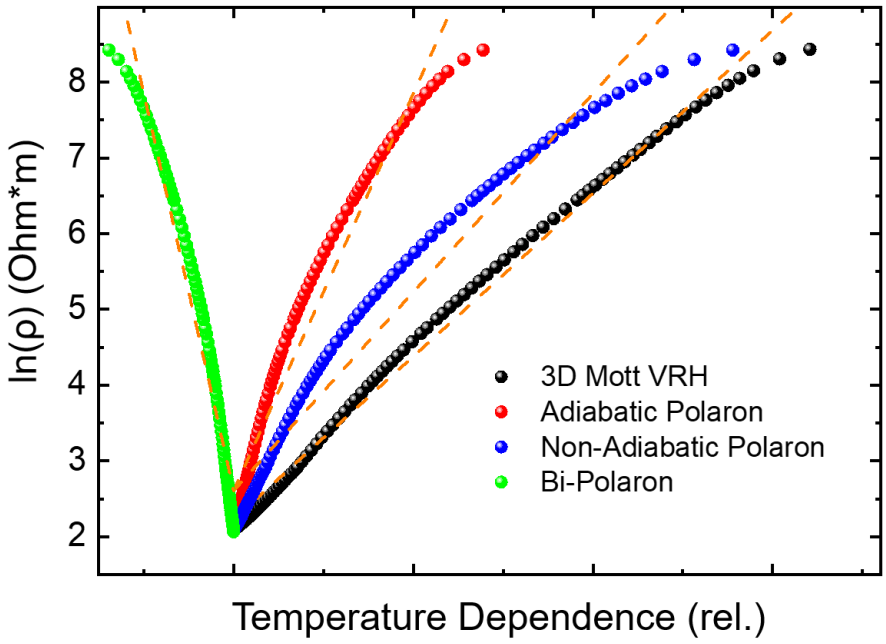

Figure 3.16. Fitting of R(T) data with theoretical models for insulating behavior in perovskites. 3D VRH fits our data better than polaron hopping, with orange lines showing the linearized best-fit lines for each model.

resistivity limit that depends on the phonon density in the material, T is the temperature in Kelvin, T_0 is the characteristic temperature that depends on both the localization of the hoping electrons and the Fermi energy DOS, and *n* can be either 1, 0.5, .333, or 0.25. These different *n* values correspond to different hopping regimes, where *n*=1 obeys an Arrhenius thermally activated hopping, *n*=0.5 corresponds to a Coulomb gapped DOS hopping model, and *n*=.333, 0.25 denotes a 2D, 3D Mott variable range hopping (VRH) state. The 3D VRH allows hopping in any direction while the 2D hopping is constrained to a single plane usually due to bond elongation in a single direction. Each of these possible models was also compared to polaron hopping models of the form $\rho = \rho_0 * T^n * \exp\left(\frac{E_a}{k_B * T}\right)$, where ρ_0 is a prefactor, E_a is the hopping activation energy, k_B is Boltzmann's constant, T is the temperature in Kelvin, and *n* again determines the type of polaron hopping seen. Adiabatic polaron hopping has an *n*=1 behavior, where *n*=2 is for non-adiabatic hopping and *n*=-0.5 is for coupled bi-polaron hopping. Comparing each of these different models,

we find that 3D Mott VRH fits our data for the $LCMO^{4uc}$ / SRO^{3uc}/ $LCMO^{4uc}$ trilayer better than any other models, and in Figure 3.16 we show a normalized curve comparison of the different

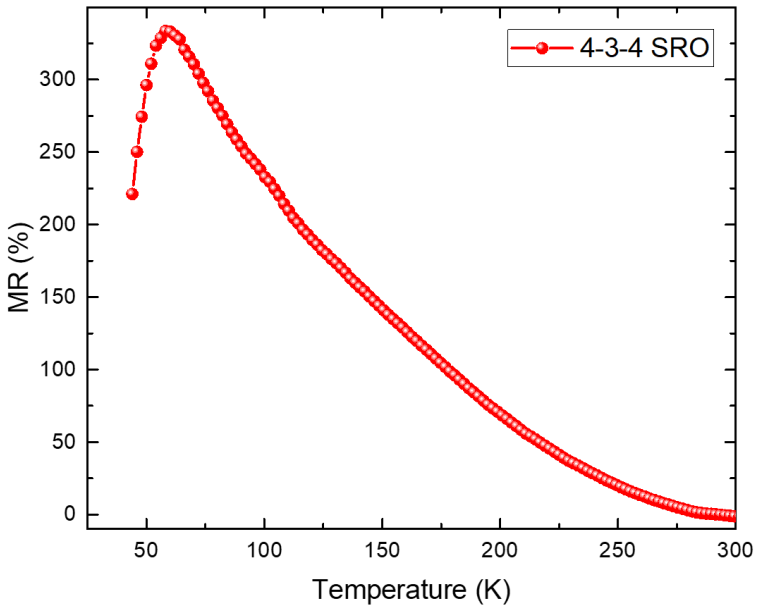

Figure 3.17. MR ratio for $LCMO^{4uc}/SRO^{3uc}/LCMO^{4uc}$ trilayer as calculated from Figure 3.15 data.

plotting models against our data. Mott VRH has been seen in the high temperature (above 300K) insulating state of LCMO bulk crystals and is attributed to an increased localization of charge carriers due to random fluctuations in the Hund's exchange energy [131–133]. As polaronic motion has not been seen in our LCMO doping regime and the VRH model holds for all temperatures in our SRO buffered trilayer, we therefore discount the potential role of JT magnetic polarons in this system.

Returning to the field-dependent resistivity curves at select temperatures shown in Figure 3.15, we see that the SRO film once again has the largest magnetic behavior with an MR ratio of 73% at 100K and 7T. At 100K, the CRO trilayer has an MR of 33% and the STO trilayer has a negligible 3.2% at 200K, though this is well above any potential magnetic stabilization in the STO

film. We note that these temperatures represent a relative lower limit of measurement for CRO and STO samples because the insulating behavior begins to run into the detection limits for our PPMS setups. The MR ratio for these curves is calculated as $100 * \frac{R(0)-R(H)}{R(0)}$, which puts a hard limit of 100% on MR with an order of magnitude difference at 90%. Each film has a closed resistive hysteresis, and each remains fully within the negative MR regime for every field value. The SRO trilayer has a large MR, above that of most GMR materials, and yet does not display a maximum in MR near its T_c as is expected for typical CMR DE-mediated ferromagnets. Plotting the MR ratio between 0 and 7T as a function of temperature for the SRO trilayer is shown in Figure 3.17. The MR ratio plotted here utilizes the alternative definition of MR = $100 * \frac{R(0)-R(H)}{R(H)}$ which allows for larger than 100% with an order of magnitude difference at 1000%. A consistent increase in the MR ratio is observed over the temperature regime with the exception of the lowest temperatures. This tail is attributed to the detection limits of our PPMS setup as the 0T data runs into the resistivity maximum at the observed inflection point, and is not considered intrinsic. If the magnetism in this film was mediated by DE domains within a larger paramagnetic insulating matrix, as has been suggested in the lower doped LCMO FMI phase, then we would still expect an inflection point in MR as the metallic pockets were formed and the overall resistance of the film was lowered. As no inflections are observed near T_c in our magnetic $LCMO^{4uc}/SRO^{3uc}/LCMO^{4uc}$ trilayers, we do not believe that small metallic DE regions are at the root of the observed magnetism here.

3.5 Layer Ordering and Repetition Effects

We have examined the structural, magnetic, and electronic properties of three ultrathin $LCMO^{4uc}/Buffer^{3uc}/LCMO^{4uc}$ systems and compared them to pure monolithic films on the same substrates. This arrangement of LCMO external layers was chosen so that the buffer interface would not dominate the entire LCMO film but would rather be a component of it that could be analyzed in tandem with the affects near the substrate and surface. If we however switch the

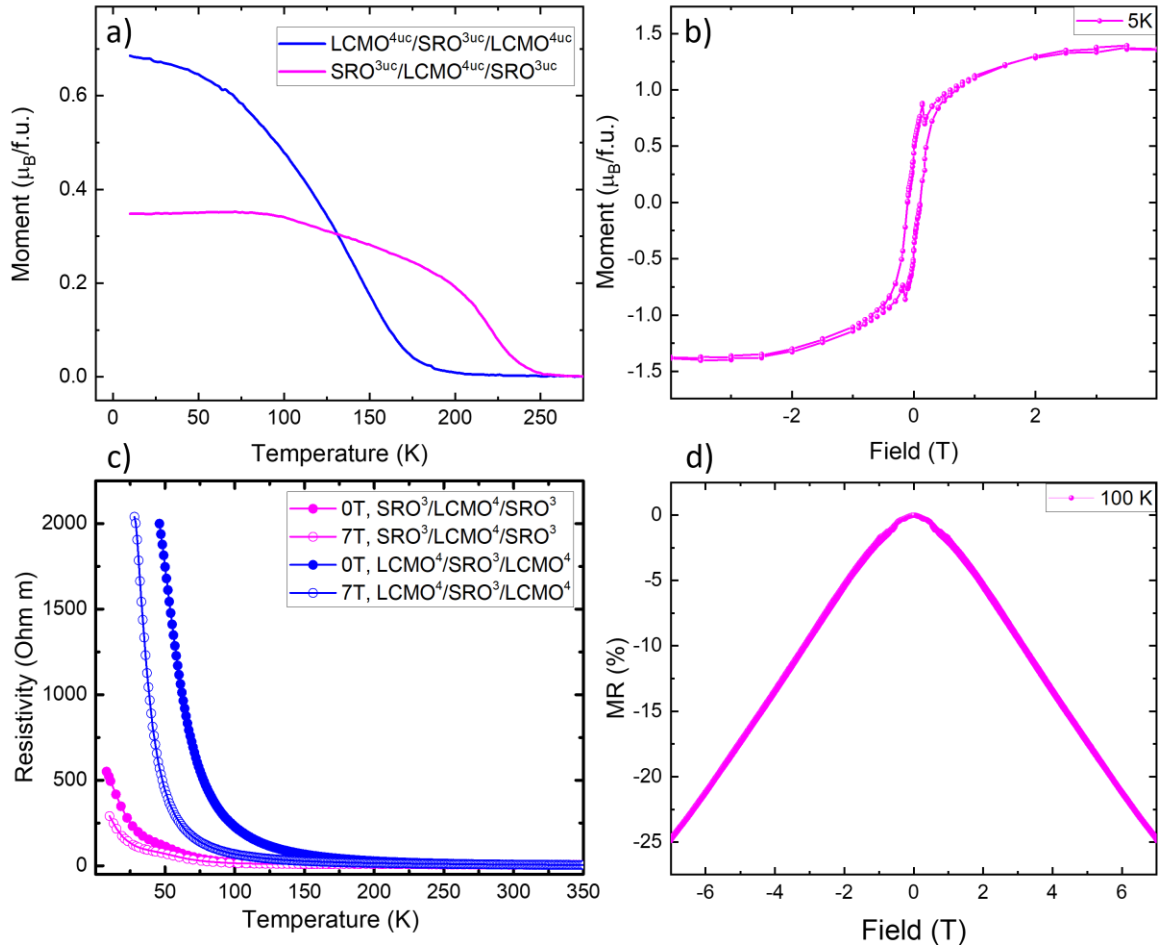

Figure 3.18. $SRO^{3uc}/LCMO^{4uc}/SRO^{3uc}$ trilayer data. a) comparison between LCMO exterior and SRO exterior samples M(T) characteristics. b) IP M(H) curve measured at 5K. c) Field dependent R(T) at 0 and 7T, compared between LCMO exterior and SRO exterior samples. Exterior SRO is still fully insulating, though with lower resistance than LCMO exterior trilayers. d) MR curve taken at 100K for comparison with LCMO exterior data.

trilayer arrangement such that the LCMO is sandwiched in between the SRO layers in an $STO^{substrate}/SRO^{3uc}/LCMO^{4uc}/SRO^{3uc}$ arrangement, we can see from Figure 3.18 that a different magnetic behavior emerges. The T_c in this reversed trilayer is 246K, substantially above that of the former SRO buffered sample and even above that of bulk LCMO. Because this film has a higher T_c than the LCMO exterior trilayer and yet only contains a single four unit cell layer of LCMO, we can be sure that it is LCMO's interfacing with SRO that is driving the enhanced T_c and not any coupling between LCMO layers. If termination conversion occurs in the first SRO

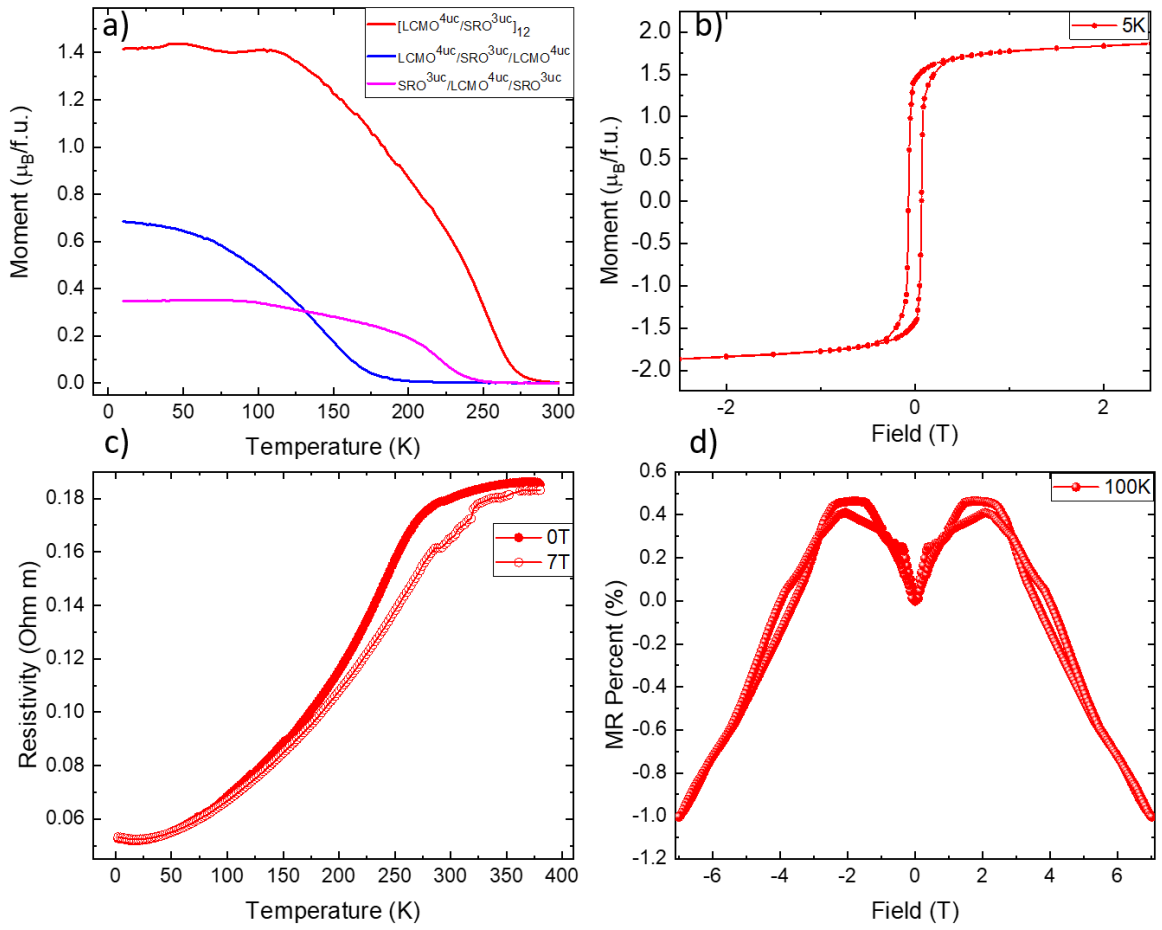

Figure 3.19. Data for $[LCMO^{4uc}/SRO^{3uc}]_{12}$ heterostructure. a) Comparison between LCMO exterior trilayer , SRO exterior trilayer, and large heterostructured samples' M(T) characteristics. b) IP M(H) curve measured at 5K. c) Field dependent R(T) at 0 and 7T. d) MR curve taken at 100K for comparison with LCMO exterior data.

layer as it typically does when grown on STO substrates, then it is likely that this reversed sample has two SrO-MnO_2 interfaces as opposed to the single Sr-Mn seen for the LCMO/SRO/LCMO trilayer through our EELS data. This interfacial bond has been suggested to induce a higher degree of exchange coupling between the layers (-13.3meV for SrO-MnO_2 as opposed to -4.5meV for [LaCa]O-RuO_2), and the additional preferred interface may induce this enhanced magnetic onset between the two samples[114, 115]. We also note the distinctly different curvature, which reaches a maximum around 100K and then stops increasing. The cause of this will be investigated, but based on these results could either suggest magnetic saturation of the LCMO moments or a competition between magnetic domains below this temperature. At 5K, this SRO dominated film does not reach the same total magnetization as the LCMO dominant film in the M(T) data. These curves are taken IP and with only 100 Oe of applied field during the field-cooled measurement however, and SRO on STO(001) has a large magnetocrystalline anisotropy that creates a hard magnetic axis in the OOP direction, and we would expect that this small IP field would not be enough to align any SRO moments. From Figure 3.18b) we can see that this reduced IP saturation moment extends to the high field region as well, with a total saturation moment of 1.35 μ_B/f.u. However, this calculation is based on an averaging of the total magnetic signal over the entire 10 u.c. sample and may be due to SRO's OOP preferential direction and the reduced number of LCMO layers, as SRO has a theoretical saturation limit of 1 μ_B/Ru whereas LCMO has a limit of 3.67μ_B/Mn [134–136]. This SRO exterior trilayer is still fully insulating from Figure 3.18c) with only a slight kink far below the FM transition temperature, once again showing that the magnetism in such a system is not directly linked to any net metallicity or metallic domains. Compared to the LCMO exterior trilayer however, the SRO/LCMO/SRO trilayer does have a lower overall resistance, as might be expected as SRO tends to have a lower resistance than LCMO at the same

layer thickness. At 100K, the MR characteristics show reduced percentage when compared to the other ruthenate heterostructures, but this again may be linked to the reduced number of LCMO layers in this sample the CMR effects are typically found manganites. Overall, we find convincing evidence from the comparison of these two samples that increasing the percent of the LCMO layers that are subject to an interface with SRO increases the magnetic onset temperature and is likely related to the number of SrO-MnO_2 interfaces in particular.

Trilayers were used in this study for limit the number of crystal defects or layer shorting behaviors that can be introduced by the repetition of heteroepitaxial surfaces and interfaces. We did however compare the physical properties of our interface-focus trilayer results with our larger $[LCMO^{4uc}/SRO^{3uc}]_{12}$ heterostructure used for crystallography. These results are shown in Figure 3.19. We see further T_c enhancement in this sample with a T_c of 280K far above the transition temperature for both SRO and LCMO bulk crystals, as well as an extension of the curvature change observed in the $SRO^{3uc}/LCMO^{4uc}/SRO^{3uc}$ sample. The flattening occurs around 112K in this curve. It is notable that this effect only begins to occur below the SRO transition temperature, and this effect will be explored further in Chapter 4. The inflated T_c may be related to change in resistive behavior, as this sample has converted to a fully metallic character across all temperatures. From our study here on the trilayers we know that these thicknesses of SRO and LCMO should be insulting even when interfaced with one another, and we can then attribute this change to extrinsic effects such as shorting between inhomogeneous layers, defect formation, and an overall change in the dimensionality of the system moving from 2D to 3D. This type of discrepancy is why it is better to grow thin structures for property measurements even if the signal is reduced so that intrinsic effects are not hidden by other artificially introduced deformities. We note in this sample a characteristic change in the MR ratio as well. While the MR ratio is much lower at 100K than in

other films, this is expected as this film has moved to a more metallic LCMO state with a maximized MR near the much higher T_c of the film. MR ratio being maximized at T_c is a classic sign of DE ferromagnetism, and it seems that this film has moved to such a state. The MR does however behave differently from monolithic films in that the near-zero field MR actually goes into the positive MR regime before returning negative at high field. This crossover behavior in MR is typically associated with the weak antilocalization effect (WAL) in strong spin-orbit coupled (SOC) systems and has been observed in other SRO heterostructures[137]. We will discuss this effect further in Chapter 4, but this is our first indication that thicker films allow for the strong SOC to become active in the properties observed.

3.6. Discussion and Conclusion

In this chapter, we were able to make important determinations about the enhanced magnetic LCMO system by focusing on the $LCMO^{4uc}/Buffer^{3uc}/LCMO^{4uc}$ set. We found that structural modification between buffer layer materials does not alter the overall rotational symmetry of the film, and that each film occupies the same structural domain with $a^-a^0c^-$ Glazer rotation. The angle of rotation does change however, and may be important for the observed magnetic characteristics in the form of increased electron localization. These films also have a novel SRO buffer layer RuO_2 termination, changing the potential exchange coupling between LCMO and SRO. We also found that reversing the external layer to an SRO layer further increased the magnetic onset, which we ascribe to a reemergence of the SRO termination reversed surface and monolithic SrO-MnO_2 interfacial bond.

We also attempted to elucidate some of the mechanisms behind the observed enhancement in magnetic properties in LCMO/Ruthenate heterostructures, particularly in the LCMO/SRO/LCMO trilayers. We were able to rule out two potential sources of this enhancement,

interfacial charge transfer and JT polaronic motion, through EELS and resistivity modelling respectively. We also do not consider small metallic pockets or interfacial metallicity to be viable explanations. It is however possible that the combination of decreased rotation and exchange coupling at the atomic interface are pivotal in the resuscitation of magnetism. A third potentially important mechanism not discussed before this is the magnetism within SRO itself. While it is known that the macroscopic ferromagnetic onset in SRO is below 150K, some studies have shown small-scale magnetic domains above the normal T_c all the way to 500 K[30, 138]. If these domains are present in our SRO buffer layers, then they might be able to pin the Mn moments IP as a result of the large J_{ex} between the two layers, allowing for easier FM alignment in LCMO layers and inducing the revived magnetism. This would help explain why the CRO buffered material does not enhance the magnetism to the same degree as SRO despite the Ru interfacial bond and same tilt pattern. The causes of this enhanced magnetism will be discussed further in Chapter 4 by looking at multiple thickness regimes of both the SRO and LCMO layers.

One other potential source of magnetism that should be considered is antisymmetric exchange at the LCMO/SRO interface. Ruthenates do have a moderate spin-orbit coupling energy, though it is substantially smaller than those seen in iridates or topological insulating materials due to smaller ionic size. This DM interaction is a type of superexchange interaction that is characterized by a weak ferromagnetism arising from canted antiferromagnetic moments. We have some indication from this chapter and will have further evidence in Chapter 4 that an antiferromagnetic interlayer alignment occurs at the LCMO/SRO interface, so this may be a tempting consideration for our experiments. However, if canted moments are indeed at the cause of our FM signal, we must consider the saturation moments observed in this chapter. By considering the theoretical limit of the Mn and Ru moments in LCMO and SRO, we can set a

minimum number of magnetic layers in our films. It is known that the maximum magnetic moment per Mn in LCMO is 3.67 μB/Mn and for Ru in SRO is ~1μB/Ru [134–136]. Using these as our maximums, and assuming every layer of SRO is ideally magnetic at 5K in the SRO sample, we find that we need a minimum of 6 fully magnetic manganite layers $LCMO^{4uc}/SRO^{3uc}/LCMO^{4uc}$ film. If we further consider that the topmost LCMO layer likely has some structural defects due to incomplete growth which tends to lessen the magnetic signal, then it would seem that entirely aligned LCMO layers are needed throughout the films. It is possible that the interface exhibits a canted antiferromagnetism between SRO and LCMO layers, and subsequent LCMO layers then continue to align FM with the interfacial Mn layer. It is clear however that the observed effect is not purely due to interfacial canted moments but must extend throughout the LCMO layers.

Chapter 4. Antiferromagnetic Interlayer Coupling in Thickness Varied Manganite-Ruthenate Heterostructures

In the previous chapter, we examined LCMO and SRO films in a focused ultrathin regime below the critical thickness of each film layer, as well as exploring the effects due to other buffer layers. We found that the interface between the SRO and LCMO seemed to play a crucial role in the development of a new magnetic character in these films mediated by the SrO-$(LaCa)O_2$ bond and a reduction in IP octahedral rotation of the film. The exchange coupling constant J_{ex} between the material layers can be affected by such structural changes, and likely plays a key role here. J_{ex} can be either positive or negative, with the positive term tending to align the layers ferromagnetically and the negative favoring an AFM moment alignment at the interface. Interfacial coupling has been suggested to be a primary motivator of exchange bias (EB) and AFM interfacial alignment of FM layers in LSMO-SRO heterostructures [64, 114, 139]. It is reasonable then to attempt to examine the role of this interfacial coupling term in heterostructures between the

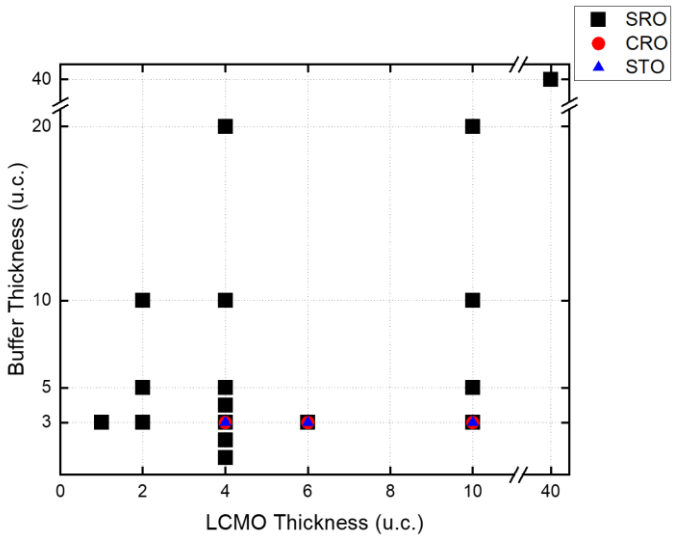

Figure 4.1. Grid representation of $LCMO^m/Buffer^n/LCMO^m$ trilayer films grown.

manganite LCMO and ruthenates SRO and CRO. To accomplish this, a vast suite of various

thickness trilayer heterostructures was fabricated in order to see how the magnetic and resistive properties would change as the films were allowed to leave the ultrathin regime and become self-active. This allows us to understand which results are purely interfacially mediated and which only emerge as the film thickens. The grown $LCMO^{m}/Buffer^{n}/LCMO^{m}$ (m=LCMO thickness, n=Buffer thickness) films available for study are shown graphically in Figure 4.1. We primarily are interested in SRO buffered trilayers as they appear to show the most pronounced magnetic and resistive changes in all thicknesses, but it is important to understand how its behavior deviates from that seen in the CRO and STO buffered systems as well and have grown multiple thicknesses of LCMO with those buffers as well. Through analysis of our physical property data, we will see SRO heterostructures continue to induce the highest magnetic onset, and that a clear IP AFM alignment of the material layers emerges in the thicker metallic films. This suggests a strongly negative J_{ex} between layers that pins SRO moments IP near the interface that can then relax back into its preferred OOP alignment after moving away from the interface. Structural analysis of thick $LCMO^{40uc}/SRO^{40uc}/LCMO^{40uc}$ shows that two mirrored structural domains form in thicker systems that are not seen in the ultrathin samples. This sample also maintains an atomically sharp unconverted Ru-termination layer at the top interface, showing the robustness of this effect on LCMO base layers and perhaps suggesting an origin of the clear 2-step FM onset observed. By varying the thickness of LCMO layers and comparing between different buffer layer behaviors, we find a structurally mediated saturation moment enhancement. Weak antilocalization (WAL) effects again emerge as films become more metallic, as was previously observed in the multiple repetition film in Chapter 4. We conclude with a discussion of these results in light of all thicknesses studied and suggest that a structurally-mediated highly exchange coupled system with stabilized above-T_c IP fluctuations is the most likely explanation for the observed results.

4.1. Growth

Each heterostructure was grown using the same growth conditions listed in Chapter 4, and we expect similar degrees of crystallinity between each film given their similarity in RHEED-observed growth characteristics. We can see from the $LCMO^{40uc}/SRO^{40uc}/LCMO^{40uc}$ trilayer XRD results in Figure 4.2 that we do indeed maintain a high degree of crystallinity and layer thickness control even in thicker films where suboptimal growth conditions can compound into a poor crystalline quality. Experimental coupled scan data matches the simulated pattern for a 40uc layered heterostructure of these materials, and RSM shows that the film maintains a large degree of epitaxial IP strain to the STO substrate, though a certain degree of relaxation is expected for thicker films. Rocking curves show that the mosaicity of the film matches the substrate well

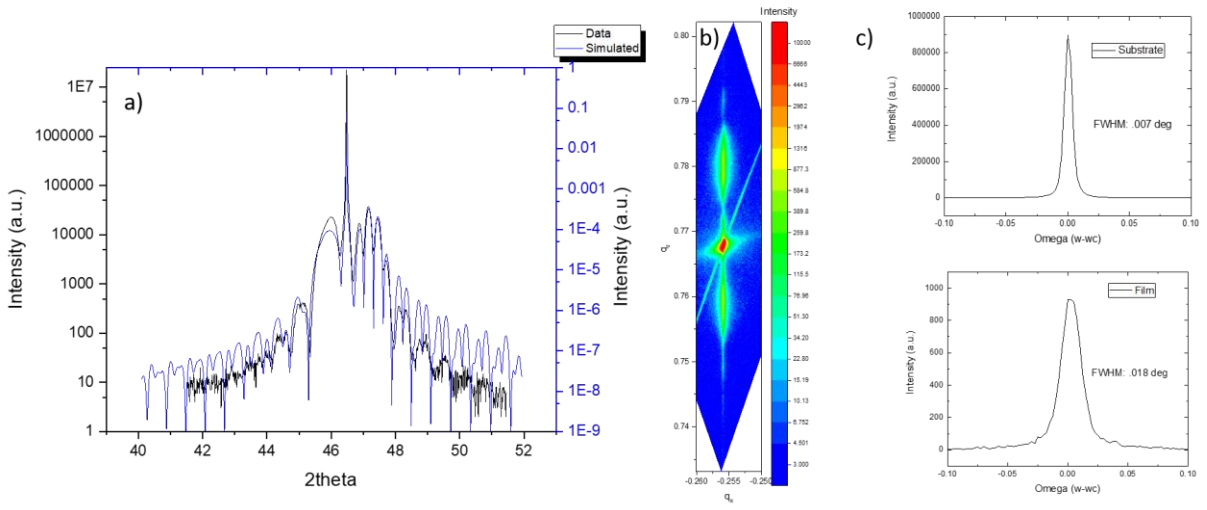

Figure 4.2. XRD Data for $LCMO^{40uc}/SRO^{40uc}/LCMO^{40uc}$ trilayer. a)Coupled scan data (black) matched with simulation data (blue) for an ideal heterostructure with the predicted thickness. b) (-103) RSM plot showing excellent IP (q_x) strain to STO substrate. c)Centered rocking curves of substrate and film peaks at (002) symmetric spot. Shows low mosaicity of substrate, film.

(~.011°). We are confident from this finely tuned control that our samples grown under the same PLD conditions roughly match this degree of crystallinity and layer control, and we therefore trust that our samples are high quality and have the desired sample thicknesses.

4.2. Varying SRO thickness

We will begin this chapter by looking at the effect of varying the thickness of the SRO buffer in trilayers with ultrathin 4uc LCMO layers. Previously, 3uc of SRO had been used to completely separate the LCMO layers and not allow for crosstalk while still maintaining a sub-critical thickness SRO layer. If we however reduce the thickness of the SRO layer down to a single unit cell, the magnetic onset is still drastically enhanced above monolithic films, as seen in Figure 4.3. The magnetic onset is brought to 188K, only 10K below that of the 3uc SRO trilayer and within the margin of error. We can make two observations from this behavior alone. First off, if crosstalk between LCMO layers were the primary motivator of enhanced FM in this system, we would expect that lowering the buffer layer thickness would enhance this effect beyond the thicker

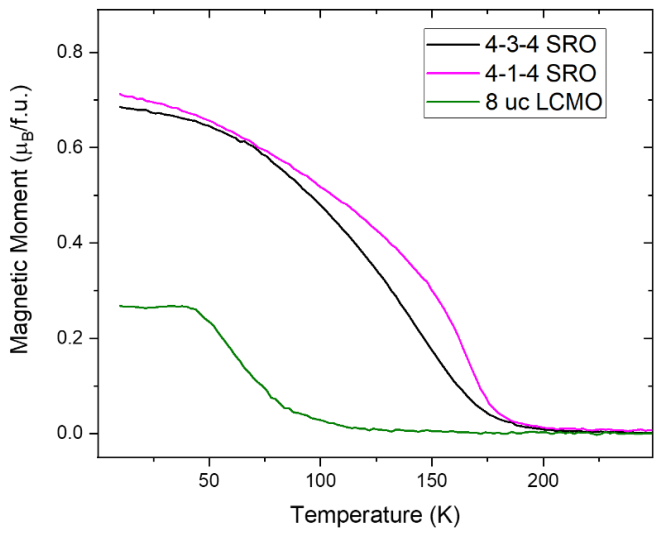

Figure 4.3. M(T) SQUID data for ultrathin trilayers and monolithic LCMO for comparison.

film. As this is not the case, we confirm that LCMO interlayer coupling is not the primary motivator in such a system. Secondly, we would expect a smaller degree of T_c difference between the 1uc SRO buffered film and the 8uc monolithic film if structural change in the LCMO layers was the primary driver of this onset revivification. The single unit cell of SRO should be

structurally dominated by the 8uc of LCMO surrounding it, and single unit cells of SRO have been shown to be structurally symmetric to their surrounding layers in single atomic layer cases[128]. Magnetic onset difference between the two films is ~80K however, which would suggest then that interfacial structural modification is not the primary driver of onset enhancement. This matches well with our observations from Chapter 4, where each buffer layered system had the same FFT-

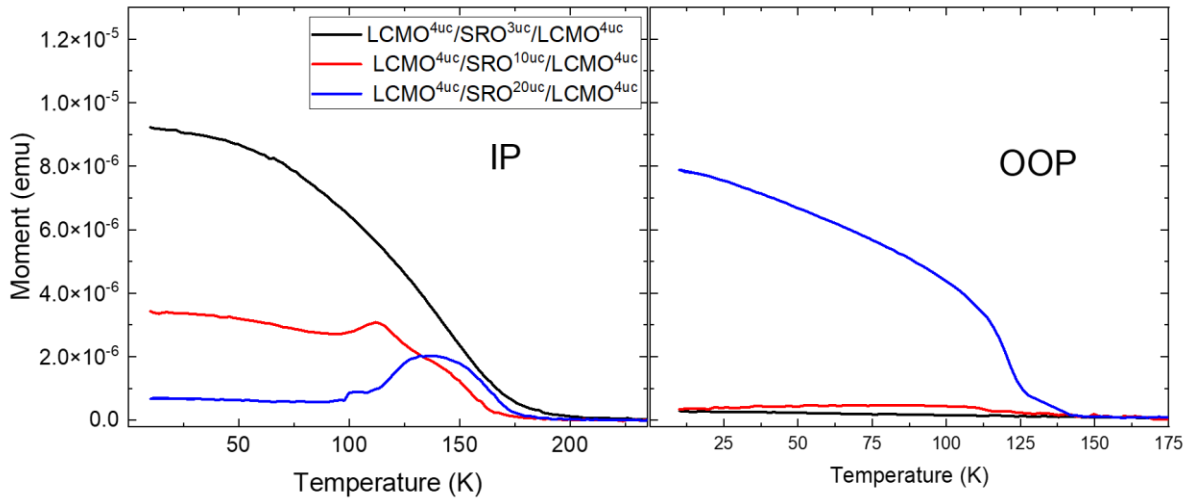

Figure 4.4. In-plane (IP) and out-of-plane (OOP) M(T) data for 3, 10, and 20uc thick SRO buffered films in 4uc LCMO trilayers.

observed symmetry change but had vastly different T_c's. We must therefore consider electronic and magnetic coupling between the SRO and LCMO layers as the primary motivator of enhance magnetic onset in these systems.

If we instead increase the thickness of SRO beyond its critical thickness, we see that a distinct change occurs in the magnetic anisotropy of the overall film. Figure 4.4 shows the SQUID-acquired M(T) data for three trilayer films with SRO buffer thicknesses of 3, 10, and 20uc. The LCMO thickness is kept at the ultrathin 4uc thickness. The IP-measured T_c remains high relative to monolithic films as the thickness increases, though there is an appreciable decline in T_c between the ultrathin 3uc case and the thicker buffers. More strikingly, a multi-humplike behavior emerges

in these thick SRO samples. The first change appears 136K, which is a typical T_c for thin film SRO samples on STO. At this temperature, the 10uc curve has a slight inflection point while the 20uc film has a full magnetic reversal point and as the temperature is lowered the overall magnetic signal decreases. As this transition coincides with the known magnetic onset in SRO layers, we conclude that SRO internal magnetism is the cause of this reduction. SRO may then be affecting the overall magnetism in the system in one of two ways. It is possible that a strong AFM interlayer coupling exists between the LCMO and SRO layers, and as the temperature is lowered below 136K, the SRO moments begin to align antiferromagnetically with the already present LCMO moments. AFM interlayer coupling has been observed in LSMO-SRO heterostructures, and is typically associated with an EB behavior in the films[64, 121]. We know from Chapter 4 that the 3uc buffered film has no EB present, but it remains to be seen if that effect would be enhanced by a greater SRO thickness. A second case may also explain these observed results however. It is possible that the SRO and LCMO layers have a weak FM or AFM coupling between above-T_c local domains in SRO and the interfacial Mn moments. These local domains pin the Mn moments IP and allow them to form at high T_c, as posited in Chapter 3, but as the thick films reach the SRO transition temperature, the magnetocrystaline anisotropy of the SRO magnetism becomes larger than the exchange coupling energy. As the temperature is reduced, more SRO moments are forced OOP and no longer induce the IP LCMO moments. This thickness of LCMO is nonmagnetic on its own, which is why at low temperatures there are no IP magnetic moments observed for the 20uc SRO film. In this case then, the exchange coupling is small compared to the magnetocrystalline anisotropy of SRO. The competition of these two terms can be elucidated by looking at the OOP M(T) data for the curves in Figure 4.4b). This shows that the OOP signal is still substantially suppressed for the 10uc SRO film, where a monolithic SRO film of this same

thickness would have a large OOP moment. The 10 unit cells of SRO are still dominated by an interfacial interaction with LCMO that forces the SRO moments IP, indicating that a strong exchange coupling exists in the system. Knowing that an IP reversal exists in the absence of a robust OOP moment in the 10uc buffered film, we consider this strong evidence of an interfacial antiparallel spin alignment. The 20uc buffered film does have a robust OOP moment at the same temperature as the downturn begins in the IP measurement, further showing that it is the SRO OOP magnetic onset that induces the IP reversal. There is another magnetic inflection point at 112K that may be related to structural changes in the SRO layers that will be discussed in this chapter.

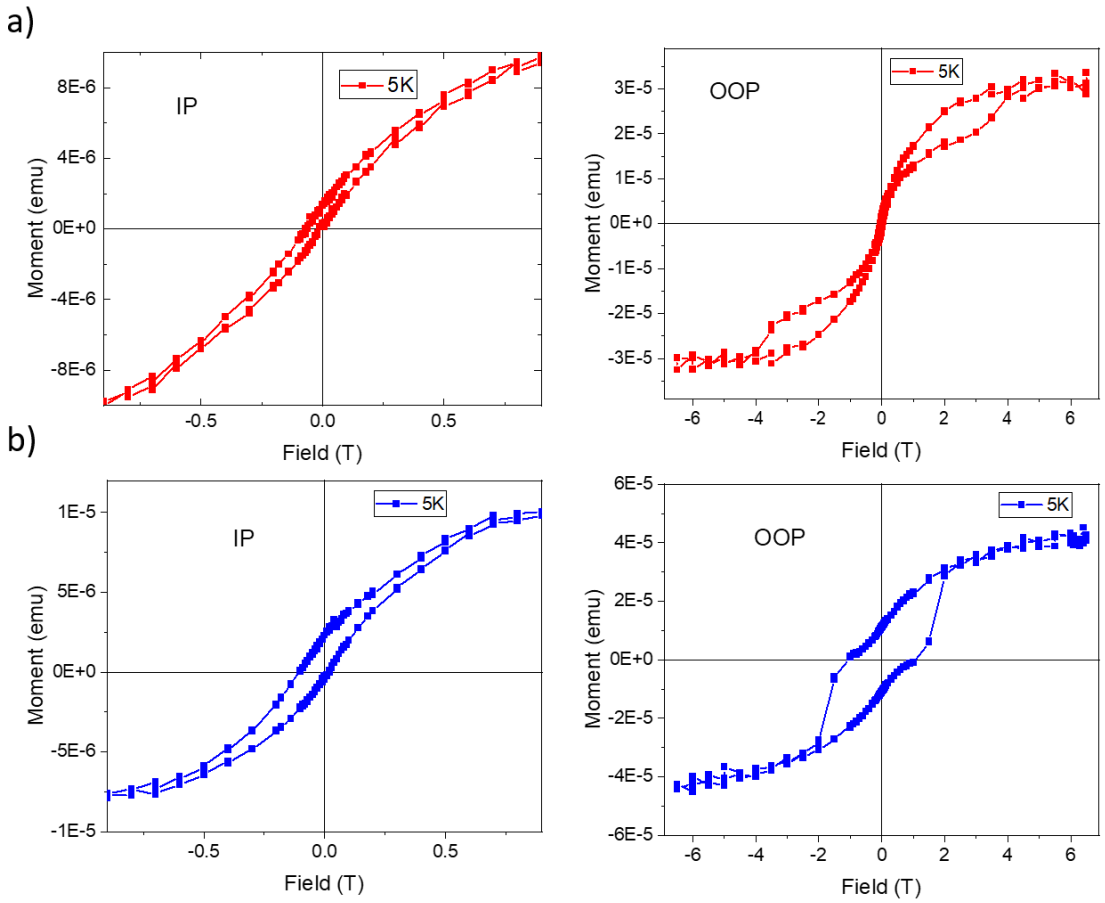

Figure 4.5. M(H) data at 5K from SQUID for IP, OOP arrangements of a) $LCMO^{4uc}/SRO^{10uc}/LCMO^{4uc}$ trilayer and b) $LCMO^{4uc}/SRO^{20uc}/LCMO^{4uc}$ trilayer. Films were cooled at 100 Oe.

Deciphering the exact interfacial mechanism at work entails looking to the magnetic hysteresis data for signs of any exchange biasing effects. We show the 5K M(H) measurements for the above mentioned SRO thickness films in Figure 4.5. Each of these films was cooled in only 100 Oe external fields, which places them in the "low field cooled" category. This is important as the direction of exchange bias has been linked to the applied field magnitude during cooling past the blocking temperature [140–142]. Low field cooled samples with interfacial AFM moments tend to exhibit negative exchange bias due to the interfacial coupling strength exceeding the applied field energy, allowing the AFM layers to preferentially align opposite to the applied field and increasing the field energy needed to form the Neel wall with the AFM layers. Positive exchange bias can emerge when the large applied cooling field forces all interfacial moments including in the AFM layer to align with it. Our thick SRO sample show a moderate introduction of a IP negative EB effect emerge with a -450 Oe and -400 Oe EB in the 10 and 20uc SRO trilayers, respectively. Coercive fields are on a similar scale IP with 500 Oe and 600 Oe respectively. This degree of EB is comparable to that observed in other low field cooled manganite heterostructures and is significant. It is also noteworthy that in the OOP orientation, no exchange bias behavior is seen in either thick film. This is due to a lack of LCMO FM moments oriented in the OOP direction as shown from M(T) data, and is further proof that an FM-AFM IP alignment of moments at the interface. In the previous paragraph, we said that the turndown behavior in M(T) could either be due to a AFM alignment of SRO spins IP with the LCMO moments, or be due to a breaking of the IP moments all together due to SRO's large magnetic anisotropy. The existence of exchange bias in these films is strong evidence for a persistent IP LCMO ferromagnetism coupled to AFM IP aligned SRO moments, as this FM/AFM interface is necessary for EB formation. A strong negative interfacial J_{ex} exists here that pins IP moments near the interface and creates the EB and M(T)

reversal behavior. It is important to note that no EB behavior exists in the ultrathin SRO case, and yet this sample still has an enhanced FM T_c above that of the thicker films. It may be that the AFM exchange coupling at the Mn-O-Ru bond exists in all samples and is enough to pin LCMO moments IP, but the SRO moments are much lower than those in LCMO and not significant enough for appreciable detection. This may also have to do with the increased magnetocrystalline anisotropy in thicker SRO layers, as changes in this parameter can alter the EB effect[143]. Why this exchange coupling exists remains to be seen, as most previous study has posited an interfacial charge transfer as the most likely cause of this behavior. We did not observe any charge transfer in our $LCMO^{4uc}/SRO^{3uc}/LCMO^{4uc}$ heterostructure in Chapter 3 however, and as the T_c enhancement effect is still present in this sample, this cause seems less likely. We also note the interesting shapes of the OOP hysteresis loops. For the 10uc SRO film, there are 3 separate hysteresis regions that have been seen in other manganite/ruthenate heterostructures[144]. The low field region is very small and would correlate to any components of LCMO that may have a slight OOP orientation. As we do not see large moments OOP from M(T) for this sample, it is then expected that the coercivity is nearly zero in this region. The large field regions are separated due to the still dominating role of IP LCMO moments and SRO coupling to them, requiring a large OOP field in order to align any of the SRO moments OOP. In the 20uc trilayer, the these regions merge into a single hysteresis loop with extremely large coercivity around 1T. The abrupt change is due to a merging of the previously separated regions seen in the 10uc buffered film and represents an SRO dominant OOP sample.

We look at the resistive properties of the $LCMO^{4uc}/SRO^{20uc}/LCMO^{4uc}$ film in Figure 4.6 as its properties are most different from the ultrathin case. As might be expected, the film is completely metallic across all measured temperatures up to 300K, with a slight inflection point near the low temperature onset of SRO magnetism. This inflection is typical of SRO films on STO substrates, and also has a low negative MR ratio under 2.5% near this transition that is again typical of SRO dominated films. This shows us that the resistive properties of this film are completely dominated by the SRO layers. The fact that no inflection is observed near the LCMO transition temperature, where metallic LCMO would have a CMR effect, is surprising, and is further evidence of a lack of DE-like behavior in these ultrathin LCMO layers even when the films as a whole are metallic. We would also expect charge transfer to be enhanced in metallic samples and push the LCMO layers into a more DE-like CMR behavior, but as this is not observed we further discount charge transfer's role in these systems.

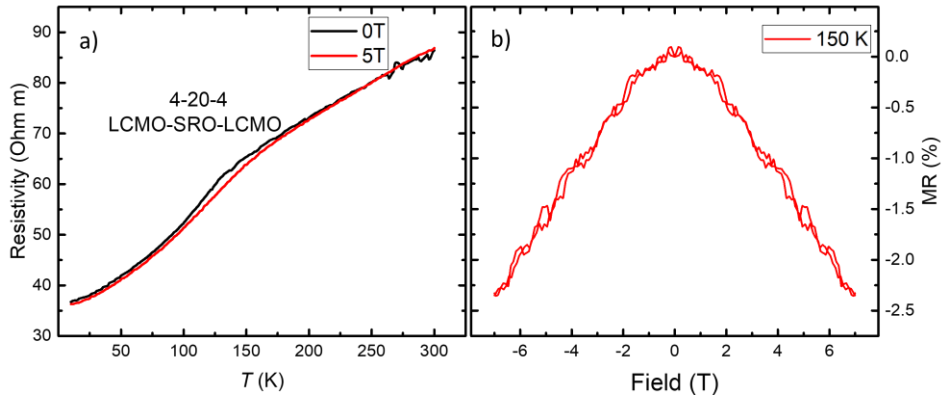

Figure 4.6. a) R(T) data, both at zero field and 5T, and b) R(H) at 150K for $LCMO^{40uc}/SRO^{40uc}/LCMO^{40uc}$ trilayer.

4.3. Structural Change in Thick Trilayers

Increasing the thickness of SRO in ultrathin LCMO heterostructures showed us a clear interfacial AFM exchange coupling between the two materials. The LCMO layers are extremely thin in films however, and not magnetic without this interfacial coupling. We became interested in how the internal robust magnetism of thicker film layers may interact with the interfacial region's exchange coupling, and set about studying the magnetic properties of the $LCMO^{40uc}/SRO^{40uc}/LCMO^{40uc}$ trilayer mentioned previously for our XRD work. Figure 4.7 shows the SQUID data for this trilayer both for the IP and OOP directions. We can see that this sample has an increased T_c of 250K, over that of monolithic films of this thickness. As expected, the IP moment is much larger than the OOP moment due to the 2.1 LCMO.SRO ratio and relative strength of Mn moments. Zooming in to the OOP M(T) data in Figure 4.7b) we see a downturn behavior emerge at 143K near the SRO onset temperature, similar to what was seen in the IP data for the $LCMO^{4uc}/SRO^{10uc}/LCMO^{4uc}$ film. The fact that this behavior now emerges in the OOP direction is most likely due to a small OOP canting of LCMO IP moments. If we take the LCMO magnetization at 150K (before SRO moments turn on) from the IP and OOP graphs and calculate the angle of the net magnetization we get an OOP canting angle of 4.12°. This naïve calculation is in line with that observed in our other films, for instance a $LCMO^{10uc}/SRO^{20uc}/LCMO^{10uc}$ trilayer

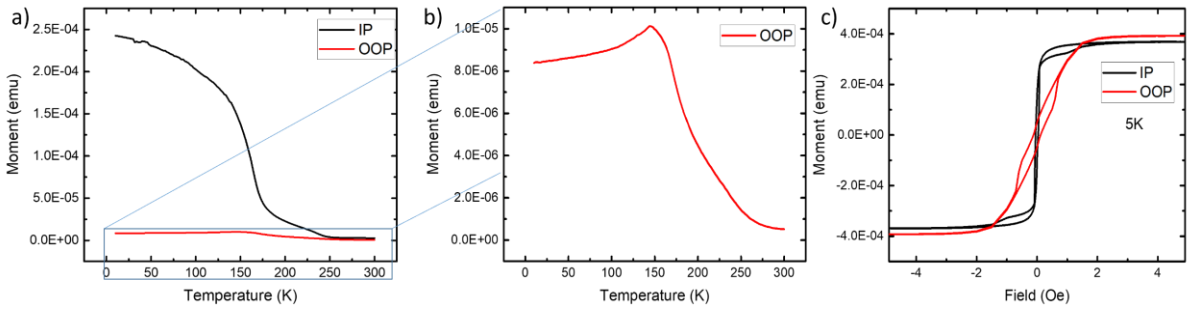

Figure 4.7. $LCMO^{40uc}/SRO^{40uc}/LCMO^{40uc}$ heterostructure M(T) and M(H) data. A) Large view of both IP and OOP components of magnetization, with b) showing a larger view of the OOP behavior. C) 5K 100 OE FC M(H) curves for both IP and OOP directed external fields.

we measured has a 4.81° OOP angle. Due to LCMO's apparent slight OOP alignment here, we attribute the downturn overserved OOP in the 40uc trilayer to the same AFM interfacial coupling seen in our other films. This downturn is present in both IP and OOP directions, meaning that the spins are perfectly AFM aligned. We note that the downturn is too small for 40uc of AFM aligned film, and attribute this to the strong IP character induced by interfacing with LCMO. We have seen in our other films that the IP component is dominant unless the SRO thickness is much more than that of LCMO, and this character is even more apparent in this sample. If the LCMO thickness is

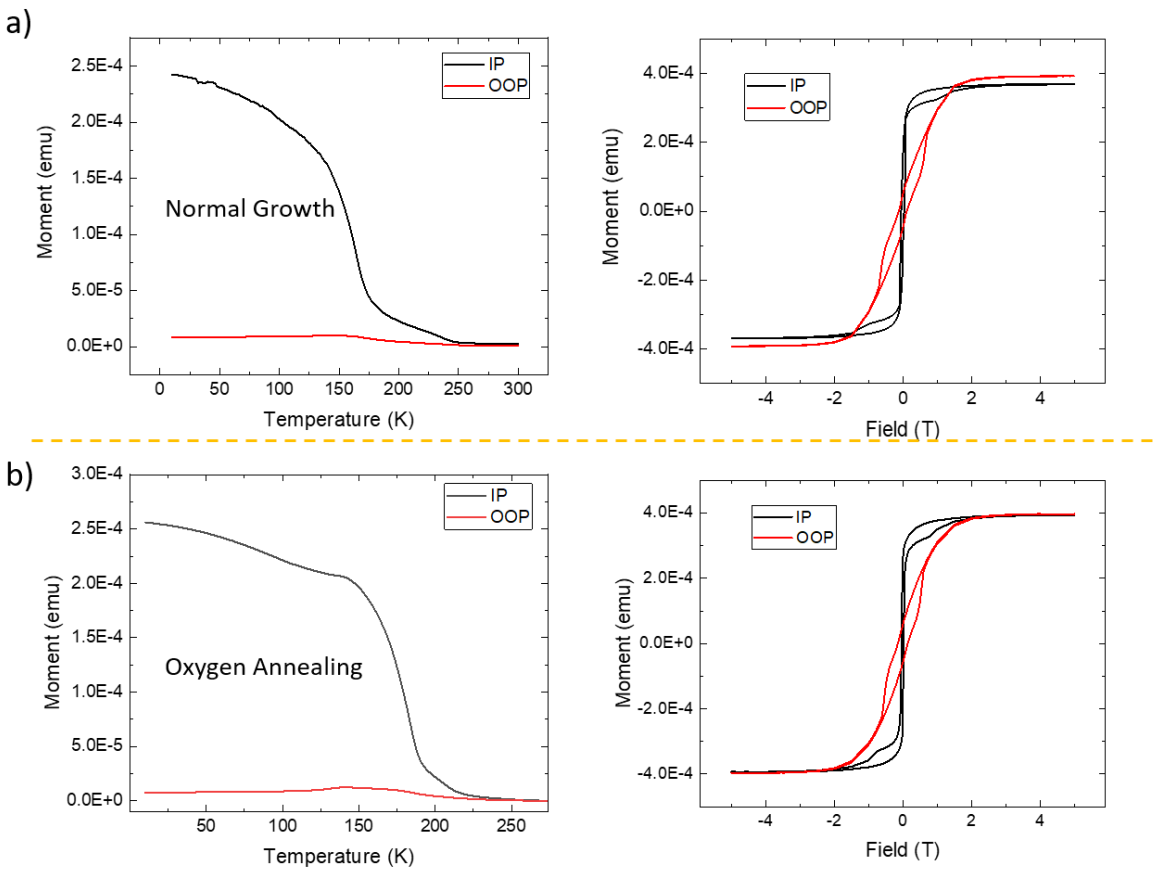

Figure 4.8. a) Data reproduced from Figure 4.7 for growth following the growth parameters used for all other films. B) SQUID data for oxygen annealed $LCMO^{40uc}/SRO^{40uc}/LCMO^{40uc}$ sample, where every 10uc during growth were annealed at 1torr oxygen pressure for 15 minutes.

too great, very few layers if any within the SRO buffer can break from the strong J_{ex} and most are only oriented at the same ~5 degree OOP angle as LCMO, albeit in an AFM alignment with those

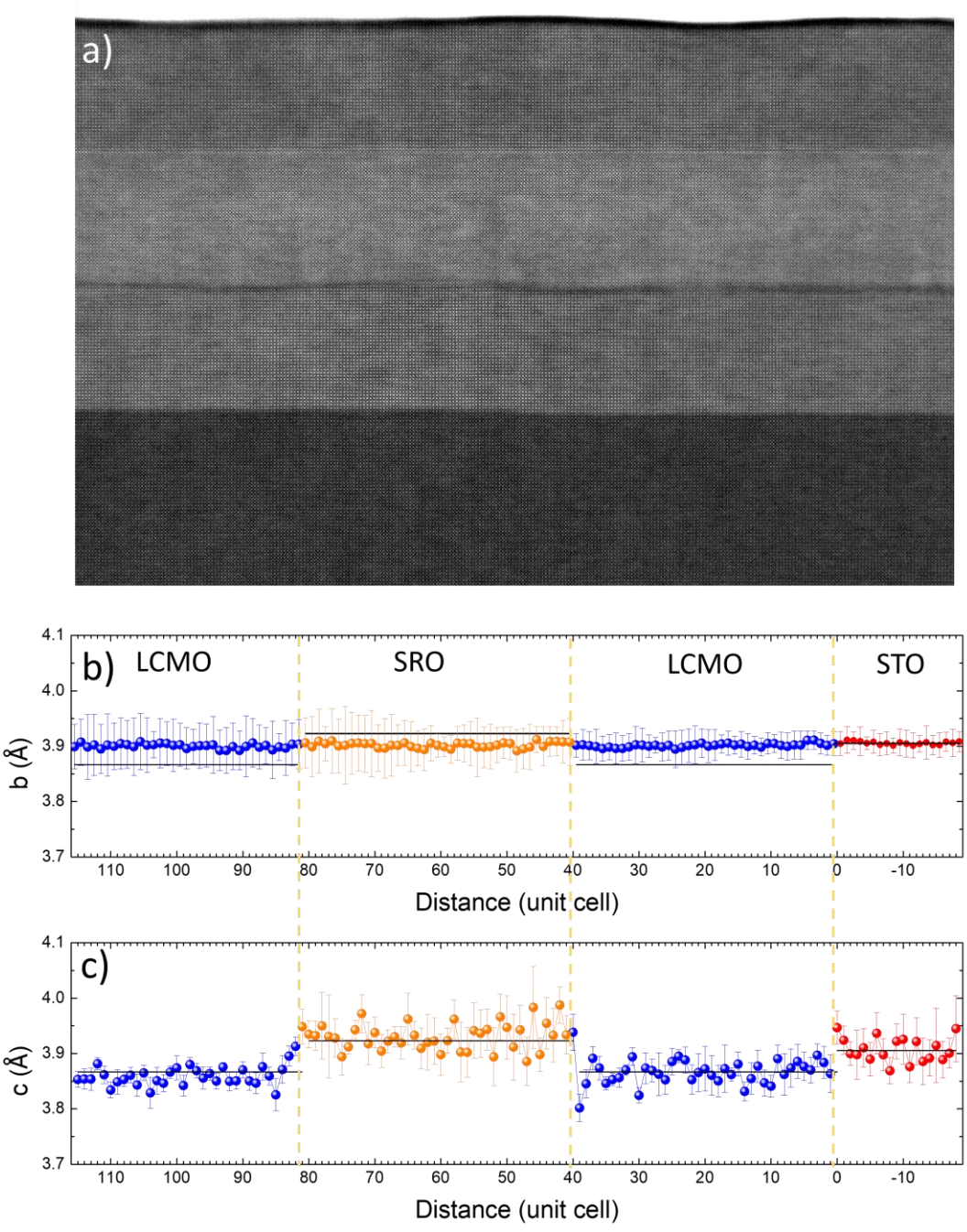

Figure 4.9. STEM HAADF image of large .1µm lateral area of $LCMO^{40uc}/SRO^{40uc}/LCMO^{40uc}$ trilayer. From this we can extract the b)IP and c)OOP pseudocubic lattice parameters for each film layer as an average over the given area. Black lines indicate the bulk lattice constants for each material layer.

Mn moments. This is why we see a moderate decrease in OOP moment below SRO T_c as opposed to an abrupt increase as would happen in monolithic SRO films.

In-plane M(T) data also shows an inflection point around 175K. Some studies of SRO films have shown that oxygen deficiency can alter the magnetic onset in films due to structural change [145]. To ensure that this was not occurring in our film, we used an oxygen annealing alternating growth cycle, using the same growth parameters to ensure the same quality crystal growth but pausing the growth every 10uc to anneal the sample at 1torr O_{pp} for 10 minutes in order ensure that every layer was oxygen rich. We compare the IP and OOP characteristics of both films in Figure 4.8, and can see that both films behave nearly identically, maintaining the two step T_c behavior. This may however be due to other structural effects not linked to oxygen vacancies, and this will be discussed. We can see from the magnetic hysteresis of this film that the IP magnetization has a split hysteresis while the OOP moment has a wasp-waist character. The IP behavior is further evidence of a substantial IP SRO orientation, as the field needed to orient the hard-axis SRO moments is split by the larger but lower coercivity LCMO moments. EB behavior is almost nonexistent, with a small IP EB of 100 Oe. For EB behavior to occur, a minimum cooling field must be used in order to train the sample in a given direction, and it is likely that the 100 Oe field used during cooling was not sufficient to align the SRO moments in any meaningful way. The slight EB field seen is the same magnitude of the cooling field, which may be an indication of an appreciable exchange bias behavior.

This large $LCMO^{40uc}/SRO^{40uc}/LCMO^{40uc}$ trilayer is intriguing in that it has robust AFM aligning states seemingly throughout the SRO buffer layer. We wanted to know if this could perhaps be structurally mediated, and performed STEM analysis on the sample. Figure 4.9 shows a large scale (~.1μm lateral area) HAADF image in the $(001)_{pc}$ direction of the 40uc sample, as

well as the layer averaged IP and OOP lattice parameters. LCMO interfaces are slightly "wavey", which may be due to some intermixture at the lower LCMO-SRO interface. However, the top SRO-LCMO interface is extremely sharp here, with no defects and single RuO_2 termination. As

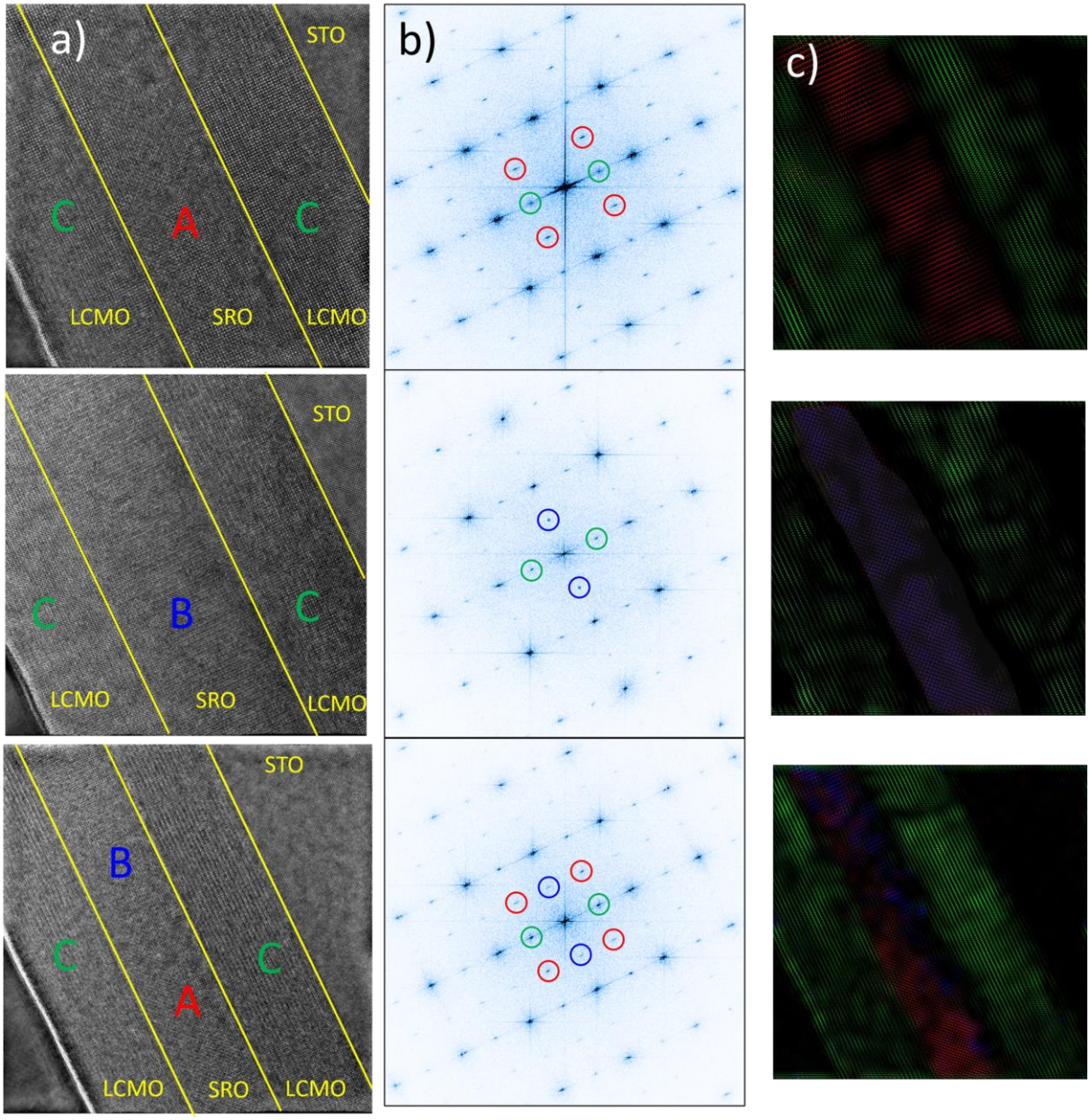

Figure 4.10. a) ABF and b) FFT diffraction patterns from 3 different large lateral areas. Yellow lines denote material interfaces. Red, blue, and green circles highlight diffraction spots for different structural domains A,B, and C formed. Two domains form in SRO buffer layers, and can be atomically mapped and colorized as shown in c), corresponding to the same colors used in b).

was discussed in Chapter 4, a stable RuO_2 terminated surface is abnormal even in extremely thin SRO films, and yet here after 40uc the SRO interface has still not converted to a SrO layer. Interfacial intermixture does not seem to be present here either, meaning that the top SrO layer is not being forced into the first LCMO layer as was suggested in Chapter 4. This affect has been observed in other manganite-SRO heterostructures, and may simply be due to growing on a tilted orthorhombic surface or a difference in growth parameters between studies, but this effect has yet to be rigorously studied and needs further work [115, 146]. The IP lattice constants in Figure 4.9b) show that the film remains strained to the substrate IP constant, in good agreement with our

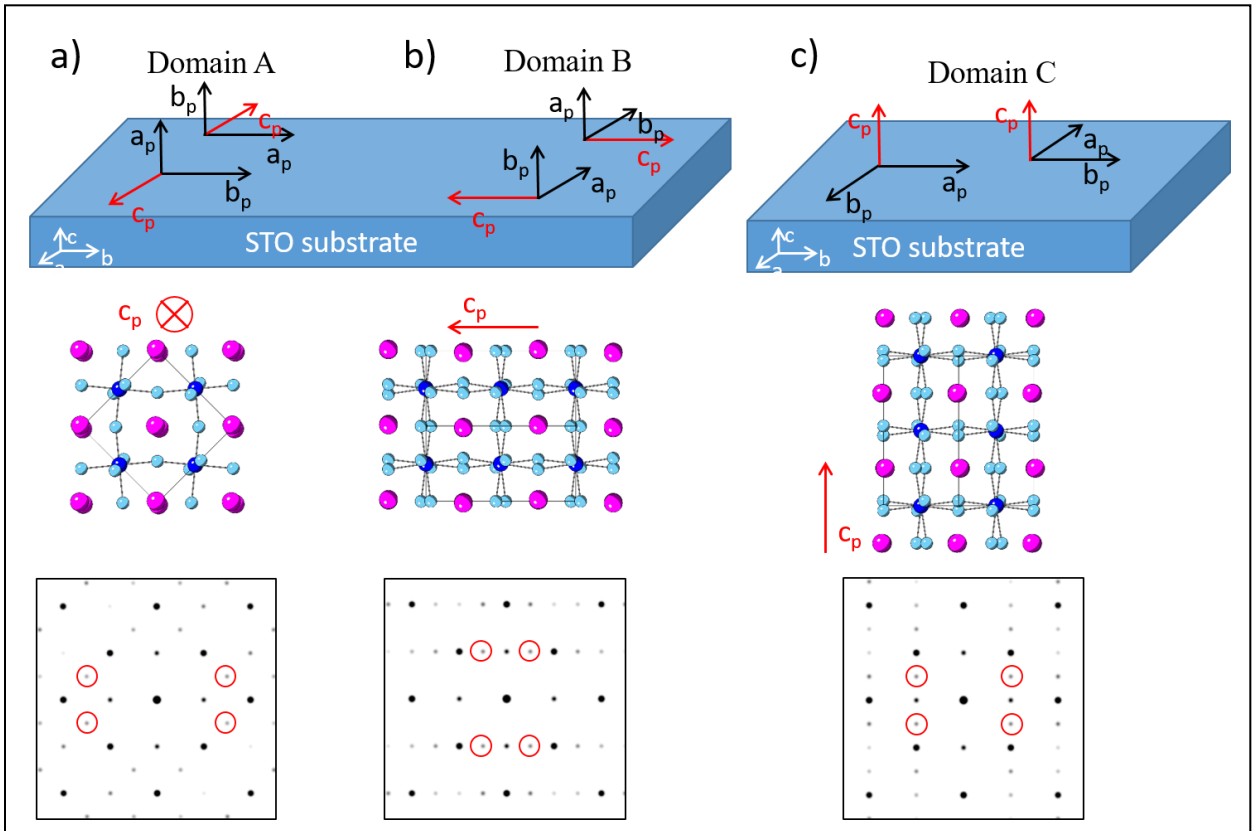

Figure 4.11. Schematic of different potential lattice orientations and their simulated FFT diffraction patterns. a), b) and c) correspond to the A,B,C domains. A,B domains form in SRO buffer layers, C domain forms in LCMO layers, which was observed for all films in the ultrathin cases (Chapter 3).

previous XRD data. Along the OOP axis, each material tends to return to their respective bulk-like constants (black lines in each region) fairly quickly away from interfacial layers.

We also obtained ABF images for different areas alongside FFT's of the imaged areas, and these are shown in Figure 4.10. A distinct structural change is observed in these films between the LCMO and SRO layers. In our $LCMO^{4uc}/SRO^{3uc}/LCMO^{4uc}$ HAADF imaging in Chapter 4 we saw that the entire film was symmetrically aligned and followed the same tilt-reduced pattern. Here however we see a distinct characteristic change between both the LCMO and SRO layers, as well as lateral differences between different sections of the film. To understand these differences, we show a schematic of the different possible structural domains herein in Figure 4.11, where the c (red) axis is the in-phase rotated crystal direction while the a and b axes (black) represent the equivalent out-of-phase rotated axes. When an orthorhombic material is grown on a cubic substrate, it will grow in one of three possible crystal orientations corresponding to which of the three axis is oriented OOP. Each of the three potential growth directions produces a different diffraction pattern that can be observed through ABF-FFT analysis. FFT intensity profile analysis for a given imaged area makes it possible to reverse engineer the locations of the various structural domains producing a given pattern, and this is how the color contrasted images are produced in Figure 4.10c). These images show that the LCMO layers maintain a single structural character with the in-phase axis oriented OOP for both the top and bottom layers. SRO meanwhile can occupy one of two potential IP orientations of this out-of-phase axis. We have observed this in other SRO and CRO samples, and is attributed to the equivalency between the two out-of-phase axes with the same pseudocubic lattice constants. The diffraction FFT images show the overall symmetry of a given section, and we can see that while some SRO sections remain fully in either structure A or B, there are some transition regions between these sections as shown in Figure

4.10b). In such crossover regions, we observe each intermediate spot, shown by the different colors circles depicting which colorized image section these diffraction spots correspond to. We note than in the previously STEM-studied SRO sample from Chapter 4, FFT analysis showed that the small SRO buffer layer matched the LCMO layer symmetric orientation, meaning that the entire film occupied a C structure as described here. Each film does however have a T_c enhancement effect, and it is therefore unlikely that relative orientation of the SRO lattice is primarily responsible for onset revival. The emergence of the A and B structural domains may however be necessary to setup the hard axis OOP orientation of SRO moments in these films and be linked to the downturn AFM effect seen in our magnetization data.

4.4. LCMO Thickness Variation

In the past section, we varied the thickness of the SRO buffer layer to understand how the increased anisotropy introduced by SRO might affect the magnetic properties observed in the previously dominant LCMO. Here we return to LCMO dominated films and allow them to move away from the ultrathin regime closer to their independent layer critical thickness. Doing this allows us to observe how the ultrathin 3uc buffer layers SRO, CRO and STO might affect the incipient FM layers of LCMO. We find that SRO continues to enhance T_c above that seen in other buffered films, though they seem to reach a maximum value around 225K. The saturation moment from STO buffered samples rapidly increases with LCMO increasing thickness and is likely related to oxygen octahedral rotation. Metallic behavior begins to remerge in SRO buffered trilayers above 6uc LCMO thickness alongside the reemergence of more bulk-like MR characteristics. Metallicity

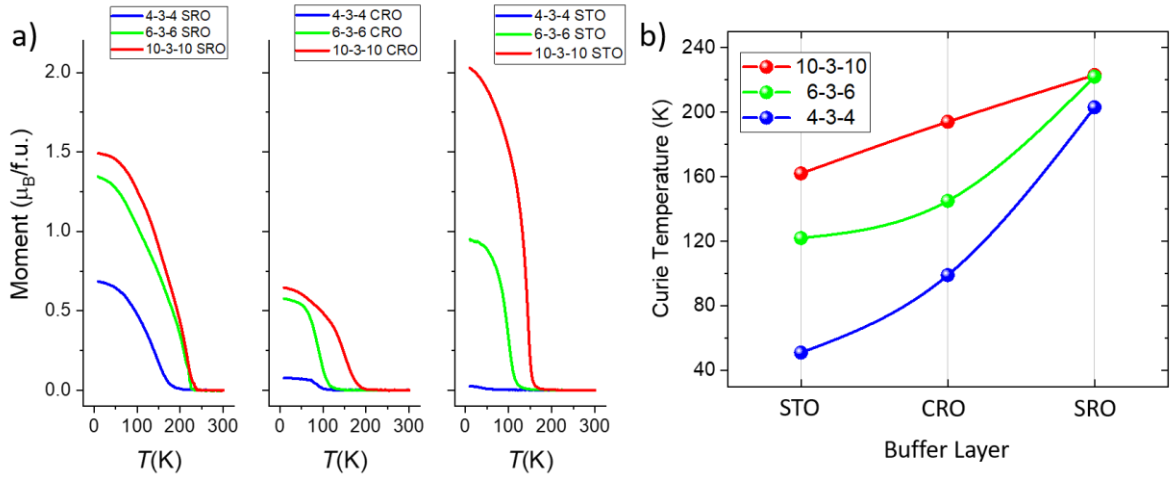

Figure 4.12. a) M(T) data for SRO, CRO, and STO buffered trilayers with 4 (blue),6 (green) , and 10uc (red) of LCMO surrounding layers. The magnetic onset temperatures for each thickness are plotted in b).

in these samples seems to allow for novel weak antilocalization (WAL) effects to emerge, appearing below the T_c of SRO. This points toward a strong spin-orbit coupling (SOC) effect in these samples mediated by LCMO layer metallicity, pointing again to a large exchange component between LCMO and SRO layers.

Beginning with IP magnetization data in Figure 4.12, we see that trilayers of the form $LCMO^{m=4,6,10uc}/Buffer^{3uc}/LCMO^{m=4,6,10uc}$ experience an increase in T_c as the thickness of LCMO is increased, as expected for films below the critical LCMO thickness. We chart the Tc's obtained from these M(T) plots in 4.12b) for each trilayer. SRO buffered films do maintain a higher onset temperature for each thickness, with CRO consistently exhibiting a moderate enhancement over STO buffered samples. We know that the interfacial Ru-Mn bond exerts an exchange coupling between the layers, and this is likely why both materials experience some enhancement effects even as the thickness increases. The SrO-MnO_2 interfacial layer terminations theoretically produce a larger coupling than the RuO_2-(LaCa)O termination, and as the CRO layer does not have any SrO interfacial layers, this may explain some of its exhibited lower T_c enhancement [66, 115].

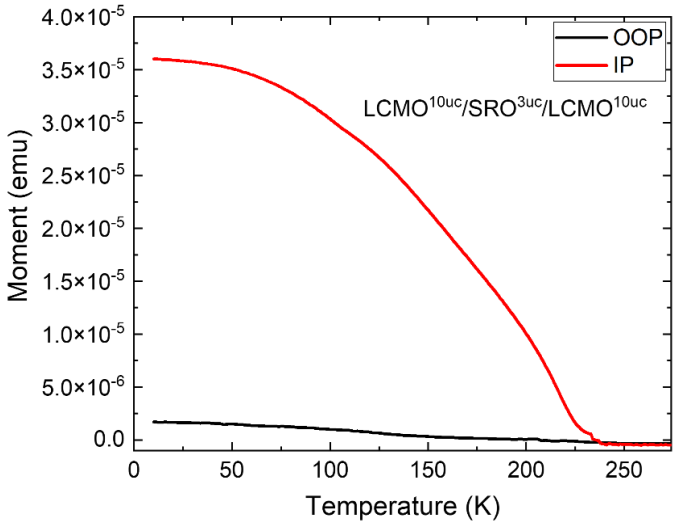

Figure 4.13. IP and OOP M(T) for $LCMO^{10uc}/SRO^{3uc}/LCMO^{10uc}$ trilayer film.

Onset in the STO buffered samples remains around the value for unbuffered monolithic films of the same LCMO layer thickness. We also wanted to look for any magnetic anisotropy in these thicker films and compare them with what was seen for our thick SRO buffered films. Figure 4.13 shows the IP and OOP magnetization data for our $LCMO^{10uc}/SRO^{3uc}/LCMO^{10uc}$ trilayer, as it is the closest in nominal thickness to our $LCMO^{4uc}/SRO^{20uc}/LCMO^{4uc}$ trilayer. We can see that these LCMO dominated films are IP aligned and have a relative LCMO moment alignment of .85° at 150K. This is evidence that it is only when the SRO structural and magnetic components become sufficiently large that any OOP alignment is induced in LCMO layers.

In our M(T) data, the STO buffered samples seemed to show a large increase in final magnetization compared to the ultrathin case. Exploring this effect, we show the IP magnetic hysteresis loops for each of the above discussed trilayers are shown in Figure 4.14, with their net saturation moments compiled in panel B. For the 6 and 10uc LCMO samples, we can see that the saturation moments for the STO buffered samples increases drastically, with the 10uc sample reaching 3.45 μ_B/Mn, exceeding the net magnetization of even the SRO buffered film and nearing

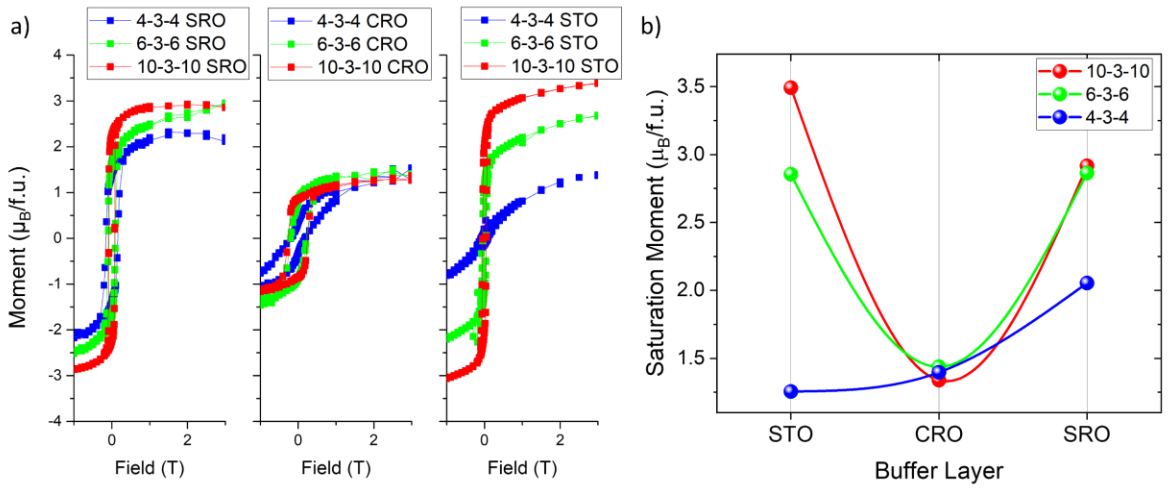

Figure 4.14. M(H) data for same samples in Figure 4.12. Saturation moment (taken at 3 T) are plotted in b).

the theoretical bulk 3.67 μ_B/Mn maximum. From M(T) data we know that the magnetic onset in this sample is 162K, around the 154K T_c of 10uc monolithic LCMO, meaning that this effect is not associated with any change in magnetic onset. Once the moments are formed however, they have a substantially increased IP uniformity, and we posit that this is due to structural modification of the LCMO films. From our TEM analysis in Chapter 4 we recall that the STO buffer layer tended to decrease the LCMO octahedral rotation. That sample was too thin however for the LCMO to be ferromagnetic on its own without the help of the interfacial Ru layers in the SRO sample, and did not show any saturation alteration. As the LCMO begins to be independently FM in the 6uc trilayer, the flattened bonds geometrically align the moments IP, and this effect continues for the 10uc trilayer. The DE ferromagnetic model also prefers a 180° bond alignment between hopping orbitals, and this flattening promotes an enhancement effect. This structural argument is consistent with what is seen in the CRO buffered sample, which has the lowest observed saturation moment that does not increase with LCMO thickness as it does in the other buffered films. CRO is known to have a large 8.5° bulk octahedral rotation, and this sample likely

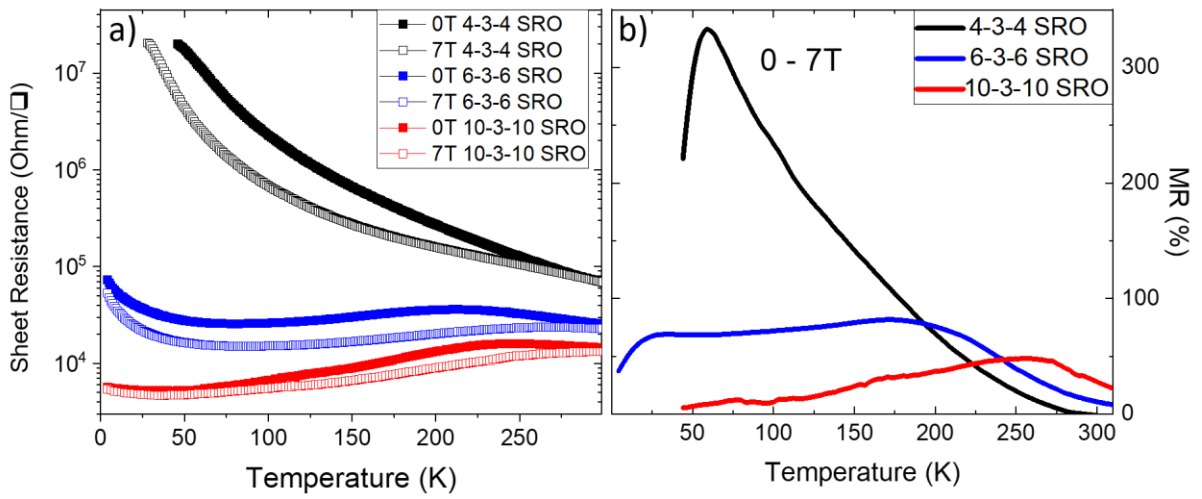

Figure 4.15. a) Field dependent R(T) data for SRO buffered films with different LCMO thickness. b) Calculated MR between the 0 and 7T R(T) values

has the greatest IP tilt of the three systems. Increasing the rotation decreases the uniform IP alignment and limits the maximum achievable saturation of the film[55, 147]. From this data, it seems that octahedral rotation in these manganite heterostructures primarily affects the maximum magnetization achievable and is not directly responsible for FM onset enhancement, as one can decouple the two enhancement phenomena.

We also examined the shape characteristics of the M(H) curves from Figure 4.14. The coercive fields are smallest for STO buffered samples and largest for CRO buffered samples across all LCMO thicknesses, an indication that saturation moment and magnetic hardness are inversely proportional here. CRO samples lose the two-step wasp waist behavior seen in the 4uc LCMO case, moving to a single hysteretic behavior for 6 and 10uc. This is likely due to much of the magnetism for thicker films not being near the interface any longer where CRO can create structural frustration that increases the field needed to flip an interfacial spin. We also do not observe any EB behavior in any of these films. As discussed, EB is only seen in samples with strong interfacial AFM coupling. We know however that the LCMO moments here strongly alter

SRO's magnetic anisotropy and pin its moments IP. As the LCMO layers become thicker, it is likely that they become even more dominant in the system and create a large internal field that flips the weak IP Ru moments at relatively low field into a FM alignment with LCMO. The absence of EB in the thick LCMO systems is not surprising then, given that it also does not exist in the ultrathin $LCMO^{4uc}/SRO^{3uc}/LCMO^{4uc}$ case.

As resistive changes in previous trilayers have illustrated key changes in the magnetic character of the films, we similarly investigate them here for the various LCMO thickness samples. We begin by looking solely at the SRO buffered cases in Figure 4.15. We can see a very clear change emerge moving from the 4 to 6uc LCMO sample, where a DE-like MIT emerges at 212 K, near the 222 K T_c for this sample. This trend continues for the 10uc LCMO trilayer, which shows a 246 K MIT slightly above it 223 K magnetic onset. The 7T resistivity data shows an apparently maximized MR ratio at the MIT transition temperature, with the temperature dependent ratio calculated in Figure 4.15b). For the thick LCMO systems, MR is maximized at the transition

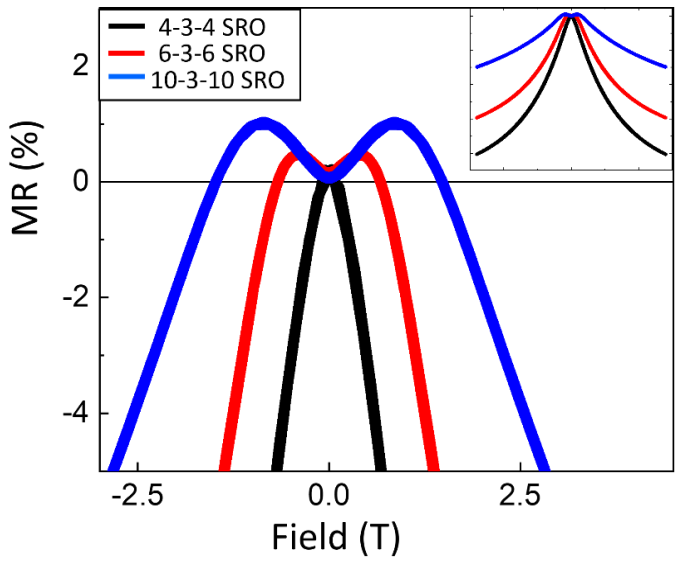

Figure 4.16. MR behavior of ultrathin SRO buffered trilayers with different LCMO thickness. Primary figure shows low-field region of larger MR curves (full curves shown in inset).

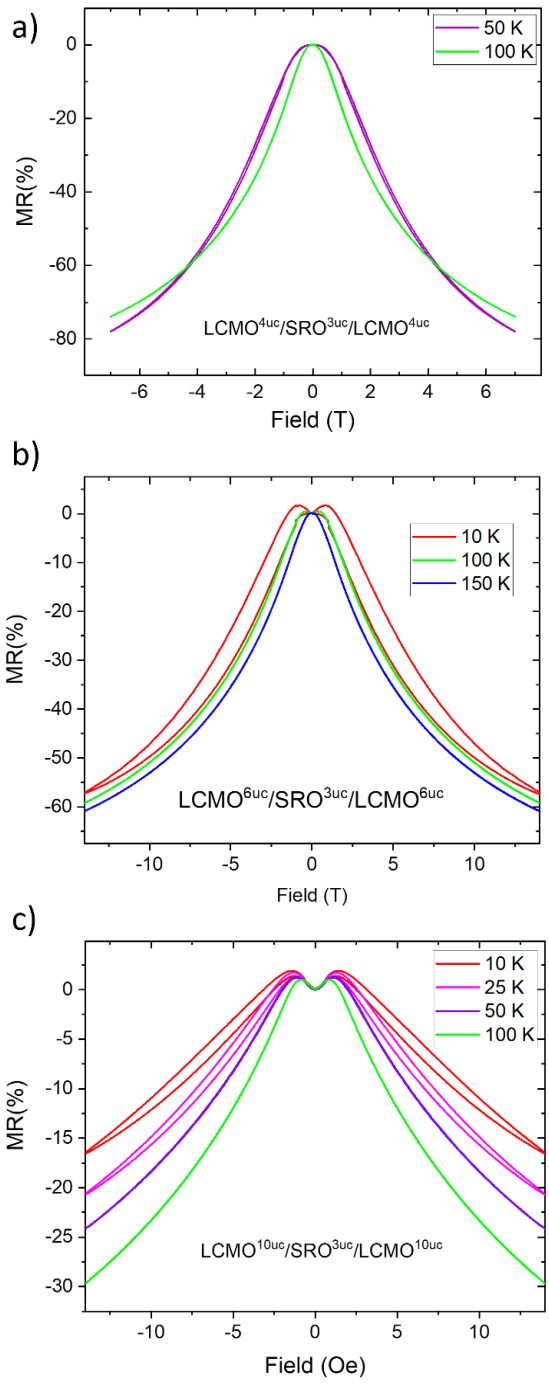

Figure 4.17. Temperature dependent MR for a)4uc, b)6uc, and c)10uc trilayer films buffered with 3uc of SRO. Measured temperatures range from 10-150K.

temperature, as is expected in DE systems. We assert then that these films have moved back to a DE mediated FM state. The thin 4uc trilayer case clearly occupies a different regime however,

with a perpetually increasing MR ratio and no MIT. We show then that while SRO buffering can move LCMO back into a FM metallic state prematurely, as 6uc monolithic LCMO is still fully insulating and nonmagnetic, the magnetic onset it not tied to this DE FM state. We posit that the induced FM alignment known to occur at the interface creates a homogeneous Mn eg spin state, which then lowers the energy needed for hopping and induces a DE-state at lower thicknesses than would otherwise exist. While structural considerations may also play a role, we know from Chapter 4 that each of these buffer layered films have a relatively similar lattice tilt and rotation, and we therefore must consider the induced magnetism itself as a cause for this change from insulating to metallic states.

Magnetoresistance measurements were also performed on these samples, and Figure 4.16 shows the 100 K R(H) measurements for each of the films, where the main figure is a close up of the near-zero field region of the inset's full 14T data. In the low-field region, we can see that the 4uc LCMO trilayer MR stays completely negative at all field values and has a relatively sharp peak. However, as the thickness of LCMO increases, a positive crossover behavior emerges, where at high fields we get a normal manganite closed loop negative resistive hysteresis, but at low fields a positive MR emerges before a near-zero field reduction in MR. This zero field "butterfly" effect is often ascribed to WAL, a quantum mechanical hopping effect seen in strong spin-orbit coupled materials. As the field is increased from zero, the metallic films experience a positive MR with maximums of .46 and 1.02% for the 6 and 10uc LCMO trilayers respectively. These maximums occur at .42 and .87T respectively, which are both far above the coercive fields observed for these samples. These are substantial effects, as other manganite/SRO heterostructures have reported similar crossover behavior below .25% positive MR [137]. It is noted that this MR behavior occurs as the thickness of SRO, the presumptively strong SOC material, is kept at the same thickness

while the LCMO thickness is varied and the sample becomes metallic, and was not observed in the increased SRO thickness samples.

Looking at multiple temperatures for the samples, we can see in Figure 4.17 the positive crossover effect persists for the thick samples for all temperatures below 100K, with maximum positive MR ratios of 2.3% and 1.9% for the 6 and 10uc films respectively. Resistive hysteresis also begins to emerge as the temperature is lowered below 25K for both samples, and the gap persists for both positive and negative MR regimes out to incredibly high fields, only barely closing at 14T for some temperatures. We note in the 6uc film data that we do not observe any positive MR crossover at 150K, a temperature just slightly above the SRO transition temperature in ultrathin layers. We also call to mind that 150K is well below the coincident MIT-FM onset in these thick LCMO trilayers, meaning that an onset of metallicity is not the cause of this effect. This is borne out by the fact that even in the fully insulating 4uc LCMO sample, at 50K we do see a very small hysteresis emerge with a 1000 Oe gap at 25% MR. This is comparable to the 1600 Oe coercive field from the M(H) curve for this sample, and the effect can be observed out to fields around 5T. Taken together, we can draw a few conclusions from these facts. As the crossover and hysteretic behavior only exists below the T_c of SRO, we assert that this effect only emerges when the SRO is independently magnetically ordered. As previously discussed, this alignment is AFM and has a strongly negative J_{ex}. Similar MR crossover and hysteretic behavior has been observed in SRO/manganite heterostructures with AFM alignment, and is typically understood as a competition between the Zeeman energy of the applied field and AFM exchange coupling near the interface [137, 148, 149]. As the thickness of the LCMO layers increases, layers away from the interface can increase the competition between these two and induce the crossover behavior. The hysteretic gaps are opened when the system does not provide enough thermal fluctuation energy

to aid the Zeeman field in flipping the interfacial AFM aligned moments. We do however observe that other SRO/manganite heterostructures with this interplay tend to close the hysteresis when the overall MR ratio returns to the negative regime, and that persistent gaps out to these fields and MRs are novel.

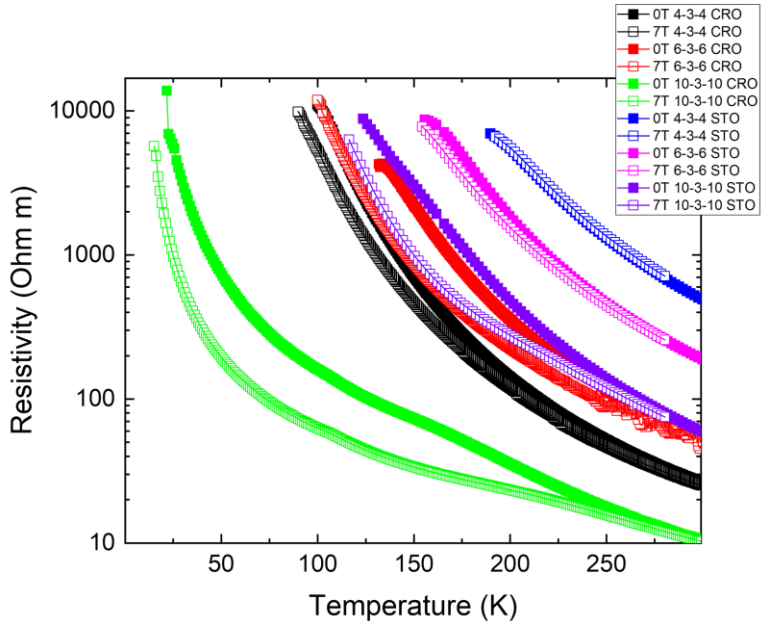

Figure 4.18. Field-dependent R(T) for CRO and STO buffered trilayers with 4,6, and 10uc LCMO thicknesses.

We briefly discuss the zero field and 7T R(T) behavior of the CRO and STO buffered films shown in Figure 4.18. Each film displays a fully insulating character across all temperatures, with no MIT even at 10uc LCMO thickness. We recall that the thicker films all have relatively high magnetic onset temperatures and, in the STO case, very high saturation magnetizations. SRO is the best metal of this group, and it is likely that it tends to drive the LCMO layers metallic before CRO or STO would. If metallicity is induced, either through buffering or an increased thickness, we then observe the MIT behavior and MR maximization at high temperature. These films are

further confirmation that metallicity and magnetism in LCMO are decoupled and that metallicity drives a specific type of magnetic character but is not needed for FM in this system.

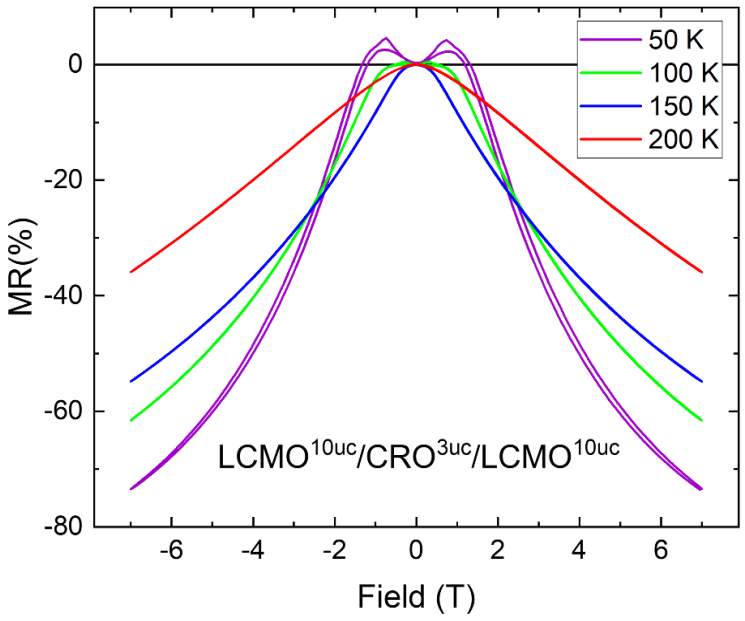

Figure 4.19. Temperature dependent MR for $LCMO^{10uc}/CRO^{3uc}/LCMO^{10uc}$ trilayer.

The $LCMO^{10uc}/CRO^{3uc}/LCMO^{10uc}$ heterostructure has a large magnetoresistance evident in the field-dependent R(T) data, and we therefore explore its MR behavior at different temperatures in Figure 4.19. We observe here a surprising result, where at 50 K a positive-to-negative crossover exists as well as a gapped hysteresis. This behavior is not seen in monolithic films, as was previously discussed, and suggests that the same interfacial Ru – O – Mn bond creates the same strong J_{ex} between the CRO and LCMO layers. In order for this interfacial coupling to have an effect on the MR however, there should be an AFM spin alignment at the interface that induces the initial positive MR that can then be brought negative by high-field alignment of spins. This means that in the 10uc thick LCMO sample, CRO has an induced FM that aligns itself antiparallel to the LCMO moments. It has been postulated that CRO is incipiently FM and that

structural change may be the only requisite for a slight FM behavior to emerge[150]. Structural change in the CRO case is likely imposed here by the thick LCMO layers from our previous STEM work, and we assume that this is important for FM inducement here. Still, the AFM alignment of any induced spins points toward a robust exchange coupling between layers that is not dependent on a SrO-MnO_2 interfacial bond, as only CaO-MnO_2 and (LaCa)O-RuO_2 interfaces exist in the CRO buffered sample. We also note that this sample is insulating at all temperature regimes, meaning that the MR crossover behavior can exist independent of a DE-mediated FM and is only dependent on the AFM alignment of interfacial spins. We speculate that this behavior only exists in thicker LCMO films as a result of higher internal fields produced by the increased number of Mn layers. These persistent FM moments can presumably pin the interfacial Ru moments in an AFM alignment if the exchange coupling is strong enough, thereby creating the positive MR effect observed. Thin LCMO layers do not have strong enough fields to induce this effect, which is why we observe a gradual increase of the MR crossover field and maximum positive MR achieved in the SRO buffered samples. As this is the only CRO buffered film which can be measured at low enough temperatures to observe any FM ordering in the CRO layer, this effect is not observed in the 6uc LCMO case.

4.5. Discussion and Conclusion

After looking at many thicknesses for both the LCMO layers and SRO buffer layers, as well as contrasting these effects with those seen in CRO and STO buffered samples, we can draw a few key insights into the nature of magnetism in these systems. Ferromagnetic onset in LCMO layers is clearly enhanced in SRO buffered samples more than in either CRO and STO buffered cases, and this enhancement occurs at temperatures far above any potential magnetic ordering in SRO. Indeed, we can clearly see the effects that do occur below the normal SRO transition

temperature. For thick SRO films, a downturn in the total magnetization occurs at the SRO T_c, and a clear IP exchange bias effect occurs at low temperature. We also see a clear MR crossover and hysteresis emerge in thick LCMO trilayers. Each of these effects has been directly linked to an AFM interfacial spin alignment and negative exchange coupling in other work on manganite/ruthenate heterostructures. Our results from this chapter confirm these previous findings across multiple thicknesses.

We importantly also find that the AFM interfacial coupling exists regardless of film thicknesses or metallicity. As both metallic and insulating trilayers have magnetic onset enhancement and the interfacial exchange coupling has been shown to produce various characteristics AFM alignment effects and be mediated pure by the interfacial moments, we therefore assert that a large negative J_{ex} between the LCMO and ruthenate layers is the main cause for the magnetic revival observed. We also show through CRO buffering and MR measurements that an interfacial AFM alignment can be formed despite CRO's lack of self-mediated magnetic ordering, showing the strength of the Mn-O-Ru exchange coupling. This only occurs when the LCMO thickness is great enough that moments formed in this layer

Structure also plays a crucial role in the observed phenomena. We observed multiple structural domains in the thick LCMO/SRO trilayer sample. This sample also had clearly observable kinks in M(T) curves, showing multiple magnetic transitions at high temperature. These kinks are also observed in the OOP M(T) for the $LCMO^{4uc}/SRO^{20uc}/LCMO^{4uc}$ trilayer but not in ultrathin trilayers. The ultrathin SRO trilayers were shown in Chapter 4 to occupy the same single structural domain as the LCMO layers surrounding it. As these M(T) kinks still exist in the during-growth annealed sample, we propose that structural ordering in SRO layers is the main cause of this kink behavior. In samples with thick SRO that can occupy the two domain structure

discussed, there is an initial onset in the LCMO layers mediated by the Ru-O-Mn exchange coupling and SRO's above-Tc magnetic domains. Because of SRO's large magnetic anisotropy, this magnetism is frustrated by the separate structures. As the temperature is lowered further however, the structural domains solidify into a single domain and allow for much easier alignment of moments, causing the second transition. This structural change is conjecture, however similar structural domain kink effects are known to exist in other manganites[151].

Oxygen octahedral rotation also plays a clear role in the maximum magnetization that a sample achieves. We can see that the saturation of independently FM LCMO layers is greatest for the sample that suppresses its tilt most, STO, and this saturation is decreased as the tilt is increased by buffering with SRO and then CRO. This effect is not tied to the pattern for magnetic onset temperatures and can be thought of independently. We also know from our monolithic data that 10uc of LCMO does not have this high of a saturation moment when grown on STO substrate, so it is not the STO/LCMO interface itself or any doping across it that is inducing this effect. It is clear from these facts that only the structural change induced by sandwiching the bottom LCMO layer between two flattening layers could induce this effect. This result is not unexpected under a superexchange model of FM which would predict easier magnetic alignment for larger overlapped Mn-O-Mn orbitals. The fact that this effect can be decoupled in these insulating samples from the magnetic onset temperature may allow for future research into how octahedral rotation can be utilized to increase the magnetic response in manganites.

In this chapter, we examined how varying the thickness of LCMO and SRO layers might alter the structural, magnetic, and insulating properties of the already established magnetically revived trilayer system. We found that thick SRO buffered samples display an AFM alignment onset at the SRO transition temperature, pointing toward an interfacial AFM coupling. This effect

persists in films with 40uc layers of both LCMO and SRO, which also show a switch from ultrathin single domain structures to exhibiting a two domain character in the SRO layers. Through holding a single thickness for the buffer layers and varying LCMO thickness, we showed that SRO continues to enhance the magnetic properties beyond that of other buffer materials, though the reduced tilt of STO samples can increase the magnetic saturation observed for those samples. The MR characteristics change drastically between the metallic and insulating SRO buffered samples, with DE-like CMR for the metallic samples while insulating samples continuously increase in MR with lower temperature. Positive crossover and large resistive hysteresis in thick samples points toward a strong AFM alignment between layers that is hard to overcome and perhaps enhanced by hard interfacial layers and easy LCMO top layers. We conclude from this chapter that a strong exchange coupling exists at manganite-ruthenate interfaces that induces magnetic revival in the system and is mediated by the interfacial termination, rotation angle, and magnetic order of the buffered material.

Chapter 5. Thickness Dependent Structural Defect Evolution in BTO – SIO Heterostructures

In addition to my extensive study of LCMO trilayered systems, I also investigated the structural evolution of a different system through heterostructuring high quality films of SrIrO3 (SIO) and BaTiO3 (BTO). This work was undertaken as a means of understanding how heterostructures may be affected by varying layer thickness and degrees of film strain, which is important for our other work in thickness dependent material characteristics. SIO is a material with extremely high spin-orbit coupling around .4eV due to Iridium's large Z and unpaired 5d electrons in the Ir^{4+} state [152, 153]. It has also been known to house interesting magnetic properties under heterointerfacing, with SRO superlattices showing tunable anisotropy and ultrathin STO spacing layers allowing for enhanced magnetism even down to a single unit cell[154–156]. The magnetic effects here are typically ascribed to an enhanced Dzyaloshinskii–Moriya interaction (DMI) at the interface as a result of broken inversion symmetry [154, 157]. BTO meanwhile has been shown to induce noncentrosymmetricity in films it is interfaced with, breaking a critical symmetry which can have pronounced magnetic and electronic effects [158].

5.1 Growth

Good crystalline growth of these materials on STO (001) substrates proved difficult. In their bulk, SIO and BTO have a pseudocubic IP lattice constant of 3.96 Å and 4.00 Å respectively [159, 160]. Growing on the substrate IP lattice constant of 3.905 Å in STO, the SIO film is under 1.5% compressive strain and the BTO is under 2.3%. Large strains are known to cause dislocation centers and substrate-film relaxation in perovskite heterostructures, and we see that for BTO films

---

This chapter contains previously published data from "Formation of dislocations via misfit strain across interfaces in epitaxial BaTiO3 and SrIrO3 heterostructures." Journal of Physics: Condensed Matter 33.27 (2021).

grown on STO(001), a large degree of relaxation could be observed in RSM plots. Figure 5.1 shows RHEED patterns and XRD data obtained for a representative 30 unit cell BTO thin film. These films were grown at 630° C and 5 mTorr oxygen environment (with a 2.5% O_3 concentration), and the ablation laser was pulsed at 2Hz with a 1.5 J/cm^2 energy density.

We can see from the RHEED spot evolution that the film moves into a step flow mode during growth, changing from the pristine substrate spots before to a streaky pattern. This is not necessarily indicative of any film relaxation or deformation, but can be associated with it in some cases. In XRD, the omega rocking curves show good alignment of the crystalline growth directions, and the coupled scans show some thickness fringes showing the OOP lattice parameter at 4.086 Å and confirming the 2.3% strain of the film. However, RSM around the (-103) off-

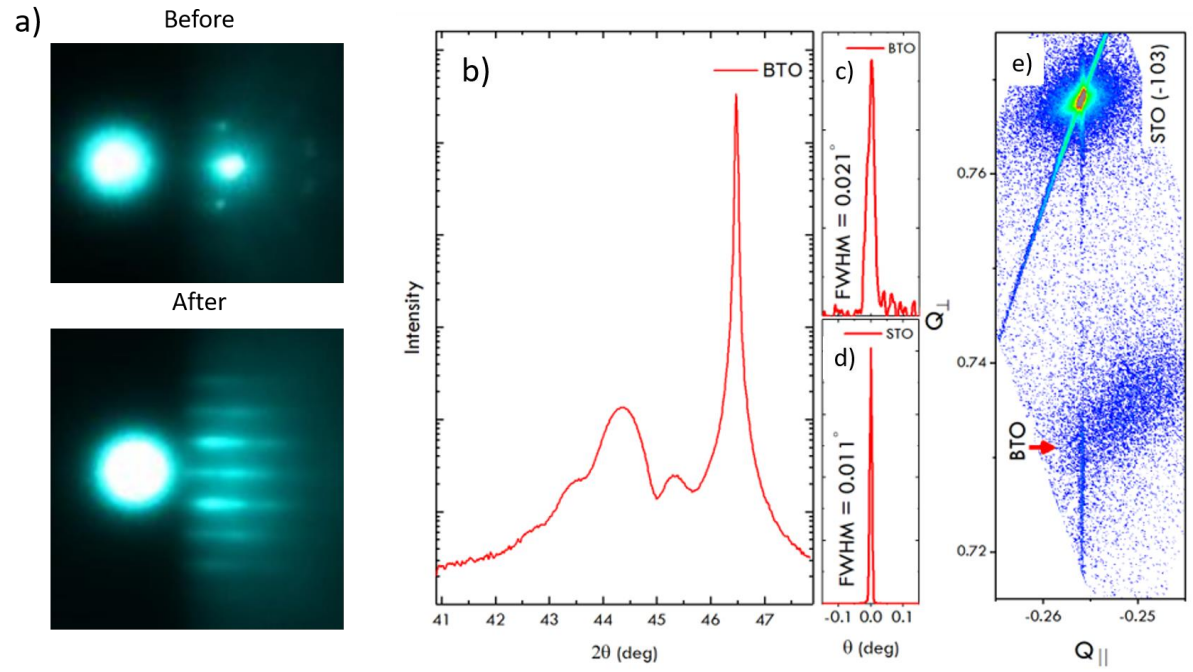

Figure 5.1. Structural data on 30 unit cell monolithic BTO film. a) RHEED patterns taken immediately before and after thin film growth. b) Omega- 2theta (coupled) scan around STO (002) diffraction peak. c-d) BTO film and STO substrate rocking curve scans show low mosaicity of film and substrate. e) RSM of (-103) asymmetric spot, with Q_{II} and $Q_{\perp}$ denoting the IP and OOP components respectively with units Å^{-1}.

symmetric point shows a spread in the BTO film peak, as evidenced by the lower count patch surrounding that labeled “BTO” higher count film peak. The majority of the film is strained to STO, but the RSM spreading denotes that parts of the film have become relaxed from the STO IP lattice constant. This halo is shifted toward the smaller OOP, larger IP direction from the film peak, denoting that the relaxed BTO is moving toward its bulk-like characteristics and reducing its compressive strain. The same relaxation is not seen in SIO monolithic films, as shown in Fig 5.2b-e), which have good rocking curve characteristics, multiple coupled scan thickness fringes (which denotes a more uniform OOP lattice constant in SIO than in the comparatively fewer seen in BTO coupled scans), and no appreciable RSM relaxation in the 45 unit cell monolayer. Growth parameters for this film were substantially different from BTO films, using a 180 mTorr oxygen environment, 720° C substrate temperature, and a 2 J/cm^2 laser repeating at 2Hz. RHEED patterns in Fig 5.2a) show that SIO film does maintain a layer-by-layer growth during deposition. The

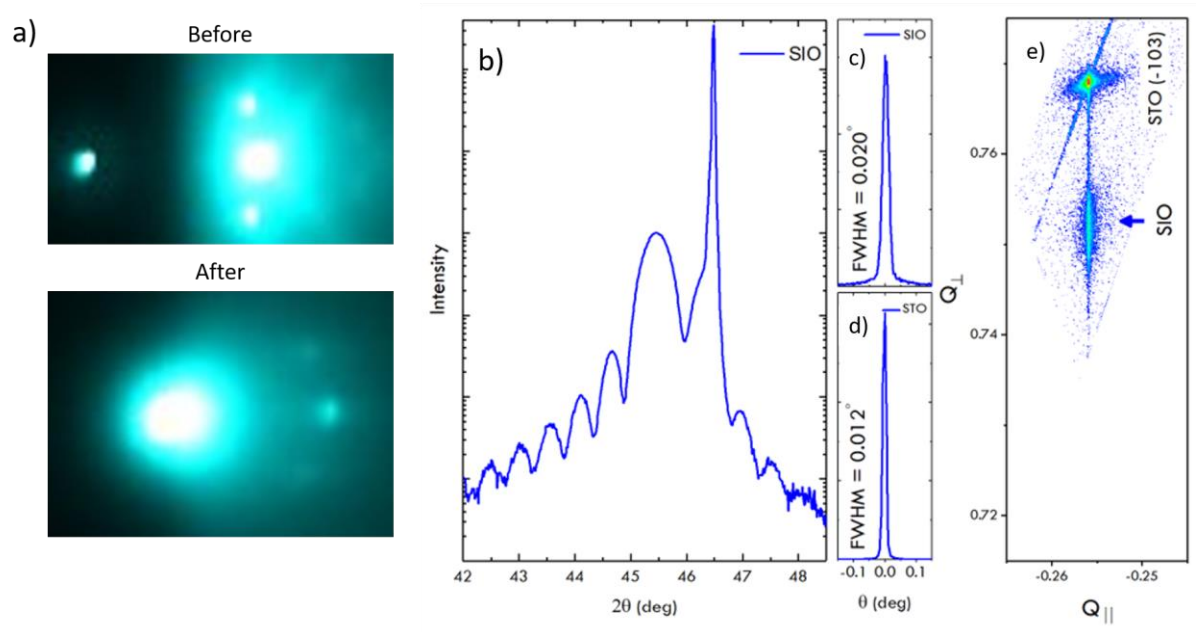

Figure 5.2. Structural data on 45 unit cell monolithic SIO film. a) RHEED patterns taken immediately before and after thin film growth. b) Omega- 2theta (coupled) scan around STO (002) diffraction peak. c-d) SIO film and STO substrate rocking curve scans. e) RSM of (-103) asymmetric spot showing full strain of the SIO film

reduced compressive strain in this material, as well as the centrosymmetricity of its perovskite unit cell, likely plays a role in why SIO grows in a more uniform fashion than BTO films.

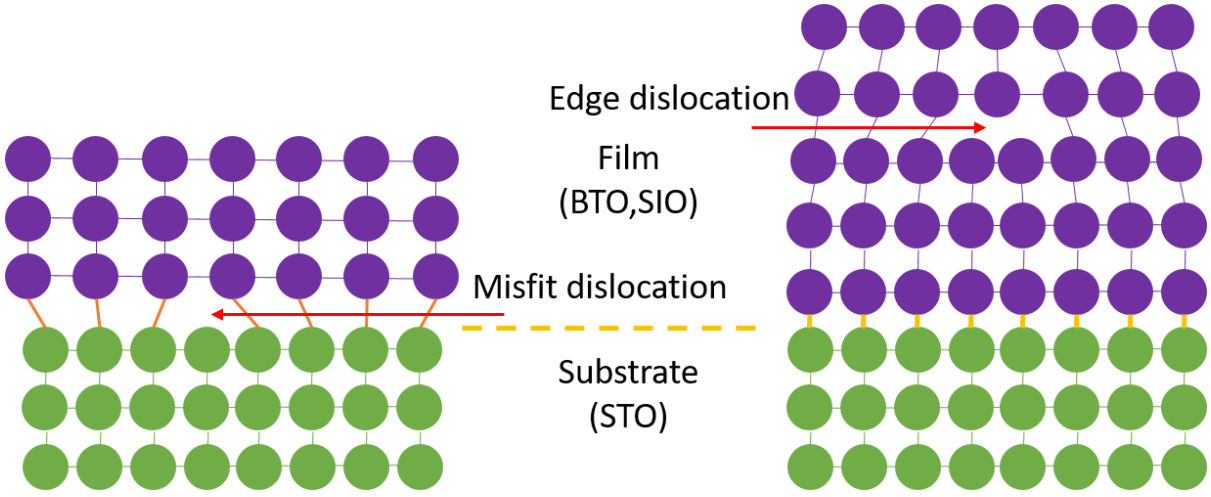

Figure 5.3. Toy model of different types of dislocation cores. Misfit dislocations occur at the interface between films and can provide for immediate film relaxation. Edge dislocations are a type of point defect within a film that can release elastic energy away from the interface.

Understanding the origins of the BTO relaxation in these films became the primary driver of this study, and through heterointerfacing between BTO and SIO we were able to elucidate the evolution of dislocation centers in strained epitaxial films. Dislocations are known to occur in films with large lattice mismatch, and can occur either as misfit dislocations at interfaces or half-loop dislocations within the films [161–165]. Misfit dislocations can occur acutely at the interface due to poor epitaxial conditions or be induced as the film strain field is increased through threading dislocations that penetrate to the interface. Edge dislocations, a form of half-loop dislocation, occur at points in the crystal that have either an additional or removed atom in the lattice. A schematic of misfit and edge dislocations are pictured in Figure 5.3. The Burgers vector associated with a dislocation describes the crystal direction shift needed to compensate for the change, and can have a magnitude greater than 1 if multiple crystal sites are involved in the dislocation described. These half-loop dislocations are intermediate sites within the films and only affect unit cells grown on

top of them. Growing thicker strained films increases the probability of these dislocation formations, as the strain field may not be enough in thinner films to drive nucleation of these sites. Mitigating oxygen vacancies is also effective in limiting dislocations, as these can serve as point defects that lower the cost of nucleation. Understanding how these dislocations evolve over heterointerfaces is crucial for development of defect engineered devices, yet little is known about their development across interfaces [166].

Toward this end, we grew heterostructures between highly-strained BTO and lightly-strained SIO on STO(001) and used XRD, STEM, and 4D in-plane (IP) strain mapping to investigate the films' crystalline properties and defect formation. Figure 5.4a) shows a schematic of a $BTO^{10uc}/SIO^{2uc}/BTO^{10uc}/SIO^{2uc}/BTO^{10uc}$ heterostructure grown on STO(001). The RHEED patterns before and after growth are shown in panel b), and show that this film again has

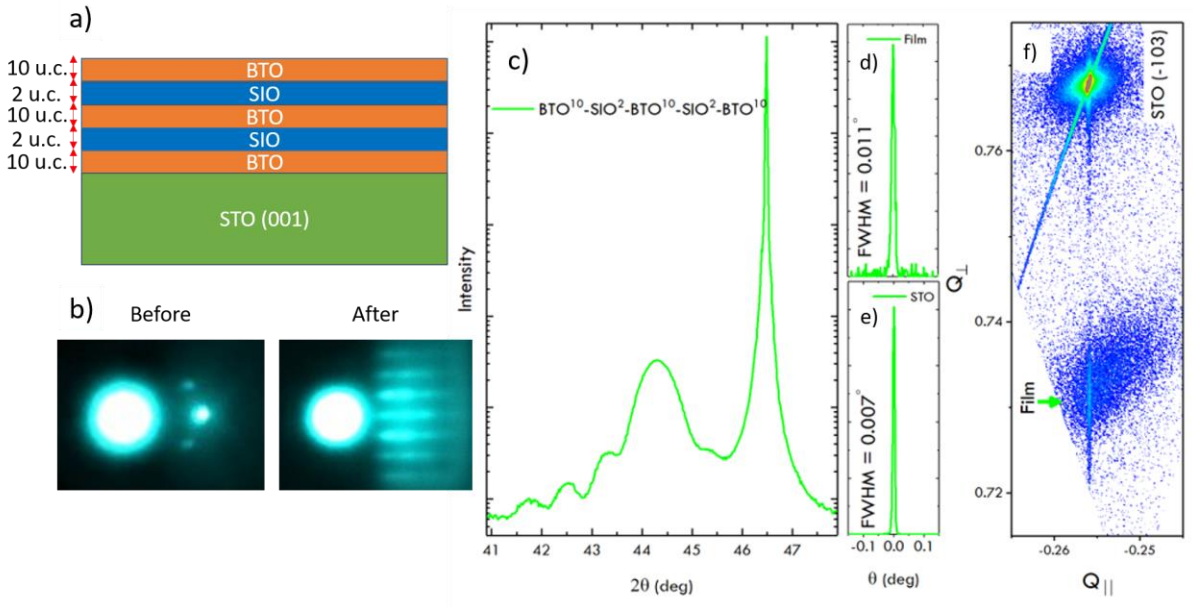

Figure 5.4. a) Schematic model of $BTO^{10uc}/SIO^{2uc}/BTO^{10uc}/SIO^{2uc}/BTO^{10uc}$ heterostructure to provide clarity on nomenclature used throughout chapter. b) Coupled scan around STO (002) diffraction peak. c-d) Film and STO substrate rocking curve scans. e) RSM of (-103) asymmetric spot partial film relaxation.

transitioned to a step-flow growth in a similar fashion to a monolithic BTO film. This film in particular was chosen to highlight the role of increasing the number of interfaces in a nominal thickness BTO film, and can be compared with the patterns observed in the 30 u.c. film from Figure 5.1. The fact that the SIO layers in this sample are kept comparably low in relation to the number of BTO layers isolates the affect of just the interface. We note here that, along with lattice mismatch strain, symmetry mismatch can also affect a heteroepitaxial growth. BTO has a cubic (albeit noncentrosymmetric) structure with a Glazer notation of $a^0a^0a^0$, which is the same as the STO substrate. SIO however is part of the *Pnma* crystallographic group with $a^-a^-c^+$ tilt and rotation pattern [92, 160]. This type of symmetry mismatch might also increase the likelihood of dislocation formation as the layers attempt to return to bulk symmetries. In this sample however, it is evident from the coupled scans and rocking curves shown in Fig 5.4c-e) that the two films have a similar crystalline quality with comparable behaviors in both. This similarity extends to the

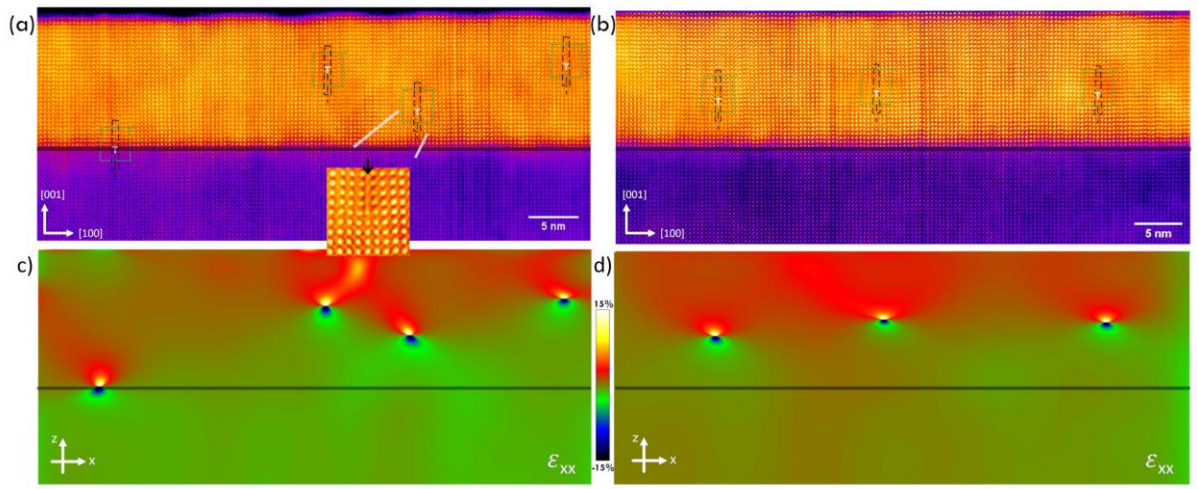

Figure 5.5. 4D STEM of monolithic BTO film. a-b) color contrasted HAADF images showing the interfacial quality and consistent thickness of the grown film. Dotted lines highlight the existence of dislocations formed. Inset shows closer view of a dislocation site, showing it to be an edge dislocation. Black line denotes substrate interface. c-d) ε_{xx} (IP) strain maps of same areas imaged in a-b. Shows transition from compressive (green) strain to tensile (red) strain after dislocation formation.

RSM of the (-103) spot, where both films produce a majority strained film peak encompassed by a relaxed lower count region. This is our first indication that increasing the number of interfaces in highly compressively strained oxide films does not increase film relaxation or dislocation formation, as both the monolithic films and increased interface films behave nearly identically in macroscopic XRD measurements.

5.2 STEM and Atomic Strain Maps of BTO Heterostructures

An atomic picture of the structural evolution across the films is needed to see how these dislocations are positioned within. HAADF images using STEM and corresponding IP strain maps were obtained for a selection of films that could efficiently encapsulate how both film thickness and interface density affected dislocation nucleation. Of primary importance as a baseline was our 30 u.c. monolithic BTO film, as shown in Figure 5.5. Large areas scans are shown and portray a consistent thickness across the film. We can immediately see from a-b) HAADF images that, apart from a single interfacial atomic displacement across the 118 nm scanned area, misfit dislocations are not forming at the interface between BTO and STO substrate. We do however begin to see edge dislocations as the thickness of the film increases, shown clearly from the zoomed inset of Fig 5.5a). At these sites, a single Ba atom is removed, allowing the larger lattice constant BTO to extend outward toward its preferred in-plane lattice constant. These sites occur conspicuously at similar thicknesses, with an average distance of 6.2 ± 1.7 nm from the STO interface. This thickness behavior has been seen in other BTO monolithic films on STO(001) and their location has been shown to be affected by growth temperature and oxygen annealing, but always tend to occur at thicknesses below 6nm [165, 167]. We use a lower growth temperature, which provides a lower energy environment during growth for dislocations to form and thus necessitates a higher

thickness of film to reach the dislocation nucleation energy, putting our dislocations further from the substrate than other works.

IP strain maps looking at the ε_{xx} matrix element of the 4D STEM images and show if films are under compressive (green hue here) or tensile (red) strain. To accomplish this, the symmetric (200) diffraction spot from the electron beam was automatically analyzed for each point in the STEM range. Figure 5.5c-d) show these strain maps for the same regions pictured in a-b). At the dislocation sites, the film clearly moves from a highly compressive to highly tensile strain in an acute manner. This abrupt change shows how efficient these sites are at relieving the crystal's elastic energy in that single edge dislocations move the layers above it to the desired strain. The dislocation centers are also laterally separated by an average distance of 17.4 ± 4.9 nm, which again shows that the films efficiently release energy at dislocation cores and do not need a high density of dislocations to do so.

With this knowledge of dislocation formation in a pure BTO film, we then looked at how the addition of a single layer of SIO, with its smaller strain percentage but large symmetry mismatch, might affect core nucleation. Figure 5.6 shows the $BTO^{8uc}/SIO^{1uc}/BTO^{8uc}$ HAADF and strain map images. The BTO layer is grown to be ~3.2 nm thick in order to be below the normal BTO dislocation nucleation critical thickness and determine if the addition of interfaces will prematurely induce formation. This is indeed the case, with dislocations forming near the BTO-SIO interface at a total film thickness much less than the BTO monolithic film. This reduction in critical thickness is somewhat confounded by the fact that the two edge dislocations shown are the only observed deformations in the entire 6 μm subsection of film imaged. It is possible then that these sites are not intrinsic but a byproduct of film growth and the high change in growth

parameters (temperature and oxygen pressure) needed to achieve epitaxial growth of the disparate materials.

If the interfaces between the symmetry mismatched BTO and SIO were a primary driver of dislocation formation, we wanted to explore a film with both a large number of interfaces and also determine if SIO layer thickness played any important role. If SIO thickness was allowed to increase, it is possible that it would regain some of its bulk symmetry characteristics and induce more pronounced dislocation formation. Toward this end, we grew a [BTO^{6uc}/SIO^{m}] heterostructure, varying the SIO layer thickness as m = 2, 3, 4, 5 uc. The HAADF images and

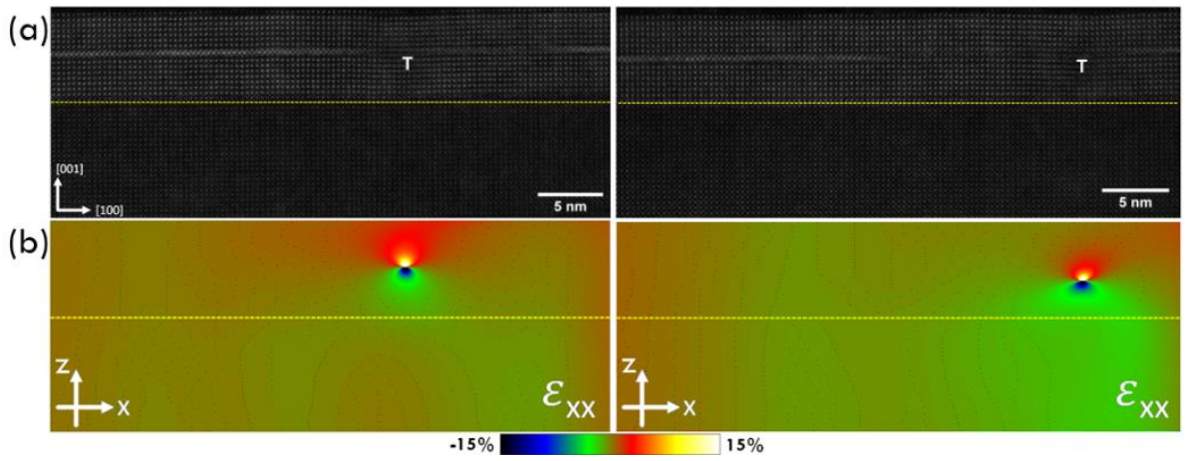

Figure 5.6. STEM image of $BTO^{8uc}/SIO^{1uc}/BTO^{8uc}$ heterostructure. a) HAADF image of large lateral area. Yellow dotted line denotes substrate interface. b) IP strain map of areas imaged in a).

corresponding IP strain maps are shown in Figure 5.7. We first analyze the quality of the interfaces created to ensure consistency between each interface formed. The colorized HAADF image in 5.7a) demonstrates the intensity profile changes seen from HAADF imaging and can be used as a

proxy for looking at interfacial intermixture by the fact that larger Z elements appear brighter in the images with a roughly $Z^{\sim 1.7}$ scaling. We can see that each of the BTO/SIO/BTO interfaces have

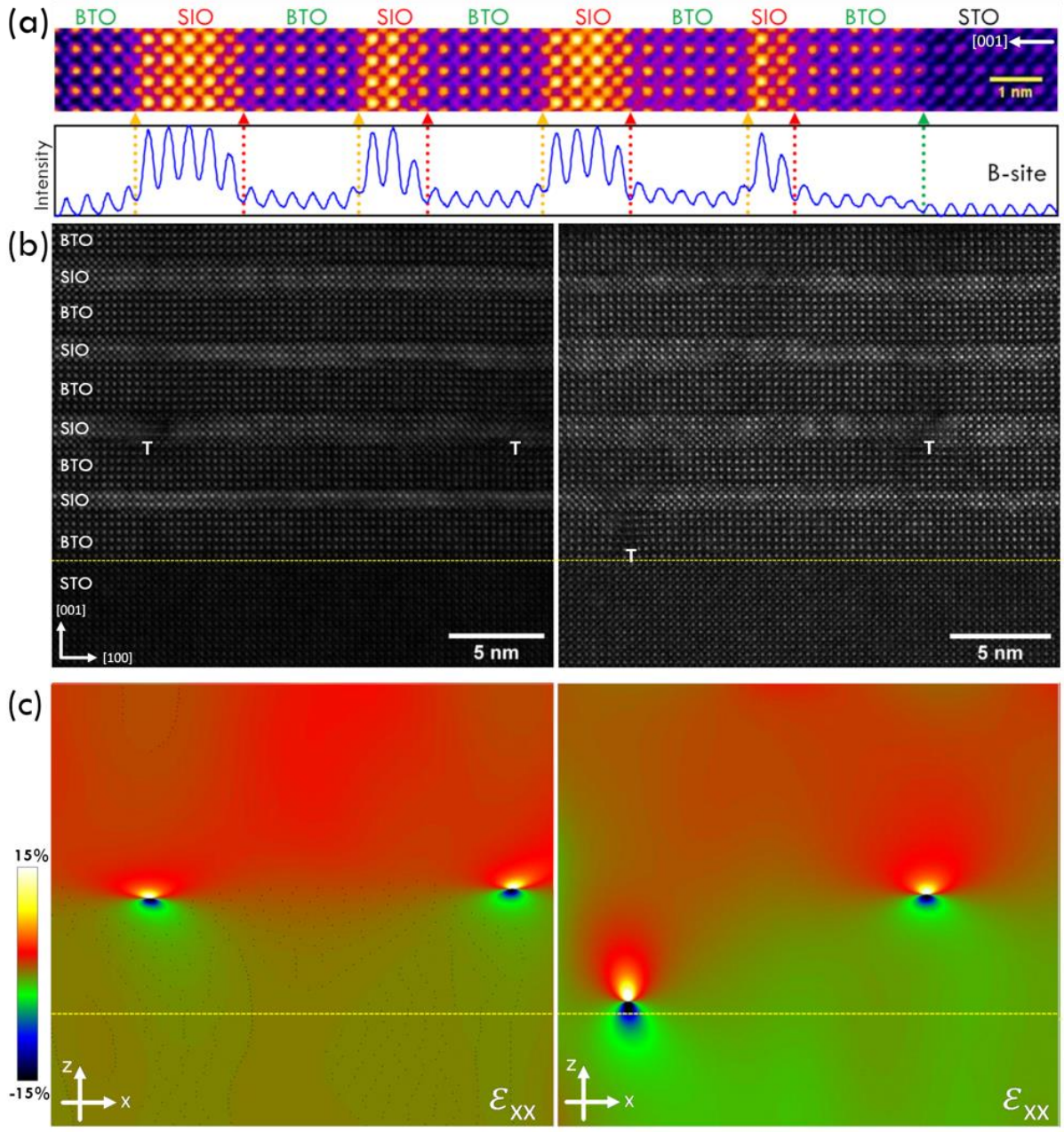

Figure 5.7. STEM images of [BTO^{6uc}/SIO^{m}] heterostructure. a) colorized HAADF image showing relative B-site intensities of the imaged spots below. Green dotted line denotes substrate interface, red dotted line denotes sharp TiO_2 – SrO interface, orange line denotes larger intermixed SrO – TiO_2 interface. b) HAADF image of large lateral area. Yellow dotted line denotes substrate interface. b) IP strain map of areas imaged in a).

a distinct intensity difference depending on which material is being used as a base layer. As an SIO layer is grown on top of BTO, the BTO surface is TiO2 terminated and will form an TiO_2 – SrO bond across the new interface. The SIO film undergoes a surface termination reversal and during growth accumulates an extra half unit cell. This occurs in many large B-site perovskites, notably SRO, and happens during the very first unit cell of a growth, characterized by a longer growth time for the first RHEED intensity oscillation than for subsequent layers [103]. At the SIO/BTO interface grown on SIO we therefore still have a SrO – TiO_2 bond, but it is evident from intensity analysis that the right-side interfaces (TiO_2 – SrO) are more sharp than the left-side interfaces (SrO – TiO_2). It is possible this increased intermixture is due to the termination reversal of SIO making the surface less stable for growth and allowing more intermixture into BTO [168]. Even the enhanced intermixture is limited to a single unit cell into the BTO films and does not seem to be a cause for any dislocation formation.

Dislocation cores are formed in this heterostructure, as seen in Figure 5.7b-c), but their location is intriguing. The first interface between BTO and SIO occurs at a film thickness of 2.5nm (bottom of SIO layer) and the second at 3.75 nm (top SIO layer). Neglecting the single misfit dislocation observed at the STO substrate interface, no dislocations are formed at these first two interfaces. This is in contrast to what was observed in the $BTO^{8uc}/SIO^{1uc}/BTO^{8uc}$ trilayer, where the additional interfaces seemed to decrease the critical thickness for edge dislocation formation. Dislocations are indeed formed in this heterostructure though, and they begin to form near the second SIO layer interface. The second SIO layer is conveniently located at ~6nm from the STO substrate, which is similar to the thickness needed in monolithic BTO films for dislocations to begin forming. The lateral density of dislocation formation is also lower than for monolithic BTO with an average distance of 19.4 nm of separation between them. This conveys that the primary

driver of dislocation formation in these films is the accumulation of lattice strain through increased film thickness. Interfaces seem to merely provide a more likely source of extrinsic crystal deformation from epitaxial instability and are not an intrinsic driver of dislocation formation. Likewise, symmetry mismatch does not seem to be a motivator in these ultrathin systems either, as the thicker m = 2 SIO layer should have driven more dislocation formation than the m = 1 SIO layer from Figure 5.6 if symmetry mismatch were a primary source of dislocations. We note that after the films are allowed to relax through edge dislocations in Figure 5.7b-c), no further dislocations are observed throughout the films, which is indicative of the efficiency of these

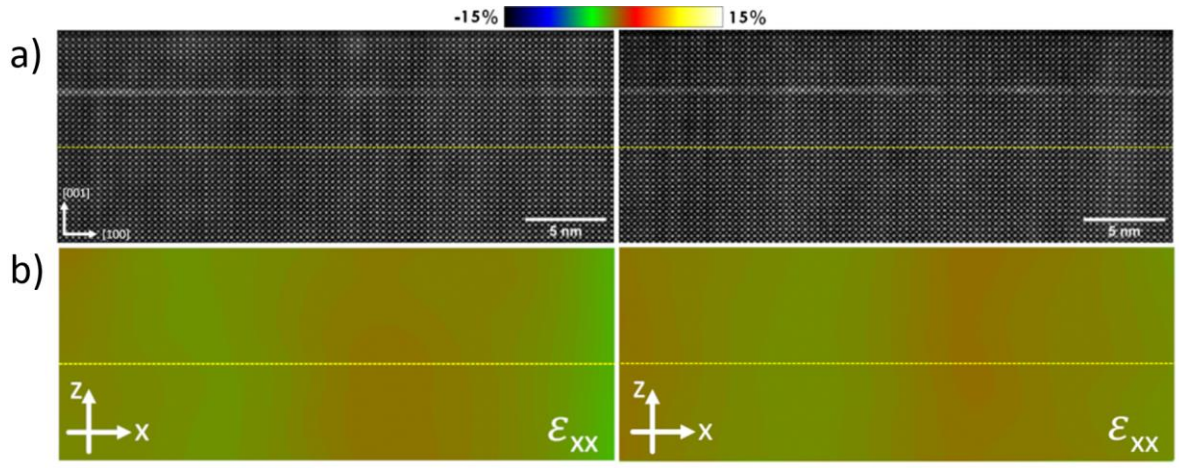

Figure 5.8. STEM image of $STO^{8uc}/SIO^{1uc}/STO^{8uc}$ heterostructure. a) HAADF image of large lateral area. Yellow dotted line denotes substrate interface. b) IP strain map of areas imaged in a).

dislocation sites in allowing the grown film to relax toward its desired lattice constants.

We also imaged $STO^{8uc}/SIO^{1uc}/STO^{8uc}$ films in order to ensure that it was not the TiO2-SrO2 interfacial layer or SIO symmetry change that was causing dislocation formation. Figure 5.8a-b) shows the HAADF and strain map images for this film. We see that no dislocation cores are found in the entire imaged area. This shows that the simple addition of an interface does not increase dislocation formation in titanate - iridate heterostructures and that accumulated elastic

strain energy is a more important factor. It should be noted that this film is almost entirely homoepitaxial, with only a single IrO_2 layer substituted for a TiO_2 layer.

Considering our SIO and BTO XRD results in tandem with these observations, we posit that BTO thickness is the primary driver of dislocation formation in these strained systems. XRD shows that we can grow thick SIO films without relaxation but thinner thicknesses of BTO relax. If the two dislocations from the sub-6nm film in Figure 5.6 are discounted as epitaxial errors (which is likely given their average lateral spacing of ~3 μm), then that film effectively has no dislocation cores. This means that, for both the $BTO^{8uc}/SIO^{1uc}/BTO^{8uc}$ and $[BTO^{6uc}/SIO^{m}]$ films, the only intrinsic factor of whether the films stay strained or lose substrate coherence through edge dislocations is the thickness of the BTO film. If the film is too thin, as in $BTO^{8uc}/SIO^{1uc}/BTO^{8uc}$, then no dislocations will be formed, but once the critical thickness is reached either in monolithic or heterostructured form, dislocation nucleation begins. The amount of compressive strain imposed by the STO (001) substrate is then the most likely driver of dislocation formation in such heteroepitxial films. It is also noted that BTO has a lower bulk modulus than SIO (135 and 187.1 GPa, respectively), and lower bulk moduli have been shown to allow for easier dislocation formation [169–171]. It is also noteworthy that these dislocations do not appear to affect the mosaicity of the films (evidenced by the similar rocking curve XRD behavior between films) as might be expected, and is explained by their relatively low lateral density and their efficiency toward pure relaxation of the films and not domain formation [172].

If these edge dislocations are driving the film relaxation as we expect, then we should be able to see their effect through analysis of the layer-by-layer IP and OOP lattice constants. This was undertaken for the $STO^{8uc}/SIO^{1uc}/STO^{8uc}$, the $BTO^{8uc}/SIO^{1uc}/BTO^{8uc}$, and the $[BTO^{6uc}/SIO^{m}]$ heterostructures to compare as the number of interfaces and film thicknesses were varied, and the

results are shown in Figure 5.9. Panels a-c) show a representative (010) cut HAADF image used for the averaging analysis, but a total lateral area of 40 unit cells were used for the averaging. Figure 5.9d-e) show the respective IP and OOP lattice constants as a function of film thickness away from the substrate interface (denoted as 0 distance). Looking at the IP lattice constants (Fig 5.9d), it is clear that the thin trilayer structures, both STO and BTO dominated films, do not bulk relax away from the STO substrate strained value, which is expected given the low number of dislocation cores. The large heterostructure does however begin to show a relaxation from the STO IP constant (denoted by the lower black dotted line) around 13 unit cells, or 5.58 nm away from the substrate, that continues throughout the film until a full relaxation to BTO's bulk IP value of 4 Å is achieved. This is the same thickness regime where dislocations begin to form and confirms that these sites are responsible for the relaxation of the thick films. We can also surmise from the

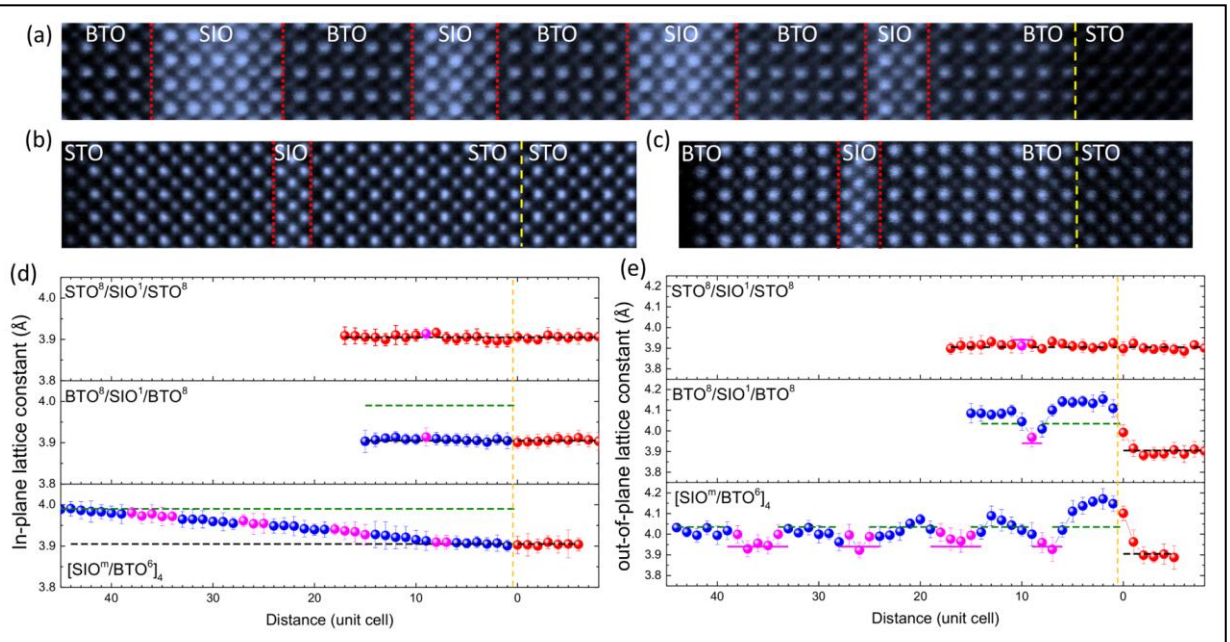

Figure 5.9. IP and OOP lattice constants of multiple films. a-c) representative HAADF imaged areas of [BTO^{6uc}/SIO^{m}] (a) , $STO^{8uc}/SIO^{1uc}/STO^{8uc}$ (b), and $BTO^{8uc}/SIO^{1uc}/BTO^{8uc}$ (c) heterostructures. d) Laterally averaged IP lattice constants for each film. Yellow line denotes STO interface, while the black dashed line denote the STO lattice constant and the green dashed line denotes the BTO bulk lattice constant. e) Laterally averaged OOP lattice constants of each film. Purple lines denote SIO bulk OOP pseudocubic lattice constant.

gradual relaxation observed that while the dislocation cores are an acute source of strain energy dispersal, the films need a certain thickness to bulk relax from the abrupt removal of an atomic site. It is interesting that every thickness of SIO layer follows the behavior of the BTO layers and eventually even become tensile strained to the BTO IP lattice constant as opposed to the STO substrates', showing once again the these films are dominated by the film with larger strain.

OOP lattice constants for the films are observed in Figure 5.9e). Again, the $STO^{8uc}/SIO^{1uc}/STO^{8uc}$ system shows strong adherence to the STO substrate OOP constant as expected for a nearly homoepitaxial film. The trilayer $BTO^{8uc}/SIO^{1uc}/BTO^{8uc}$ shows that the BTO and SIO layers are well strained IP to STO and as a result increase their OOP lattice constants above their bulk values in order to conserve their unit cell volume (compressive strain normally induces elongated OOP lattice constants). The middle single unit cell SIO layer shows a reduced OOP expansion as a result of its lower strain when adhering to an STO substrate. BTO is elongated past its bulk value (green dashed line) in both layers and does not show pattern of relaxation toward this value. This however is not the case in the multilayered system, where we see a damped oscillatory behavior as the film thickness increases and the IP lattice constant relaxes. Once the dislocations near the second SIO layer allow the film to relax, the OOP lattice constant of BTO never surpasses its bulk value again and displays complete relaxation. This abrupt change in OOP lattice constant behavior while the IP lattice shows a gradual bulk change may be related to tensile strain imposed by the dislocation cores on the films above them (red areas of strain maps).

5.3 Conclusions

Through high resolution XRD and atomic resolution 4D STEM, we were able to determine that in compressively strained heteroepitaxial films, the material with larger strain percentage is likely to drive the overall structure of the film and any dislocations that form therein. Neither

symmetry mismatch nor interfacial intermixture seemed to play a role in defect nucleation. Studies on tensile strained $LaAlO_3$/STO films with a strain of 3% show similar thickness dependence of dislocation formation [173]. Further work on the role of symmetry mismatch should be undertaken in a more systematic way, perhaps by heterostructuring with films with higher degrees of orthorhombic tilt like $CaRuO_3$, but this preliminary work suggests that this type of mismatch is not as effective at inducing dislocation formation. We can see from this work that it is possible to strategically place dislocations at interfaces between materials, and it is possible that this type of defect engineering can be crucial in developing functional electronic wells [174, 175].

Chapter 6. Conclusions and Outlook

In this dissertation work, we have explored how interfacing between different materials can affect the fundamental structural and magnetic characteristics of thin films. We primarily looked at manganite/ruthenate heterostructures between LCMO and SRO in order to elucidate the origin of the magnetic revivification in LCMO layers. Multiple causes were considered and ruled out. In other manganite/ruthenate systems, novel magnetic effects are usually ascribed to interfacial charge transfer, but we found no evidence of this in our EELS analysis of our extremely thin trilayer. Magnetic polaron formation also does not seem to be a likely cause, as the resistivity tends to follow a VRH model as opposed to polaronic motion in the extremely thin case. Small scale FM metallic regions are also unlikely from our MR characteristics. While the DM interaction may have a slight effect in moderate SOC ruthenate heterostructures as it is known to favor a canted alignment of AFM spins, we also know from the size of the FM saturation that small canting of interfacial moments is not sufficient. Structural change does play an important role in the saturation moment of films but is not directly correlated with higher onset temperatures, as STO buffered samples have high saturation fields but lower T_c than ruthenate buffered samples. Based on these results, we come to the conclusion that the primary driver of increased magnetic onset in such systems is two-fold, with both the exchange coupling between Ru and Mn at the SrO-MnO_2 interface and small magnetic domains in SRO inducing this effect. We know that the interface termination alone is not enough as STO buffered samples also have this same termination and similar interfacial exchange coupling energies [115, 176]. SRO is known to have small-scale order FM regions, and magnetism in one heterostructure layer can induce pinning effects in interfaced layers [30, 63, 177]. CRO buffered samples have a CaO-MnO_2 termination, which due to CRO's lowered metallicity and the smaller Ca ionic radius should have a smaller exchange interaction

than its isovalent SrO terminated counterpart. These would both show that in the ultrathin limit, the incipient FM moments in ruthenates are the most important in pinning the LCMO moments IP and allowing them to large scale order at higher temperatures. Exchange coupling between the layers aids in this and determines the spin alignment of the different layers. Onset enhancement occurs regardless of the metallicity of the system, a result that has been missed in other manganite-ruthenate studies and shows that manganites can have different FM orderings.

We confirm that the coupling between the ruthenate and LCMO layers is antiferromagnetic through studies of multiple thicknesses of LCMO and SRO layers. Exchange bias behavior and downturns in magnetization are observed in thick SRO samples, and MR hysteresis and positive-

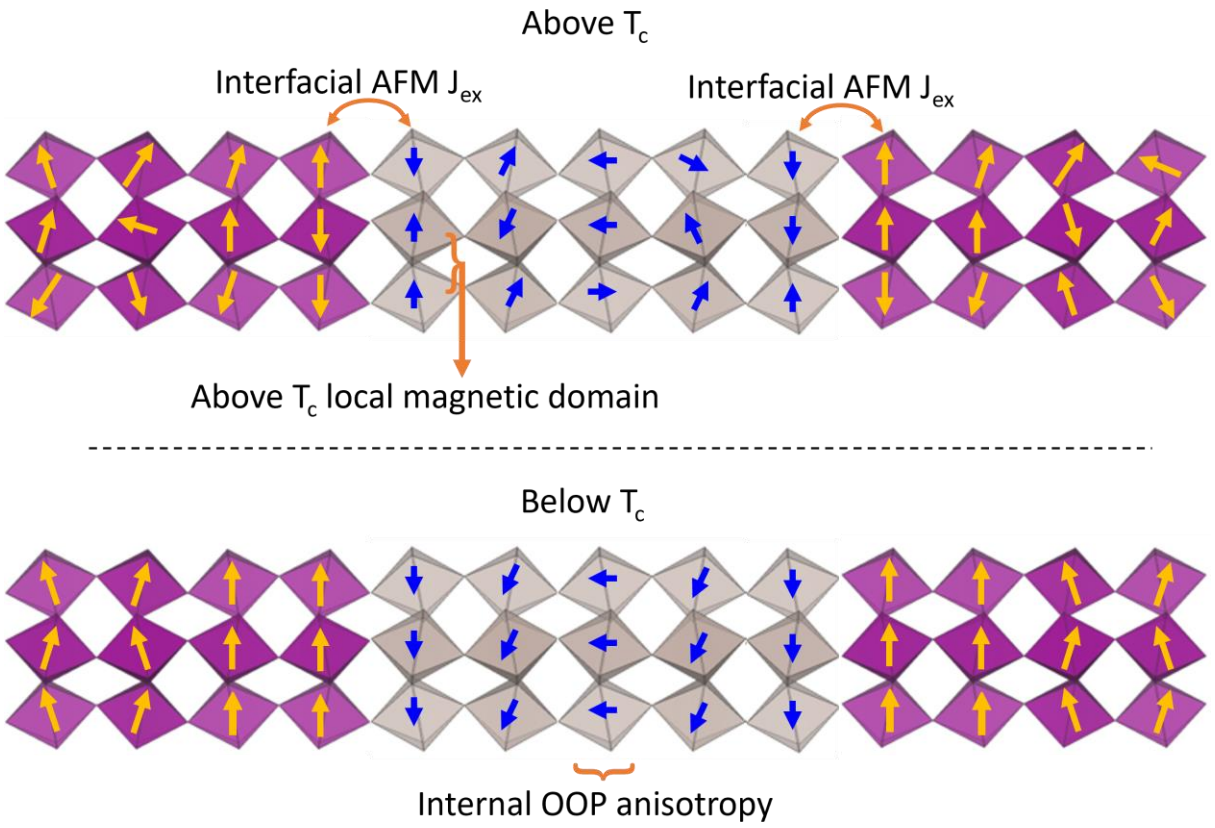

Figure 6.1. Schematic representation of B-site moments above and below Tc in LCMO/SRO/LCMO trilayer. Exchange coupling, small above Tc magnetic domains, and reemergent OOP alignment in SRO layers are shown for emphasis of key findings.

to-negative crossover is observed in both SRO and CRO buffered thick LCMO trilayers. These effects are tied to AFM interfacial alignment, and only appear in samples with sufficient thickness for the films to sufficient signal and measurable low-temperature resistivities. We also considered the magnetic anisotropy of these systems, and found that sufficiently thick SRO buffered samples regained an appreciable OOP moment away from the interface. Overall, this gives a picture of the LCMO-SRO system and magnetic character as presented schematically in Figure 6.1. The interfacial layers of LCMO and SRO are pinned IP with only slight OOP canting (~4°). Moving away from the interface, sufficiently thick SRO layers can regain their preferred OOP alignment. Above T_c, there is still pinning of the interfacial moments due to the superexchange coupling and SRO magnetic domains, though it is only below T_c that they become large scaled ordered and observable in SQUID.

In our structural work on the BTO/SIO system, we were able to exhibit a strong ability to place dislocations at interfaces by varying the thickness of compressively strained BTO layers. Dislocation formation appears in the absence of interfaces and depends solely on the thickness of the highly strained BTO layer. This can be understood as a release of elastic energy of the system with higher Young's moduli, and becomes important as film thicknesses are increased. The fact that interfaces do not drastically affect the formation allows us to formulate below critical thickness multi-heterointerface systems that would allow for much lower defect formation. Placing deformations might be useful in future studies of functional devices, as we have shown that increased localization in our LCMO systems have led to increased magnetic effects and this localization may be enhanced by strategically placed defects at the all-important interface.

Future research into the LCMO/SRO system should attempt to use optical techniques such as magneto-optical Kerr effect (MOKE) and magnetic force microscopy (MFM) to probe whether

the small-scale SRO domains extend out into the LCMO layers. This would allow us to know whether pinning by SRO moments is a definitive cause of the revived magnetism. We are also working with industrial partners who are attempting to directly image moments on an atomic scale utilizing innovative 4D-STEM techniques, and this may allow us to look at a cross-section of our samples and determine directly if the interfacial alignment is antiferromagnetic. This is exciting work that will be published in the future.

Appendix. Copyright Information

OPEN ACCESS
IOP Publishing
Journal of Physics: Condensed Matter
J. Phys.: Condens. Matter 33 (2021) 275003 (7pp)
https://doi.org/10.1088/1361-648X/abfdf1

Formation of dislocations via misfit strain across interfaces in epitaxial $BaTiO_3$ and $SrIrO_3$ heterostructures

M Saghayezhian[1], Z Wang[1,2], D Howe[1], P Siwakoti[1], E W Plummer[1], Y Zhu[2,*] and Jiandi Zhang[1,*]

[1] Department of Physics and Astronomy, Louisiana State University, Baton Rouge, LA 70803, United States of America
[2] Condensed Matter Physics and Materials Science Department, Brookhaven National Laboratory, Upton, NY 11973, United States of America

E-mail: jiandiz@lsu.edu and zhu@bnl.gov

Received 4 February 2021, revised 9 April 2021
Accepted for publication 4 May 2021
Published 28 May 2021

Abstract

Dislocations often occur in thin films with large misfit strain as a result of strain energy accumulation and can drastically change the film properties. Here the structure and dislocations in oxide heterostructures with large misfit strain are investigated on atomic scale. When grown on $SrTiO_3$ (001), the dislocations in both the monolithic $BaTiO_3$ thin film and its superlattices with $SrIrO_3$ appear above a critical thickness around 6 nm. The edge component of the dislocations is seen in both cases with the Burgers vector of $\boldsymbol{a}\langle 100\rangle$. However, compared to monolithic $BaTiO_3$, the dislocation density is slightly lower in $BaTiO_3/SrIrO_3$ superlattices. In the superlattice, when considering the $SrTiO_3$ lattice constant as the reference, $BaTiO_3$ has a larger misfit strain comparing with $SrIrO_3$. It is found that in both cases, the formation of dislocation is only affected by the critical thickness of the film with larger lattice misfit ($BaTiO_3$), regardless of the existence of a strong octahedral tilt/rotation mismatch at $BaTiO_3/SrIrO_3$ interface. Our findings suggest that it is possible to control the position of dislocations, an important step toward defect engineering.

Keywords: TEM, dislocation, multiferroics, ferroelectrics, thin films, defects

(Some figures may appear in colour only in the online journal)

1. Introduction

Dislocations are an inevitable form of defects that are ubiquitous in misfit perovskite heterostructures, as they are key in strain field relaxation and can significantly change the physical properties [1, 2]. Dislocations can work as pathways to accelerate ion transfer [3], give rise to flexoelectric polarization in $SrTiO_3$, create ferromagnetism in antiferromagnetic NiO, and paramagnetism in ferromagnetic $La_{2/3}Ca_{1/3}MnO_3$ [4–7].

In ferroelectric materials, they are responsible for depolarizing fields around the dislocation core which is detrimental to the performance of the materials [8–10]. For example, in $BaTiO_3$ thin films with large lattice mismatch, misfit dislocations (MD) form at the interface with the substrate and dislocation half-loops form away from the interface. These two forms of dislocations contribute to the strain relaxation and set a critical thickness, above which the film retains its bulk structure and loses its coherency with the substrate [9, 11], going from epitaxial to pseudomorphic or semi-coherent growth [12]. The presence of dislocation cores, at the interface or away from it, create such strong structural distortion that its strain can produce stress levels higher than the yield stress [13]. Such highly localized strain gradient can generate deep defect electronic

* Authors to whom any correspondence should be addressed.

References

1. J. Xia, W. Siemons, G. Koster, M.R. Beasley, A. Kapitulnik "Critical thickness for itinerant ferromagnetism in ultrathin films of SrRuO3" *Physical Review B* **79** 140407 (2009).

2. Y.J. Chang, C.H. Kim, S.-H. Phark, Y.S. Kim, J. Yu, T.W. Noh "Fundamental Thickness Limit of Itinerant Ferromagnetic SrRuO3 Thin Films" *Physical Review Letters* **103** 57201 (2009).

3. Y. Tokura "Critical features of colossal magnetoresistive manganites" *Reports on Progress in Physics* **69** 797–851 (2006).

4. F. Ando, M. Ishibashi, T. Koyama, Y. Shiota, T. Moriyama, D. Chiba, T. Ono "Magnetic domain writing defined by electrical gating in Pt/Co film" *Applied Physics Letters* **113**(2018).

5. M. Pan, S. Hong, J.R. Guest, Y. Liu, A. Petford-Long "Visualization of magnetic domain structure changes induced by interfacial strain in CoFe2O4/BaTiO3 heterostructures" *Journal of Physics D. Applied Physics* **46**(2013).

6. P.W. Anderson "New approach to the theory of superexchange interactions" *Physical Review* **115** 2–13 (1959).

7. J.B. Goodenough "Theory of the role of covalence in the perovskite-type manganites [La,M(II)]MnO3" *Physical Review* **100** 564–573 (1955).

8. J. Kanamori "Superexchange interaction and symmetry properties of electron orbitals" *Journal of Physics and Chemistry of Solids* **10** 87–98 (1959).

9. F. Hund "Zur Deutung verwickelter Spektren. II." *Zeitschrift für Physik* **34** 296–308 (1925).

10. J. Katriel, R. Pauncz "Theoretical Interpretation of Hund's Rule" *Advances in Quantum Chemistry* **10** 143–185 (1977).

11. M.I. Dykman, E.I. Rashba "The roots of polaron theory" *Physics Today* **68** 10–11 (2015).

12. P.S. Anil Kumar, P.A. Joy, S.K. Date "Evidence for Jahn-Teller polaron formation and spin-cluster-assisted variable-range-hopping conduction in La0.7Ca0.3MnO3" *Journal of Physics Condensed Matter* **10** 1–8 (1998).

13. A.J. Millis, P.B. Littlewood, B.I. Shraiman "Double exchange alone does not explain the resistivity of La1-xSrxMnO3" *Physical Review Letters* **74** 5144–5147 (1995).

14. I. Dzyaloshinsky "A Thermodynamic Theory of "Weak" Ferromagnetism of Antiferromagnets" *J. Phys. Chem. Solids* **4** 241–255 (1958).

15. T. Moriya "Anisotropic superexchange interaction and weak ferromagnetism" *Physical Review* **120** 91–98 (1960).

16. B. Dupé, M. Hoffmann, C. Paillard, S. Heinze "Tailoring magnetic skyrmions in ultra-thin transition metal films" *Nature Communications* **5** 1–6 (2014).

17. J. Matsuno, N. Ogawa, K. Yasuda, F. Kagawa, W. Koshibae, N. Nagaosa, Y. Tokura, M. Kawasaki "Interface-driven topological Hall effect in $SrRuO_3$-$SrIrO_3$ bilayer" *Science Advances* **2** e1600304 (2016).

18. H. Chen, H. Park, A.J. Millis, C.A. Marianetti "Charge transfer across transition-metal oxide interfaces. Emergent conductance and electronic structure" *Physical Review B - Condensed Matter and Materials Physics* **90** 1–12 (2014).

19. Z. Zhong, P. Hansmann "Band alignment and charge transfer in complex oxide interfaces" *Physical Review X* **7** 1–13 (2017).

20. A. Ohtomo, H.Y. Hwang "A high-mobility electron gas at the LaAlO3 /SrTiO3 heterointerface" *Nature* **427** 423–427 (2004).

21. S. Lin, C. Xu, L. Xu, Z.L. Wang "The Overlapped Electron-Cloud Model for Electron Transfer in Contact Electrification" *Advanced Functional Materials* **30**(2020).
22. B.A.S. Mendis, K.M.N. De Silva "A comprehensive study of linear and non-linear optical properties of novel charge transfer molecular systems" *Journal of Molecular Structure. THEOCHEM* **678** 31–38 (2004).

23. K.A. Müller, W. Berlinger, M. Capizzi, H. Gränicher "Monodomain strontium titanate" *Solid State Communications* **8** 549–553 (1970).

24. H.P.R. Frederikse, G.A. Candela "Magnetic susceptibility of insulating and semiconducting strontium titanate" *Physical Review* **147** 583–584 (1966).

25. H.S. Michio Naito "Reflection high-energy electron diffraction study on the SrTiO3 surface structure" *Physica C* **229**(1994).

26. C.W. Jones, P.D. Battle, P. Lightfoot, W.T.A. Harrison "The structure of SrRuO3 by time-of-flight neutron powder diffraction" *Acta Crystallographica Section C Crystal Structure Communications* **45** 365–367 (1989).

27. D. Kan, M. Anada, Y. Wakabayashi, H. Tajiri, Y. Shimakawa "Oxygen octahedral distortions in compressively strained SrRuO3 epitaxial thin films" *Journal of Applied Physics* **123** 235303 (2018).

28. W. Lu, W. Song, P. Yang, J. Ding, G.M. Chow, J. Chen "Strain engineering of octahedral rotations and physical properties of SrRuO 3 Films" *Scientific Reports* **5** 1–9 (2015).

29. S. Pang " Review on Electronic Correlations and the Metal-Insulator Transition in SrRuO 3 " *Applied Microscopy* **47** 187–202 (2017).

30. D.W. Jeong, H.C. Choi, C.H. Kim, S.H. Chang, C.H. Sohn, H.J. Park, T.D. Kang, D.-Y. Cho, S.H. Baek, C.B. Eom, J.H. Shim, J. Yu, K.W. Kim, S.J. Moon, T.W. Noh "Temperature Evolution of Itinerant Ferromagnetism in SrRuO 3 Probed by Optical Spectroscopy" (2013).

31. Q. Qin, L. Liu, W. Lin, X. Shu, Q. Xie, Z. Lim, C. Li, S. He, G.M. Chow, J. Chen "Emergence of Topological Hall Effect in a SrRuO 3 Single Layer" **1807008** 1–6 (2019).

32. J. Matsuno, N. Ogawa, K. Yasuda, F. Kagawa, W. Koshibae, N. Nagaosa, Y. Tokura, M. Kawasaki "Interface-driven topological Hall effect in SrRuO 3-SrIrO 3 bilayer"

33. G. Spavieri, M. Mansuripur "Origin of the spin-orbit interaction" *Physica Scripta* **90** 85501 (2015).

34. A. Manchon, A. Belabbes "Spin-Orbitronics at Transition Metal Interfaces" *Solid State Physics - Advances in Research and Applications* **68**(2017).

35. Y. Yang, S. Feng, Z. Li, T. Li, Y. Xiong, L. Cao, X. Gao "Unexpected Outstanding Room Temperature Spin Transport Verified in Organic-Inorganic Hybrid Perovskite Film" *Journal of Physical Chemistry Letters* **10** 4422–4428 (2019).

36. E. Maguid, M. Yannai, A. Faerman, I. Yulevich, V. Kleiner, E. Hasman "Disorder-induced optical transition from spin Hall to random Rashba effect" *Science* **358** 1411–1415 (2017).

37. J.G. Cheng, J.S. Zhou, J.B. Goodenough "Lattice effects on ferromagnetism in perovskite ruthenates" *Proceedings of the National Academy of Sciences of the United States of America* **110** 13312–13315 (2013).

38. D. Kan, Y. Wakabayashi, H. Tajiri, Y. Shimakawa "Interfacially engineered oxygen octahedral rotations and their impact on strain relief in coherently grown SrRu O3 films" *Physical Review B* **94** 024112 (2016).

39. S.H. Chang, Y.J. Chang, S.Y. Jang, D.W. Jeong, C.U. Jung, Y.J. Kim, J.S. Chung, T.W. Noh "Thickness-dependent structural phase transition of strained SrRuO 3 ultrathin films. The role of octahedral tilt" *Physical Review B - Condensed Matter and Materials Physics* **84** 1–5 (2011).

40. K.W. Kim, J.S. Lee, T.W. Noh, S.R. Lee, K. Char "Metal-insulator transition in a disordered and correlated SrTi 1-xRu xO 3 system. Changes in transport properties, optical spectra, and electronic structure" *Physical Review B - Condensed Matter and Materials Physics* **71** 1–11 (2005).

41. P. Mahadevan, F. Aryasetiawan, A. Janotti, T. Sasaki "Evolution of the electronic structure of a ferromagnetic metal. Case of SrRuO3" *Physical Review B - Condensed Matter and Materials Physics* **80** 3–6 (2009).

42. Q. Huang, A. Santoro, J.W. Lynn, R.W. Erwin, J.A. Borchers, J.L. Peng, K. Ghosh, R.L. Greene "Structure and magnetic order in La1−xCaxMnO3 (0<x<0.33)" *Physical Review B* **58** 2684–2691 (1998).

43. J. Klein "Epitaktische Heterostrukturen aus dotierten Manganaten" *Ph. D. Thesis* 29 (2001).

44. M. Nakamura, A. Sawa, J. Fujioka, M. Kawasaki, Y. Tokura "Interface band profiles of Mott-insulator/Nb. SrTiO3 heterojunctions as investigated by optical spectroscopy" *Physical Review B - Condensed Matter and Materials Physics* **82** 4–7 (2010).

45. H. Tanaka, N. Okawa, T. Kawai "Magnetic exchange interactions in perovskite LaMnO3/LaMO3 (M = Ni, Co, Cr, Fe) superlattices" *Solid State Communications* **110** 191–196 (1999).

46. V. Markovich, E. Rozenberg, A.I. Shames, G. Gorodetsky, I. Fita, K. Suzuki, R. Puzniak, D.A. Shulyatev, Y.M. Mukovskii "Magnetic, transport, and electron magnetic resonance properties of La0.82Ca0.18MnO3 single crystals" *Physical Review B - Condensed Matter and Materials Physics* **65** 1–8 (2002).

47. P. Anil Kumar, R. Mathieu, P. Nordblad, S. Ray, O. Karis, G. Andersson, D.D. Sarma "Reentrant superspin glass phase in a La0.82Ca0.18MnO3 ferromagnetic insulator" *Physical Review X* **4** 12–16 (2014).

48. J.C. Loudon, N.D. Mathur, P.A. Midgley "Charge-ordered ferromagnetic phase in La0.5Ca0.5MnO3" 797–800 (2002).

49. H. Sharma, A. Tulapurkar, C. V. Tomy "Sign reversal of anisotropic magnetoresistance in La0.7Ca0.3MnO3/SrTiO3 ultrathin films" *Applied Physics Letters* **105** 3–7 (2014).

50. J. Rubio-Zuazo, L. Onandia, P. Ferrer, G.R. Castro "Correlation between the electronic and atomic structure, transport properties, and oxygen vacancies on La0.7Ca0.3MnO3 thin films Cite" *Appl. Phys. Lett* **104** 21604 (2014).

51. C.J. Lu, Z.L. Wang, C. Kwon, Q.X. Jia "Microstructure of epitaxial La0.7Ca0.3MnO3 thin films grown on LaAlO3 and SrRiO3" *Journal of Applied Physics* **88** 4032–4043 (2000).
52. S. Koohfar, A.B. Georgescu, A.N. Penn, J.M. LeBeau, E. Arenholz, D.P. Kumah "Confinement of magnetism in atomically thin La0.7Sr0.3CrO3/La0.7Sr0.3MnO3 heterostructures" *npj Quantum Materials* **4** 25 (2019).

53. A.T. Zayak, X. Huang, J.B. Neaton, K.M. Rabe "Structural, electronic, and magnetic properties of SrRu O3 under epitaxial strain" *Physical Review B - Condensed Matter and Materials Physics* **74** 1–11 (2006).

54. H. Kobayashi, M. Nagata, R. Kanno, Y. Kawamoto "Structural characterization of the orthorhombic perovskites. [ARuO3 (A = Ca, Sr, La, Pr)]" *Materials Research Bulletin* **29** 1271–1280 (1994).

55. X. Zhai, L. Cheng, Y. Liu, C.M. Schlepütz, S. Dong, H. Li, X. Zhang, S. Chu, L. Zheng, J. Zhang, A. Zhao, H. Hong, A. Bhattacharya, J.N. Eckstein, C. Zeng "Correlating interfacial octahedral rotations with magnetism in (LaMnO 3+δ)N/(SrTiO3)N superlattices" *Nature Communications* **5** 1–8 (2014).

56. E.J. Moon, P. V. Balachandran, B.J. Kirby, D.J. Keavney, R.J. Sichel-Tissot, C.M. Schlepütz, E. Karapetrova, X.M. Cheng, J.M. Rondinelli, S.J. May "Effect of interfacial octahedral behavior in ultrathin manganite films" *Nano Letters* **14** 2509–2514 (2014).

57. J.M. Longo, P.M. Raccah, J.B. Goodenough "Magnetic Properties of SrRuO3 and CaRuO3" *Journal of Applied Physics* **39** 1327–1328 (1968).

58. P.K. T. Gibb, R. Greatrex, N. Greenwood "Ruthenium-99 Mossbauer Studies of the Magnetic Properties of Ternary and Quaternary Ruthenium(1v) Oxides" (1973).

59. J.L. Martínez, C. Prieto, J. Rodríguez-Carvajal, A. de Andrés, M. Vallet-Regí, J.M. González-Calbet "Structural and magnetic properties of Sr2RuO4-type oxides" *Journal of Magnetism and Magnetic Materials* **140**–**144** 179–180 (1995).

60. J.S. Lee, Y.S. Lee, T.W. Noh, K. Char, J. Park, S.J. Oh, J.H. Park, C.B. Eom, T. Takeda, R. Kanno "Optical investigation of the electronic structures of Y2Ru2O7, CaRuO3, SrRuO3, and Bi2Ru2O7" *Physical Review B - Condensed Matter and Materials Physics* **64** 2451071–2451076 (2001).

61. J.E.C. M. Shepard, G. Cao, S. McCall, F. Freibert "Magnetic and transport properties of Na doped SrRuO3 and CaRuO3" *Journal of Magnetism and Magnetic Materials* **321** 2753–2756 (2009).

62. G. Cao, S. McCall, M. Shepard, J. Crow, R. Guertin "Thermal, magnetic, and transport properties of single-crystal" *Physical Review B - Condensed Matter and Materials Physics* **56** 321–329 (1997).

63. X. Ke, M.S. Rzchowski, L.J. Belenky, C.B. Eom "Positive exchange bias in ferromagnetic La0.67Sr0.33MnO3⁄SrRuO3 bilayers" *Applied Physics Letters* **84** 5458–5460 (2004).

64. M. Ziese, I. Vrejoiu, D. Hesse "Inverted hysteresis and giant exchange bias in La0.7 Sr 0.3 MnO3/SrRuO3 superlattices" *Applied Physics Letters* **97** 3–6 (2010).

65. A. Solignac, R. Guerrero, P. Gogol, T. Maroutian, F. Ott, L. Largeau, P. Lecoeur, M. Pannetier-Lecoeur "Dual Antiferromagnetic Coupling at La0.67Sr0.33MnO3⁄ SrRuO3 Interfaces" *Physical Review Letters* **109** 27201 (2012).

66. A.F. Schäffer, L. Chotorlishvili, I. V. Maznichenko, A. Ernst, K. Dörr, I. Mertig, J. Berakdar "Element specific hysteresis of La0.7Sr0.3MnO3-SrRuO3 (LSMO-SRO) heterostructures" *APL Materials* **6** 076103 (2018).

67. M. Ziese, I. Vrejoiu, E. Pippel, P. Esquinazi, D. Hesse, C. Etz, J. Henk, A. Ernst, I. V Maznichenko, W. Hergert, I. Mertig "Tailoring Magnetic Interlayer Coupling in La0.67Sr0.33MnO3⁄SrRuO3 Superlattices" *Physical Review Letters* **104** 167203 (2010).

68. G. Gong, A. Gupta "Perovskite oxide superlattices. Magnetotransport and magnetic properties" *Physical Review B - Condensed Matter and Materials Physics* **54**(1996).

69. V. Suresh Kumar, S.-L. Zhou, R.-R. Liu, Y.-M. Zhu, H.-J. Liu, Y.-Y. Chin, H.-J. Lin, C.-T. Chen, Q. Zhan, Y.-H. Chu "Antiferromagnetic Interfacial Coupling and Giant Magnetic Hysteresis in La 0.5 Ca 0.5 MnO 3 −SrRuO 3 Superlattices" (2018).

70. V.S.K. Channam "Synthesis of strongly correlated oxides and investigation of their electrical and optical properties" *PhD Thesis* (2017).

71. N.J.C. Ingle, A. Yuskauskas, R. Wicks, M. Paul, S. Leung "The structural analysis possibilities of reflection high energy electron diffraction" *Journal of Physics D. Applied Physics* **43**(2010).

72. A. Juarez "Introduction to hemispherical deflection analysers." 2–3 (2012).

73. S. Chatterjee, C. Cushman, N.J. Smith, C. Incorporated, H. Samha "Trends in Advanced XPS Instrumentation. 2. Angle-Resolved XPS (AR- XPS) and XPS Surface Mapping" (2017).

74. S.A. Speakman "Basics of X-Ray Powder Diffraction Training" *MIT*

75. J.M. Triscone, P. Fivat, M. Andersson, M. Decroux, O. Fischer "Two-dimensional and three-dimensional vortex lattice dynamics in DyBa2Cu3O7-(Y1-xPrx)Ba2Cu3O7 coupled heterostructures" *Physical Review B* **50** 1229–1236 (1994).

76. C. Gan, B. Materials, U. Modern "Characterizing GaN Based Materials Using Modern X - Ray Methods" 1–16 (2016).

77. Z. Li, L. Jiu, Y. Gong, L. Wang, Y. Zhang, J. Bai, T. Wang "Semi-polar (11-22) AlGaN on overgrown GaN on micro-rod templates. Simultaneous management of crystal quality improvement and cracking issue" *Applied Physics Letters* **110**(2017).

78. G.A. Morton, E.G. Ramberg "Point projector electron microscope" *Physical Review* **56** 705 (1939).

79. J. Liu "Scanning transmission electron microscopy and its application to the study of nanoparticles and nanoparticle systems" *Journal of Electron Microscopy* **54** 251–278 (2005).

80. O.L. Krivanek, N. Dellby, A.R. Lupini "Towards sub-Å electron beams" *Ultramicroscopy* **78** 1–11 (1999).

81. Pennycook, Stephen J. , Peter D. Nellist "Scanning Transmission Electron Microscopy. Imaging and Analysis" (2011).

82. H.H. Rose "Optics of high-performance electron microscopes" *Science and Technology of Advanced Materials* **9**(2008).

83. S.J.P.C. Albina Y. Borisevich, Andrew R. Lupini "Depth sectioning with the aberration-corrected scanning transmission electron microscope" *Proceedings of the National Academy of Sciences of the United States of America* **103** 16081 (2004).

84. I. MacLaren, T.A. MacGregor, C.S. Allen, A.I. Kirkland "Detectors-The ongoing revolution in scanning transmission electron microscopy and why this important to material characterization" *APL Materials* **8**(2020).

85. H. Ryll, M. Simson, R. Hartmann, P. Holl, M. Huth, S. Ihle, Y. Kondo, P. Kotula, A. Liebel, K. Müller-Caspary, A. Rosenauer, R. Sagawa, J. Schmidt, H. Soltau, L. Strüder "A pnCCD-based, fast direct single electron imaging camera for TEM and STEM" *Journal of Instrumentation* **11**(2016).

86. C. Mahr, K. Müller-Caspary, T. Grieb, F.F. Krause, M. Schowalter, A. Rosenauer "Accurate measurement of strain at interfaces in 4D-STEM. A comparison of various methods" *Ultramicroscopy* **221** 113196 (2021).

87. C. Ophus "Four-Dimensional Scanning Transmission Electron Microscopy (4D-STEM). From Scanning Nanodiffraction to Ptychography and Beyond" *Microscopy and Microanalysis* 563–582 (2019).

88. S.J. Pennycook, L.A. Boatner "Chemically sensitive structure-imaging with a scanning transmission electron microscope" *Nature* **336** 565–567 (1988).

89. G. Guzzinati, W. Ghielens, C. Mahr, A. Béché, A. Rosenauer, T. Calders, J. Verbeeck "Electron Bessel beam diffraction for precise and accurate nanoscale strain mapping" *Applied Physics Letters* **114**(2019).

90. M. Vatanparast, P.E. Vullum, M. Nord, J.M. Zuo, T.W. Reenaas, R. Holmestad "Strategy for reliable strain measurement in InAs/GaAs materials from high-resolution Z-contrast STEM images" *Journal of Physics. Conference Series* **902** 2–6 (2017).

91. J. Fan, Y. Xie, Y. Zhu, F. Qian, Y. Ji, D. Hu, W. Tong, L. Zhang, L. Ling, C. Wang, C. Ma, H. Yang "Emergent phenomena of magnetic skyrmion and large DM interaction in perovskite manganite La 0.8 Sr 0.2 MnO 3" *Journal of Magnetism and Magnetic Materials* **483** 42–47 (2019).

92. J.G. Zhao, L.X. Yang, Y. Yu, F.Y. Li, R.C. Yu, Z. Fang, L.C. Chen, C.Q. Jin "High-pressure synthesis of orthorhombic SrIrO3 perovskite and its positive magnetoresistance" *Journal of Applied Physics* **103** 1–6 (2008).

93. Y. Tokura "Critical features of colossal magnetoresistive manganites" *Reports on Progress in Physics* **69** 797–851 (2006).

94. F. Hofer, F.P. Schmidt, W. Grogger, G. Kothleitner "Fundamentals of electron energy-loss spectroscopy" *IOP Conference Series. Materials Science and Engineering* **109**(2016).

95. O.L. Krivanek, J.P. Ursin, N.J. Bacon, G.J. Corbin, N. Dellby, P. Hrncirik, M.F. Murfitt, C.S. Own, Z.S. Szilagyi "High-energy-resolution monochromator for aberration-corrected scanning transmission electron microscopy/electron energy-loss spectroscopy" *Philosophical Transactions of the Royal Society A. Mathematical, Physical and Engineering Sciences* **367** 3683–3697 (2009).

96. R.D. Leapman, L.A. Grunes, P.L. Fejes "Study of the L23 edges in the 3d transition metals and their oxides by electron-energy-loss spectroscopy with comparisons to theory" *Physical Review B* **26** 614–635 (1982).

97. G.A. BOTTON, C.C. APPEL, A. HORSEWELL, W.M. STOBBS "Quantification of the EELS near-edge structures to study Mn doping in oxides" *Journal of Microscopy* **180** 211–216 (1995).

98. Z.L. Wang, J.S. Yin, Y.D. Jiang "EELS analysis of cation valence states and oxygen vacancies in magnetic oxides" *Micron* **31** 571–580 (2000).

99. "Superconductors" *LibreTexts.org* (2020).

100. Q. Design "Physical Property Measurement System. Hardware Manual" (2004).

101. N. Liu, F. Wei, L. Liu, H.S.S. Lai, H. Yu, Y. Wang, G.-B. Lee, W.J. Li "Optically-controlled digital electrodeposition of thin-film metals for fabrication of nano-devices" *Optical Materials Express* **5** 838 (2015).

102. N.M. Nemes, M. García-Hernández, Z. Szatmári, T. Fehér, F. Simon, C. Visani, V. Peña, C. Miller, J. García-Barriocanal, F. Bruno, Z. Sefrioui, C. Leon, J. Santamaría "Thickness dependent magnetic anisotropy of ultrathin LCMO epitaxial thin films" *IEEE Transactions on Magnetics* **44** 2926–2929 (2008).

103. G. Rijnders, D.H.A.A. Blank, J. Choi, C.-B.B. Eom "Enhanced surface diffusion through termination conversion during epitaxial SrRuO 3 growth" *Applied Physics Letters* **84** 505–507 (2004).

104. C. Lichtensteiger "InteractiveXRDfit. A new tool to simulate and fit X-ray diffractograms of oxide thin films and heterostructures" *Journal of Applied Crystallography* **51** 1745–1751 (2018).

105. C.L.C. J.C. Jiang, X.Q. Pan "Microstructure of epitaxial SRO thin films on (001) STO" *Physical Review B* **49** 16659–16669 (1998).

106. Y.L. Qin, H.W. Zandbergen, Z.Q. Yang, J. Aarts "Crystal structure of (La,Ca)MnO3 ultrathin films deposited on SrTiO3 substrates" *Philosophical Magazine* **85** 4465–4476 (2005).

107. Z.Q. Yang, R. Hendrikx, J. Aarts, Y.L. Qin, H.W. Zandbergen "Properties and microstructure of ultrathin (La,Ca)MnO3 films under different conditions of strain" *Physical Review B - Condensed Matter and Materials Physics* **70** 1–6 (2004).

108. Q. Xie, K. Gao, X. Wu, G. Cheng, L. Chen, T. Xie "Reduced electric dead layer in tensile strained La2/3Ca1/3MnO3 ultrathin films" *Materials Letters* **140** 174–176 (2015).

109. J.C. Jiang, W. Tian, X. Pan, Q. Gan, C.B. Eom "Effects of miscut of the SrTiO3 substrate on microstructures of the epitaxial SrRuO3 thin films" *Materials Science and Engineering B* **56** 152–157 (1998).

110. J.C. Jiang, W. Tian, X.Q. Pan, Q. Gan, C.B. Eom "Domain structure of epitaxial SrRuO3 thin films on miscut (001) SrTiO3 substrates" *Applied Physics Letters* **72** 2963–2965 (1998).

111. G. Sanchez-Santolino, M. Cabero, M. Varela, J. Garcia-Barriocanal, C. Leon, S.J. Pennycook, J. Santamaria "Oxygen octahedral distortions in LaMO3/SrTiO3 superlattices" *Microscopy and Microanalysis* **20** 825–831 (2014).

112. C. Colliex, L. Bocher, F. De La Peňa, A. Gloter, K. March, M. Walls "Atomic-scale STEM-EELS mapping across functional interfaces" *Jom* **62** 53–57 (2010).

113. S. Das, A.D. Rata, I. V. Maznichenko, S. Agrestini, E. Pippel, K. Chen, S.M. Valvidares, H.B. Vasili, J. Herrero-Martin, E. Pellegrin, K. Nenkov, A. Herklotz, A. Ernst, I. Mertig, Z. Hu, K. Doerr "Termination control of magnetic coupling at a complex oxide interface" (2016).

114. M.M. Koch, L. Bergmann, S. Agrestini, I. Maznichenko, I. Mertig, A. Herklotz, S. Das, D.A. Rata, K. Dörr "Thickness-Dependent Ru Exchange Spring at La0.7Sr0.3MnO3–SrRuO3 Interface" *Physica Status Solidi (B) Basic Research* **257**(2020).

115. S. Das, A.D. Rata, I. V. Maznichenko, S. Agrestini, E. Pippel, N. Gauquelin, J. Verbeeck, K. Chen, S.M. Valvidares, H. Babu Vasili, J. Herrero-Martin, E. Pellegrin, K. Nenkov, A. Herklotz, A. Ernst, I. Mertig, Z. Hu, K. Dörr "Low-field switching of noncollinear spin texture at L a0.7 S r0.3Mn O3-SrRu O3 interfaces" *Physical Review B* **99** 1–11 (2019).

116. D. Lan, B. Chen, L.L. Qu, F. Jin, Z. Guo, L. Xu, K. Zhang, G. Gao, F. Chen, S. Jin, L. Wang, W. Wu "Interfacial Engineering of Ferromagnetism in Epitaxial Manganite/Ruthenate Superlattices via Interlayer Chemical Doping" *ACS Applied Materials and Interfaces* **11** 10399–10408 (2019).

117. B.B. Chen, P.F. Chen, H.R. Xu, X.L. Tan, F. Jin, Z. Guo, B.W. Zhi, W.B. Wu "Contrasting size-scaling behavior of ferromagnetism in La 0.67Ca0.33MnO3 films and La 0.67Ca0.33MnO3/CaRuO3 multilayers" *Applied Physics Letters* **104** 0–5 (2014).

118. M. Ziese, I. Vrejoiu "Properties of manganite/ruthenate superlattices with ultrathin layers" *Physica Status Solidi - Rapid Research Letters* **7** 243–257 (2013).

119. R.F. Egerton, M. Malac "EELS in the TEM" *Journal of Electron Spectroscopy and Related Phenomena* **143** 43–50 (2005).

120. L.A.J. Garvie, A.J. Craven "Electron-beam-induced reduction of Mn4+ in manganese oxides as revealed by parallel EELS" *Ultramicroscopy* **54** 83–92 (1994).

121. X. Ke, M.S. Rzchowski, L.J. Belenky, C.B. Eom "Positive exchange bias in ferromagnetic La 0.67Sr 0.33MnO 3/SrRuO 3 bilayers" *Applied Physics Letters* **84** 5458–5460 (2004).

122. H. Zhang, J. Zhang, J.E. Zhang, F.R. Han, H.L. Huang, J.H. Song, B.G. Shen, J.R. Sun "Antiferromagnetic interlayer coupling of (111)-oriented La0.67Sr0.33MnO3/SrRuO3 superlattices" *Chinese Physics B* **28** 0–4 (2019).

123. P. Kaur, K.K. Sharma, R. Pandit, R.J. Choudhary, R. Kumar "Structural, electrical, and magnetic properties of SrRuO3 thin films" *Applied Physics Letters* **104**(2014).

124. C. Wang, C. Chen, C.H. Chang, H.S. Tsai, P. Pandey, C. Xu, R. Böttger, D. Chen, Y.J. Zeng, X. Gao, M. Helm, S. Zhou "Defect-Induced Exchange Bias in a Single SrRuO3 Layer" *ACS Applied Materials and Interfaces* **10** 27472–27476 (2018).

125. L.H. Bennett, E. Della Torre "Analysis of wasp-waist hysteresis loops" *Journal of Applied Physics* **97** 8–11 (2005).

126. D. Toyota, I. Ohkubo, H. Kumigashira, M. Oshima, T. Ohnishi, M. Lippmaa, M. Takizawa, A. Fujimori, K. Ono, M. Kawasaki, H. Koinuma "Thickness-dependent electronic structure of ultrathin SrRu O3 films studied by in situ photoemission spectroscopy" *Applied Physics Letters* **87** 1–3 (2005).

127. F. Bern, M. Ziese, A. Setzer, E. Pippel, D. Hesse, I. Vrejoiu "Structural, magnetic and electrical properties of SrRuO3 films and SrRuO3/SrTiO3 superlattices" *Journal of Physics Condensed Matter* **25**(2013).

128. H. Boschker, T. Harada, T. Asaba, R. Ashoori, A. V. Boris, H. Hilgenkamp, C.R. Hughes, M.E. Holtz, L. Li, D.A. Muller, H. Nair, P. Reith, X. Renshaw Wang, D.G. Schlom, A. Soukiassian, J. Mannhart "Ferromagnetism and Conductivity in Atomically Thin SrRuO3" *Physical Review X* **9**(2019).

129. A. Krichene, W. Boujelben, S. Mukherjee, N.A. Shah, P.S. Solanki "An empirical model for magnetic field dependent resistivity and magnetoresistance in manganites. Application on polycrystalline charge-ordered La0.4Gd0.1Ca0.5MnO3" *Physical Chemistry Chemical Physics* **20** 12608–12617 (2018).

130. K.V. Sarathy, S. Parashar, A.R. Raju, C.N.R. Rao "Hopping conduction in charge-ordered rare-earth manganates Ln 1 − x Ca x MnO 3 (Ln = rare earth)" *Solid State Sciences* **4** 353–357 (2002).

131. K.O. J.M. D. Coey, M. Viret, L. Ranno "Electron Localization in Mixed-Valence Manganites" *Physical Review Letters* (1995).

132. M. Viret, L. Ranno, J. Coey "Magnetic localization in mixed-valence manganites" *Physical Review B - Condensed Matter and Materials Physics* **55** 8067–8070 (1997).

133. M. Ziese, C. Srinitiwarawong "Polaronic effects on the resistivity of manganite thin films" *Physical Review B - Condensed Matter and Materials Physics* **58** 11519–11525 (1998).

134. D. Das, C.M. Srivastava, D. Bahadur, A.K. Nigam, S.K. Malik "Magnetic and electrical transport properties of La0.67Ca 0.33MnO3 (LCMO).xZnO composites" *Journal of Physics Condensed Matter* **16** 4089–4102 (2004).

135. I.B. Shim, S.Y. Bae, Y.J. Oh, S.Y. Choi "Magnetic inhomogeneity in colossal magnetoresistive La0.67Ca0.33MnO3-δ perovskite ceramics" *Solid State Ionics* **108** 241–247 (1998).

136. J.J. Neumeier, M.F. Hundley, M.G. Smith, J.D. Thompson, C. Allgeier, H. Xie, W. Yelon, J.S. Kim "Magnetic, thermal, transport, and structural properties of Sr2RuO4+. Enhanced charge-carrier mass in a nearly metallic oxide" *Physical Review B* **50** 17910–17916 (1994).

137. R. Sobhanan Helen, W. Prellier, P. Padhan "Evidence of weak antilocalization in quantum interference effects of (001) oriented La0.7Sr0.3MnO3-SrRuO3superlattices" *Journal of Applied Physics* **128** 0–7 (2020).

138. J.S. Dodge, E. Kulatov, L. Klein, C.H. Ahn, J.W. Reiner, L. Miéville, T.H. Geballe, M.R. Beasley, A. Kapitulnik, H. Ohta, Y. Uspenskii, S. Halilov "Temperature-dependent local exchange splitting in SrRuO3" *Physical Review B - Condensed Matter and Materials Physics* **60** R6987–R6990 (1999).

139. M. Ziese, E. Pippel, E. Nikulina, M. Arredondo, I. Vrejoiu "Exchange coupling and exchange bias in La0.7Sr 0.3MnO3-SrRuO3 superlattices" *Nanotechnology* **22**(2011).

140. J. Nogués, C. Leighton, I.K. Schuller "Correlation between antiferromagnetic interface coupling and positive exchange bias" *Physical Review B - Condensed Matter and Materials Physics* **61** 1315–1317 (2000).

141. and D.N. I. Panagiotopoulos, C. Christides, N. Moutis, M. Pissas "Exchange biasing in LCMO multilayers" **4913** 3–6 (1999).

142. M. Ziese, F. Bern, I. Vrejoiu "Exchange bias in manganite/SrRuO3 superlattices" *Journal of Applied Physics* **113**(2013).

143. Z.J. Guo, J.S. Jiang, J.E. Pearson, S.D. Bader, J.P. Liu "Exchange-coupled Sm-Co/Nd-Co nanomagnets. Correlation between soft phase anisotropy and exchange field" *Applied Physics Letters* **81** 2029–2031 (2002).

144. M. Ziese, F. Bern, I. Vrejoiu "Exchange bias in manganite/SrRuO3 superlattices" *J. Appl. Phys* **113** 63911 (2013).

145. M. Zheng, X. Li, W. Xiao, W. Wang, H. Ni "Oxygen deficiency and cooling field driven vertical hysteretic shift in epitaxial SrRuO3/SrTiO3 heterostructures" *Applied Physics Letters* **111**(2017).

146. M. Ziese, I. Vrejoiu, E. Pippel, A. Hähnel, E. Nikulina, D. Hesse "Orthorhombic-to-tetragonal transition of SrRuO3 layers in Pr0.7Ca0.3MnO3/SrRuO3 superlattices" *Journal of Physics D. Applied Physics* **44**(2011).

147. M. Huijben, G. Koster, Z.L. Liao, G. Rijnders "Interface-engineered oxygen octahedral coupling in manganite heterostructures" *Applied Physics Reviews* **4**(2017).

148. Y. Shiomi, Y. Handa, T. Kikkawa, E. Saitoh "Anomalous Hall effect with giant hysteresis loop in La0.67Sr0.33MnO3|SrRuO3 superlattices" *Physical Review B - Condensed Matter and Materials Physics* **92** 1–4 (2015).

149. A. Sahoo, W. Prellier, P. Padhan "Ultrathin Scale Tailoring of Anisotropic Magnetic Coupling and Anomalous Magnetoresistance in SrRuO 3 -PrMnO 3 Superlattices" *ACS Applied Materials and Interfaces* **10** 44190–44196 (2018).

150. S. Tripathi, R. Rana, S. Kumar, P. Pandey, R.S. Singh, D.S. Rana "Ferromagnetic CaRuO3" *Scientific Reports* **4** 1–7 (2014).

151. B. Paudel, B. Zhang, Y. Sharma, K.T. Kang, H. Nakotte, H. Wang, A. Chen "Anisotropic domains and antiferrodistortive-transition controlled magnetization in epitaxial manganite films on vicinal SrTiO3substrates" *Applied Physics Letters* **117**(2020).

152. D.J. Groenendijk, N. Manca, G. Mattoni, L. Kootstra, S. Gariglio, Y. Huang, E. Van Heumen, A.D. Caviglia "Epitaxial growth and thermodynamic stability of SrIrO3/SrTiO3 heterostructures" *Applied Physics Letters* **109**(2016).

153. T.A. B. J. Kim, H. Ohsumi, T. Komesu, S. Sakai, T. Morita, H. Takagi "Phase-Sensitive Observation of a Spin-Orbital Mott State in Sr2IrO4" **323** 632–632 (2009).

154. T.R. Dasa, L. Hao, J. Yang, J. Liu, H. Xu "Strain effects on structural and magnetic properties of SrIrO3/SrTiO3 superlattice" *Materials Today Physics* **4** 43–49 (2018).

155. Z. Zeng, J. Feng, X. Zheng, C. Wang, J. Liu, Z. Lu, F.X. Jiang, X.H. Xu, Z. Wang, R.W. Li "Emergent ferromagnetism with tunable perpendicular magnetic anisotropy in short-periodic SrIrO3/SrRuO3 superlattices" *Applied Physics Letters* **116**(2020).

156. J. Matsuno, K. Ihara, S. Yamamura, H. Wadati, K. Ishii, V. V. Shankar, H.Y. Kee, H. Takagi "Engineering a Spin-Orbital Magnetic Insulator by Tailoring Superlattices" *Physical Review Letters* **114** 1–5 (2015).

157. Y. Li, L. Zhang, Q. Zhang, C. Li, T. Yang, Y. Deng, L. Gu, D. Wu "Emergent Topological Hall Effect in La0.7Sr0.3MnO3/SrIrO3 Heterostructures" *ACS Applied Materials and Interfaces* **11** 21268–21274 (2019).

158. H. Guo, Z. Wang, S. Dong, S. Ghosh, M. Saghayezhian, L. Chen, Y. Weng, A. Herklotz, T.Z. Ward, R. Jin, S.T. Pantelides, Y. Zhu, J. Zhang, E.W. Plummer "Interface-induced multiferroism by design in complex oxide superlattices" *Proceedings of the National Academy of Sciences* **114** E5062 LP-E5069 (2017).

159. K. Fujimoto, Y. Kobayashi, K. Kubota "Growth of BaTiO3SrTiO3 thin films by r.f. magnetron sputtering" *Thin Solid Films* **169** 249–256 (1989).

160. A. Biswas, Y.H. Jeong "Growth and engineering of perovskite SrIrO3 thin films" *Current Applied Physics* **17** 605–614 (2017).

161. B. Carcan, H. Bouyanfif, M. El Marssi, F. Le Marrec, L. Dupont, C. Davoisne, J. Wolfman, D.C. Arnold "Phase Diagram of BiFeO3/LaFeO3 Superlattices. Antiferroelectric-Like State Stability Arising from Strain Effects and Symmetry Mismatch at Heterointerfaces" *Advanced Materials Interfaces* **4** 1–11 (2017).

162. H. Simons, A.C. Jakobsen, S.R. Ahl, H.F. Poulsen, W. Pantleon, Y.H. Chu, C. Detlefs, N. Valanoor "Nondestructive Mapping of Long-Range Dislocation Strain Fields in an Epitaxial Complex Metal Oxide" *Nano Letters* **19** 1445–1450 (2019).

163. G. Wagner "The Film Surface as the Site for Spontaneous Nucleation of Dislocation Half-Loops in Strained Heteroepitaxial Systems" *Physica Status Solidi (a)* **173** 385–403 (1999).

164. K. Shintani, H. Yonezawa "Comparative study of critical thicknesses of strained epitaxial layers based on the zero-energy criterion of dislocation half-loops" *Journal of Applied Physics* **78** 5022–5027 (1995).

165. H.P. Sun, X.Q. Pan, J.H. Haeni, D.G. Schlom "Structural evolution of dislocation half-loops in epitaxial BaTiO 3 thin films during high-temperature annealing" *Applied Physics Letters* **85** 1967–1969 (2004).

166. J.L. MacManus-Driscoll, M.P. Wells, C. Yun, J.W. Lee, C.B. Eom, D.G. Schlom "New approaches for achieving more perfect transition metal oxide thin films" *APL Materials* **8**(2020).

167. H.P. Sun, W. Tian, X.Q. Pan, J.H. Haeni, D.G. Schlom "Evolution of dislocation arrays in epitaxial BaTiO 3 thin films grown on (100) SrTiO 3" *Applied Physics Letters* **84** 3298–3300 (2004).

168. M. Gibert, M. Viret, A. Torres-Pardo, C. Piamonteze, P. Zubko, N. Jaouen, J.M. Tonnerre, A. Mougin, J. Fowlie, S. Catalano, A. Gloter, O. Stéphan, J.M. Triscone "Interfacial Control of Magnetic Properties at LaMnO3/LaNiO3 Interfaces" *Nano Letters* **15** 7355–7361 (2015).

169. C.H. Kronbo, M.B. Nielsen, S.M. Kevy, P. Parisiades, M. Bremholm "High pressure structure studies of 6H-SrIrO3 and the octahedral tilting in 3C-SrIrO3 towards a post-perovskite" *Journal of Solid State Chemistry* **238** 74–82 (2016).

170. G.J. Fischer, Z. Wang, S. ichiro Karato "Elasticity of CaTiO3, SrTiO3 and BaTiO3 perovskites up to 3.0 Gpa. the effect of crystallographic structure" *Physics and Chemistry of Minerals* **20** 97–103 (1993).

171. F. Léonard, R.C. Desai "Spinodal decomposition and dislocation lines in thin films and bulk materials" *Physical Review B - Condensed Matter and Materials Physics* **58** 8277–8288 (1998).

172. T. Suzuki, Y. Nishi, M. Fujimoto "Analysis of misfit relaxation in heteroepitaxial BaTiO3thin films" *Philosophical Magazine A. Physics of Condensed Matter, Structure, Defects and Mechanical Properties* **79** 2461–2483 (1999).

173. C. Merckling, M. El-Kazzi, G. Delhaye, V. Favre-Nicolin, Y. Robach, M. Gendry, G. Grenet, G. Saint-Girons, G. Hollinger "Strain relaxation and critical thickness for epitaxial LaAlO3 thin films grown on SrTiO3(0 0 1) substrates by molecular beam epitaxy" *Journal of Crystal Growth* **306** 47–51 (2007).

174. D. Cherns, S.J. Henley, F.A. Ponce "Edge and screw dislocations as nonradiative centers in InGaN/GaN quantum well luminescence" *Applied Physics Letters* **78** 2691–2693 (2001).

175. L. Lymperakis, J. Neugebauer, M. Albrecht, T. Remmele, H.P. Strunk "Strain induced deep electronic states around threading dislocations in GaN" *Physical Review Letters* **93** 1–4 (2004).

176. L.Y. Chen, C. Le Chen, K.X. Jin, S.F. Wang, X.J. Du "Magnetic ordering and structural stability of La2/3Sr1/3MnO3/SrTiO3 (001) interfaces. A density-functional theory study" *Physica Status Solidi (B) Basic Research* **250** 402–410 (2013).

177. E. Goto, N. Hayashi, T. Miyashita, K. Nakagawa "Magnetization and switching characteristics of composite thin magnetic films" *Journal of Applied Physics* **36** 2951–2958 (1965).

Vita

David Howe was born on in 1991 in Pittsfield, Massachusetts to loving parents Ann and Randall Howe. He was raised both in Pittsfield and Atlanta, GA and attended the Westminster Schools for his high school education. He completed his Bachelors of Science at the University of Notre Dame du Lac in 2014 with a degree in Applied Physics with Honors. He enrolled at Louisiana State University in the Physics PhD program in 2014, for which this dissertation is submitted for the completion of. He has started work as a Research Scientist at Veeco Instruments Inc.